To the Graduate Council:

I am submitting herewith a dissertation written by Zhi Shi entitled "A Study of Jets in Crossflow and Its Application on Wingtip Blowing." I have examined the final copy of this dissertation for form and content and recommend that it be accepted in partial fulfillment of the requirements for the degree of Doctor of Philosophy with a major in Aerospace Engineering.

Jain-Ming Wu, Major Professor

We have read this dissertation
and recommend its acceptance:

John E. Cawthers

Ahmad D. Vakili

Roy J. Schulz

Accepted for the Council:

Vice Provost
and Dean of the Graduate School

A STUDY OF JETS IN CROSSFLOW AND ITS APPLICATION ON WINGTIP BLOWING

A Dissertation

Presented for the

Doctor of Philosophy

Degree

The University of Tennessee, Knoxville

Zhi Shi

May 1990

ACKNOWLEDGMENTS

The author wishes to express his appreciations to many persons who have helped in various ways while in conducting and completing this dissertation.

Special thanks go to author's major professor and committee chairman Dr. J. M. Wu; his advice and encouragement throughout the course of this study have been most valuable and helpful. Many valuable suggestions in conducting experiments received from Dr. A. D. Vakili are acknowledged with deep gratitude. The author would like to thank Dr. T. H. Moulden for the stimulating discussions and diligent perusal of the manuscript. Appreciations are also go to Dr. J. E. Caruthers and Dr. R. J. Schulz for their constructive comments and deep physical insights. Sincere thanks are expressed to Prof. J. Z. Wu for many helpful discussions on the issue of vorticity dynamics.

Thanks are also extended to Mr. R. G. Ray, Mr. R. Meeker, and Mr. H. Sartain of the UTSI Gas Dynamics Laboratory for their helpful hands during the tests; to Mrs. Mary Lo for her great help in references search; and to Mr. B. Stubblefield who did most of the photographic works for this dissertation.

The author is very much appreciative in receiving the prestigious B. H. Goethert Scholarship from the Institute during this study, which made him be able to complete his doctorate degree. Special thanks are expressed to Dr. R. L. Young and his family who donated this scholarship.

Most of all, the author would like to thank his mother, wife, and daughter, for their support, encouragement and great sacrifices during the course of pursuing his advanced degrees.

ABSTRACT

The objective herein is to study the flowfield associated with jets in crossflow and their applications to the flowfield near the tip of a wing. The study was both numerical and experimental.

The flowfields of different shaped jets orientated in crossflow were studied numerically. The predicted flow features generally agreed well with measurements and observations. Qualitatively, most of the basic flow physics were captured numerically, particularly for circular jet cases where data is available for comparisons. Periodic vortex formations were captured both at the front and the rear bound shear layers of the jet plume. The well known counter-rotating vortex pair is symmetric for a symmetrically oriented jet but is asymmetric for asymmetric jet. The source of these vortices is the jet-pipe boundary-layer vorticity. For any shaped jet, a pair of vertical twin tornado-like wake vortices would always form behind the jet plume due to the lower pressure at that region. These wake vortices are asymmetric in position and different on size for an asymmetrically placed jet, The source of these vortices is the crossflow boundary-layer vorticity.

An experimental investigation of discrete wingtip jets was also conducted in both water and wind tunnels as an important application. Careful flow visualization revealed that the local perturbation introduced by the wingtip jet closely resembles that of asymmetric jets blowing from a flat plate. All types of vortices observed in the latter flowfield were identified in the flowfield generated by the wingtip jet. It was reconfirmed that the wingtip jets effectively dispersed the tip vortex and the individual jet location and blowing momentum are the major parameters. Wing surface pressure measurements indicated that wingtip jets affected the global surface pressure distribution over the wing and improved its lift.

TABLE OF CONTENTS

CHAPTER PAGE

I. INTRODUCTION 1

§ 1.1 Technical Background 1

§ 1.2 Objectives of the Present Study 5

§ 1.3 Vorticity Source in the Flowfield of Jets in Crossflow 6

II. NUMERICAL SOLUTION 11

§ 2.1 Governing Differential Equations 11

§ 2.2 Numerical Approximation 12

A. Computational Grids 12

B. Finite Difference Approximation 15

§ 2.3 Solution Procedure 16

§ 2.4 Computational Setting and Boundary Conditions 20

§ 2.5 Numerical Results and Discussion 23

A. Circular Jets 23

A.1 Circular Jet with Velocity Ratio $R = 2$ 24

A.2 Circular Jet with Velocity Ratio $R = 4$ 38

B. Large Aspect Ratio Rectangular Jet with 90° Yaw Angle . . 45

C. Slot Jet with 45° Yaw Angle 48

D. Slot Jet with 30° Yaw Angle 56

III. WATER TUNNEL EXPERIMENTS 66

§ 3.1 Water Tunnel Facility 67

§ 3.2 Flow Visualization Technique and Analysis 69

§ 3.3 Model Design and Experimental Set-up 69

§ 3.4 Water Tunnel Test Results and Discussion 76

A. Wingtip Flowfield due to Single Jet Blowing 76
B. Effects of Wingtip Blowing on the Tip-Vortex Flow 85
C. Wingtip-Jet Blowing on Swept Wings 89
IV. WIND TUNNEL EXPERIMENTS AND RESULTS 95
§ 4.1 Wind Tunnel, Model, and Experimental Set-up 95
A. UTSI Low-Speed Wind Tunnel 95
B. Model and Experimental Set-up 95
§ 4.2 Surface Streak Patterns 99
§ 4.3 Surface Pressure Measurements and Lift Coefficients 107
V. SUMMARY OF THE PRESENT STUDY 116
VI. CONCLUSIONS AND RECOMMENDATIONS 119
BIBLIOGRAPHY 121
VITA 128

LIST OF TABLES

TABLE PAGE

3.1. Swept Model Descriptions 70

3.2. Jet Configurations of Tip I 75

LIST OF FIGURES

FIGURE PAGE

1.1. Schematic control volume. 8

1.2. Vorticity orientation next to the solid surfaces. 10

2.1. Computational mesh layout. 13

2.2. Two-dimensional mesh slice in normal to z–direction (the boundary cells are shown with dashed lines). 13

2.3. A typical mesh cell with the locations of the flow variables. 14

2.4. A typical convergence process ($R = 4$ circular jet, $t = 3.35$). 18

2.5. Computational flow chart. 19

2.6. The layout of the computational setting. 20

2.7. Sketch of non-circular, asymmetrically placed jet orientation. 21

2.8. Grid structure used to approximate the circular jet orifice. 23

2.9. The sectional velocity vectors for a circular jet ($R = 2$, t=1.0). 25

2.10. The schematic flow field of jet in a crossflow for $R = 1.5$ (Foss, 1980). . 27

2.11. Schematic of the velocity profiles near the jet-orifice. 29

2.12. The reorientation of the crossflow boundary-layer vorticity. 30

2.13. Wake vortices formation for circular jet. 32

2.14. Laser induced fluorescence sectional view of a circular jet (Yu, 1987, $R = 3$, $X/D = 3$). 33

2.15. The velocity profiles at the circular jet exit ($R = 2$, t=3.0). 34

2.16. A comparison of computed and experimental jet centerlines. 36

2.17. The u–velocity profile in the $y = 0$ plane for a circular jet with $R = 2$. 37

2.18. The counter-rotating vortex pairs for circular jet with $R = 4$. 39

2.19. The front-bound vortices observed during wind tunnel test (Fric & Roshko, 1989, circular jet, $R = 2$, $Re_d = 3800$). 41

2.20. Computed jet's front-bound vortices (circular jet, $R = 4$). 42

2.21. Horizontal sectional view for $\beta = 90^o$ slot-jet ($R = 3$). 46

2.22. Vertical sectional view at the $y = 0$ plane for $\beta = 90^o$ slot-jet. 47

2.23. The development of the counter-rotating vortex pair for $\beta = 90^o$ long-slot jet (cross-sectional views, $R = 3$, t=2.5). 49

2.24. Sectional velocity vector plots for $R = 10$ long-slot jet ($\beta = 90^o$, t=2.0). 50

2.25. Grid structure used to approximate the $\beta = 45^o$ asymmetric jet orifice. 51

2.26. The sectional velocity vector plots for 45^o asymmetric jet ($R = 2$, t=3.0). 53

2.27. The development of the counter-rotating vortex pair along jet exit at various x–stations ($\beta = 45^o$, $R = 2$, t=3.0, x–locations refer to Figure 2.25). 55

2.28. The sectional velocity vectors for 45^o asymmetric jet ($R = 4$, t=2.1). 57

2.29. Grid structure used to approximate the $\beta = 30^o$ asymmetric jet orifice. 58

2.30. Sectional velocity vectors for 30^o asymmetric jet in a crossflow. . . . 59

2.31. Cross-sectional views on 45^o inclined plane at discrete x–stations. . . 62

2.32. Schematic of the flowfield of a non-symmetric jet in crossflow (Wu, Vakili, & Yu, 1986). 65

2.33. A 45^o cross-sectional view of a slot-jet at $\beta = 0^o$ (Yu, 1987, $R = 3$, $Re_d = 470$). 65

3.1. General layout of the UTSI water tunnel facility (Collins, 1982). . . . 68

3.2. Basic models used in water tunnel experiments. 71

3.3. Wingtip configurations used in water tunnel experiments. 73

3.4. Flow pattern for the wingtip with a single blowing jet. 77

3.5. Global view of the flowfield for single wingtip jet blowing (Tip I, jet #2, $U_\infty = 8$ cm/s, $\alpha = 16^o$, $C_\mu = 0.02$). 80

3.6. Near surface flow pattern for single jet blowing (Tip I, jet #1, $U_\infty = 8$ cm/s, $\alpha = 16^o$, $C_\mu = 0.02$). 81

3.7. Near surface flow pattern for a non-symmetric jet in crossflow (Wu, Vakili, & Yu, 1986, $R = 9$, $\beta = 31^o$, $Re_d = 240$). 82

3.8. Near surface flow pattern for two jets blowing (Tip I, $U_\infty = 8$ cm/s, $\alpha = 16^o$, $C_{\mu I} = C_{\mu II} = 0.02$). 83

3.9. Flow pattern for three jets blowing (Tip I, $U_\infty = 8$ cm/s, $\alpha = 10^o$, $C_{\mu I} = C_{\mu II} = C_{\mu III} = 0.02$). 84

3.10. The effect of wingtip-jet blowing on the tip vortex dispersion ($U_\infty = 9$ cm/s, $\alpha = 8^o$). 86

3.11. Tip-vortex dispersion by upper and lower circular jets blowing ($U_\infty = 9$ cm/s, $\alpha = 8^o$, Tip III). 88

3.12. Wingtip vortex for backward-swept wing without blowing ($U_\infty = 9$ cm/s, $\alpha = 8^o$). 90

3.13. Flowfield on the tip area of a backward-swept wing with tip-jet blowing ($U_\infty = 9$ cm/s, $\alpha = 8^o$, Tip III). 91

3.14. Wingtip vortex for forward-swept wing without blowing ($U_\infty = 9$ cm/s, $\alpha = 8^o$). 92

3.15. Flowfield on the tip area of a forward-swept wing with tip-jet blowing ($U_\infty = 9$ cm/s, $\alpha = 8^o$). 94

4.1. Schematic of the wing model for wind tunnel testing. 97

4.2. Experimental set-up in the wind tunnel. 98

4.3. Surface streak pattern for the wing without tip-jet blowing ($U_\infty = 45$ m/s, $\alpha = 10^o$). 100

4.4. Schematic surface streak pattern for the wing without tip-jet blowing. 102

4.5. Surface streak pattern for the wing with tip-jet blowing ($U_\infty = 45$ m/s, $\alpha = 10^o$, tip-jet $^{\#}2$, $C_\mu = 0.002$). 104

4.6. A sketch of the surface streak pattern near the jet orifice. 106

4.7. Chordwise C_p distribution at different sections (jet $^{\#}1$, $U_\infty = 20$ m/s, $\alpha = 5^o$). 108

4.8. Chordwise C_p distribution at different sections (jet $^{\#}2$, $U_\infty = 20$ m/s, $\alpha = 8^o$). 110

4.9. Spanwise C_l distribution (jet $^{\#}1$, $U_\infty = 20$ m/s, $\alpha = 5^o$). 113

4.10. Spanwise C_l distribution (jet $^{\#}2$, $U_\infty = 20$ m/s, $\alpha = 8^o$). 113

4.11. Lift coefficients C_l vs. C_μ for different angle of attack. 114

LIST OF SYMBOLS

AR	aspect ratio
B	wing span
b	width of rectangular or slot jet
C	wing chord
C_μ	jet momentum coefficient, $C_\mu = \dot{m}V_j / 0.5\rho\, U_\infty^2 \mathrm{S}$
C_l	lift coefficient
C_p	pressure coefficient
D	diameter of circular jet
f	frequency
$\vec{f}$	body force
l	length of rectangular or slot jet
$\vec{n}$	unit normal vector outward from control volume
p	static pressure
$\dot{m}$	jet mass flow rate
R	jet-to-crossflow velocity ratio, $R = V_j/U_\infty$
Re_c	Reynolds number based on C, $Re_c = U_\infty C/\nu$
Re_d	Reynolds number based on jet diameter, $Re_d = U_\infty D/\nu$
S	wing area
S	entropy
S_t	Strouhal number, $S_t = fD/U_\infty$
T	temperature
t	time
u, v, w	velocity components in physical coordinates
$\vec{V}$	velocity vector

V_j	jet exit velocity
U_∞	free stream velocity
x, y, z	physical coordinates
Λ	sweep angle of wing leading edge
α	angle of attack
$\tilde{\alpha}$	relative factor
β	jet exit model orientation angle
μ	dynamic viscosity
μ_v	Bulk viscosity
ν	kinematic viscosity coefficient, $\nu = \mu/\rho$
(ξ, η, ζ)	computational coordinates
ρ	density
$\vec{\sigma}$	dynamic vorticity flux, $\vec{\sigma} = \vec{n} \cdot \nabla(\mu\vec{\omega})$
ω	over-relaxation parameter
$\vec{\omega}$	vorticity vector
ϵ	convergence criterion
ϵ_{ijk}	Levi-Civita symbol
∇	gradient operator
τ_o	wall shear stress

Superscript

n	index for time step

Subscript

i, j, k	index for grid cells
o	index for wall boundary

CHAPTER I

INTRODUCTION

The purpose of this study was to explore certain detailed features of jets in crossflow and their application to wingtip-jet-blowing. Both numerical and experimental simulations have been adopted in the study. Wingtip-jet-blowing is considered important for two major reasons:

(a). Dispersion of the tip vortex.

(b). Reduction of induced drag.

Before such applications can be made with confidence, it is necessary to have a detailed physical understanding of such flows. The present study is devoted to this purpose. It is for this reason that both numerical and experimental studies have been undertaken.

§ 1.1 Technical Background

The problem of a jet in crossflow has received much attention in the past and has been studied extensively; both by experiments and by analyses. This is because of its wide application in engineering fields as well as in daily life.

Attracted by its applications to jet mixing for heating, cooling, or burning problems, the early investigations were mainly focused on the deflection of the jet plume, the penetration of the jet into the free-stream, and the jet cross-section behavior. During the late 1940's, Callaghan et al. (1948, 1950) investigated the penetration of jets with various shaped orifices by measuring the total pressure and temperature distributions. By using a pitot-probe, Jordinson (1958) made

velocity measurement to determine the trajectory of jets with different velocity ratios. All experimental results indicated that, due to the action of the free-stream, the jets were deflected and gradually aligned to the mean-flow. The well known development of a circular jet into a kidney shaped cross-section plume was also reported during this early phase of the studies (by Jordinson (1958), Keffer & Baines (1963), and Abramovich (1963), for example).

During the late 1960's and early 1970's, the progress in V/STOL technology brought a new interest and thrust into the research of jets in crossflow. Because of this special focus, the wall pressure distribution and the surface force became the main concern at that time. Many investigators, such as Bradbury et al. (1965), McMahon et al. (1970), Fearn and Weston (1974), and others made significant contributions to this topic. By their efforts, the wall pressure distribution for a circular transverse jet became well known and the low pressure region on the wall behind the jet was found and studied.

Another essential phenomenon of transverse jets, the periodic vortices motion in the jets' wake, has been reported by many investigators using the misleading terminology "shedding vortices". McAllister (1968) expressed the "shedding frequency" of these vortices in terms of a Strouhal number based upon the jet diameter. He reported that the Strouhal number varied form $S_t = 0.103$ for R = 3.83 to $S_t = 0.019$ for R = 34. Reilly (1968) identified two eddy groups in this flow; a periodic formation of large-scale eddies in the jet plume and another group of eddies shed from the sides of the jet. By using hot-wire measurements, McMahon et al.(1971) provided the quantitative evidence for "vortex shedding" behind a turbulent jet in crossflow for both circular and rectangular shaped orifices. As will be discussed later, this "shedding" process is different from that associated with solid surfaces.

With the development of measuring instrumentations and techniques, the detailed features of jets in crossflow, such as the velocity field, turbulence intensity, and the flow behavior inside of the jet-pipe, have been studied carefully since the early 1980's. Andreopoulos et al. (1982, 1984, 1985) measured the mean velocity field and the Reynolds stress for a circular jet issuing normally into a free-stream at jet-to-crossflow velocity ratios of 0.5, 1, and 2. One of their interesting results was that the velocity profile inside the jet-pipe, which was symmetric with respect to the pipe axis without crossflow, was distorted by the imposition of a crossflow at the exit; the mean w–velocity profile was skewed (the mean w was smaller on the wind-side of the pipe and larger on the lee-side) and the mean u–velocity became non-zero. These changes were evident closer to jet's exit and less pronounced away from it as would be expected. The degree of the distortion depended largely upon the jet-to-crossflow velocity ratio R. Crabb et al. (1981) did similar research for different jet-to-crossflow velocity ratios and reached similar conclusions.

It is only since the 1970's that some numerical solutions for jets in crossflow have been reported. Thompson (1971) presented a solution of the time-dependent, incompressible Navier-Stokes equations based on an integro-differential formulation of these equations. Chien et al. (1975) used a vorticity-velocity method to obtain numerical solution for the steady Navier-Stokes equations. The calculation of a turbulent jet by Patankar et al. (1977) exhibited good agreement for the jet centerline, the rate of jet velocity decay, and the U-velocity profile on the centre-plane. The numerical results during these early days, however, were of relatively low-resolution because of computer limitations.

Recently, several higher-resolution computations have been reported. Employing a quasi-equilibrium version of the Reynolds-stress closure model and with a symmetry assumption, Sykes et al. (1986) gave a detailed picture of the jet-plume

and a discussion of the vorticity dynamics for a turbulent jet with jet-to-crossflow ratios of 2, 4, and 8. Focusing on evaluating the fluid mechanics of a jet in crossflow, Roth (1987, 1988) calculated the solution for a steady, laminar case by using the F3D code which was developed to solve the Reynolds averaged, thin-layer Navier-Stokes equations. The basic steady flow physics for a circular jet, such as the jet centerline, the counter-rotating vortex pair, and the wake region near the wall were captured qualitatively.

Up to this date, most investigations were performed on circular jets, there are only a few studies of non-circular jets in crossflow that have been reported. McMahon et al. (1970, 1971) studied the static pressure distribution on the wall and the vortex shedding from a turbulent jet in crossflow for both circular and round-end rectangular orifices. Wu and Mosher (1969) reported their experimental and analytical investigations of symmetric round-end rectangular jets issuing into a deflecting stream. As a branch of the jet in crossflow problem, Krothapalli et al. (1989) investigated a high aspect ratio rectangular jet issuing normally into a crossflow in a subsonic wind tunnel, with the longer edge of the jet facing the oncoming flow.

Investigations on various non-symmetric jets in crossflow were carried out by Wu, Vakili, and Yu (1986, 1988). The structure and behavior of the flow field of various non-symmetric jets with various jet-orifice orientations and jet-to-crossflow velocity ratios were qualitatively studied in the water tunnel and some velocity measurements were done by using a hot-film probe. See also the work of Yu (1987).

§ 1.2 Objectives of the Present Study

Given the above background, it is clear that in spite of the extensive studies that have been made so far on circular jets in crossflow, our knowledge of the non-circular jet, especially a non-symmetriclly oriented jet, in a crossflow is still very limited. The motivation for a study of non-circular, asymmetrically oriented jets in crossflow stemmed from Wu and his coworkers' previous investigations using discrete jets blowing from the wing tip to improve the wing aerodynamic performance [12, 64-67]. Although a single jet non-symmetrically placed in a uniform crossflow was studied experimentally [68, 71] as a preliminary model to study the basic phenomena of the flowfield generated by a lateral tip-jet on a wingtip, many essential features of this kind of flow still remain to be explored and that leads to the present study. It was also believed that a basic study on a non-circular, asymmetrically oriented jet in a crossflow would have many other applications in the future.

The present investigation was mainly carried out to study the non-circular, and asymmetrically oriented jet in a crossflow and its application on aircraft wingtips. It focuses on the physics and structure of this type of flowfield; such as the shape of its plume, its velocity field structure and the associated vortices. Finally, the inter-relation between these basic features is investigated. Special attention was paid to the near field flow which is defined as the first few jet diameters from the jet exit and is the most active region of the jet/crossflow interaction process; it is in this region that the two distinct vorticity vector fields merge: that on the wall of the crossflow and that from the jet-pipe.

Two main parts of the investigation are included in this work. In part 1, a three-dimensional numerical solution of the unsteady, incompressible Navier-

Stokes equation will be developed for the case of a jet emitted normal to an uniform free-stream. Comparisons with available laboratory data and with different numerical methods were used to demonstrate the quality of the simulation. Basic features of this computed flow are presented and some explanations are given for the computed results.

As an application of this type of non-symmetric jet in a crossflow, experimental investigations were also carried out to study associated phenomena of the flowfield around wingtips with discretely positioned tip blowing jets. It is understood of course, that the jet issuing from a flat surface is considerably simpler than that associated with a wingtip configuration. The structure and behavior of the flowfield created by wingtip-jet blowing were studied through both water-tunnel and low-speed wind-tunnel experiments. Water-tunnel flow visualization and surface oil-flow technique on the wind-tunnel model were used to identify the different types of vortices and study the effect of wingtip blowing on the tip vortex. A wing-surface pressure distribution measurement was undertaken in order to study the effects of the wingtip-jet blowing on wing lift. All these results are presented in Chapters 3 and 4 as the second part of this work.

§ 1.3 Vorticity Source in the Flowfield of Jets in Crossflow

Since the major characteristics of the flowfield of jets in a crossflow are related to vortical kinematics and dynamics, it is important to discuss first what are the vorticity sources of this flowfield before going into a detailed discussion of the jet interaction and its structure.

In many of the papers which studied jets in a uniform crossflow, the vorticity present in the flowfield has been described as generated from the jet/free-stream

flow interaction; this is not only misleading but also physically wrong. By referring to the vorticity transport equation and the theoretical work of Wu et al. (1987), Fric and Roshko (1989) concluded that any new vorticity can only enter the flow through imposed initial conditions and/or wall boundary conditions; there is no source of new vorticity within the flow. This point is made clearer below.

By taking the curl of the Navier-Stokes equation and after some rearrangement, for constant first and second viscosities μ and μ_v, a general viscous, compressible vorticity equation was obtained (Thompson, 1984)

$$\begin{aligned}\frac{D\vec{\omega}}{Dt} =&(\vec{\omega}\cdot\nabla)\vec{V} - \vec{\omega}\,(\nabla\cdot\vec{V}) + \nabla T\times\nabla S + \nabla\times\vec{f}\\ &+\left(\mu_v+\frac{4}{3}\,\mu\right)\left[\nabla\left(\frac{1}{\rho}\right)\times\nabla(\nabla\cdot\vec{V})\right]\\ &+\mu\left[\frac{1}{\rho}\,\nabla^2\vec{\omega} - \nabla\left(\frac{1}{\rho}\right)\times(\nabla\times\vec{\omega})\right].\end{aligned} \tag{1.1}$$

For incompressible flow with a conservative body force, we have

$$\begin{aligned}\nabla\left(\frac{1}{\rho}\right) &= 0,\\ \nabla\cdot\vec{V} &= 0,\\ \nabla T\times\nabla S &= 0,\\ \nabla\times\vec{f} &= 0,\end{aligned}$$

and hence Eq. (1.1) reduces to the vorticity transport equation

$$\frac{D\vec{\omega}}{Dt} =(\vec{\omega}\cdot\nabla)\vec{V} + \nu\nabla^2\vec{\omega}. \tag{1.2}$$

Eq. (1.2) does not contain any vorticity generation terms, i.e., there is no vorticity source within the fluid. All vorticity in this flowfield must be generated on solid surfaces.

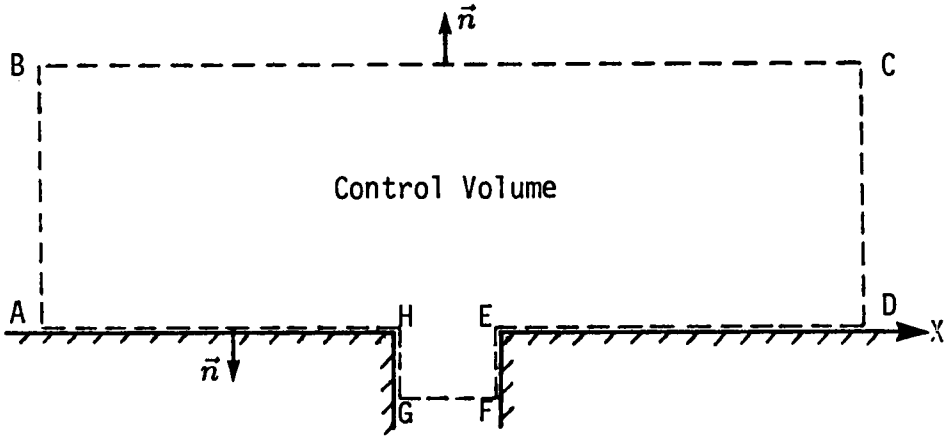


Figure 1.1 Schematic control volume.

Next, let us set a control volume with part of its boundary on solid surfaces as shown in Figure 1.1. An integration of Eq. (1.2) over this control volume leads to

$$\frac{\partial}{\partial t}\int_V \vec{\omega} dV = \int_{\partial V} \left[(\vec{n}\cdot\vec{\omega})\vec{V} - (\vec{n}\cdot\vec{V})\vec{\omega}\right] dS + \int_{\partial V} \nu \vec{n}\cdot\nabla\vec{\omega} dS, \qquad (1.3)$$

where $\vec{n}$ is an unit normal vector outward from the control surface. To determine the rate of vorticity increase inside the control volume we need only be concerned with the vorticity flux across its boundary because there is, as just stated, no source inside the control volume. On those boundaries which are inside the fluid (such as ABCD and FG in Fig. 1.1), the diffusion term $\int_{\partial V} \nu\vec{n}\cdot\nabla\vec{\omega} dS$ in (1.3) is effectively zero because $\vec{\omega}$ is almost a constant in the $\vec{n}$ direction. So the vorticity is brought into the control volume only by advection (the effect of the first term of Eq. (1.3)). On the other hand, the advection term $\int_{\partial V}\left[(\vec{n}\cdot\vec{\omega})\vec{V} - (\vec{n}\cdot\vec{V})\vec{\omega}\right] dS$ vanishes on the solid surfaces, hence vorticity is brought into the control volume by the diffusion term $\int_{\partial V} \nu\vec{n}\cdot\nabla\vec{\omega} dS$. It has been shown by Wu, Wu, and Wu (1987, 1988) that for an incompressible flow over stationary solid surfaces, the dynamic

vorticity flux

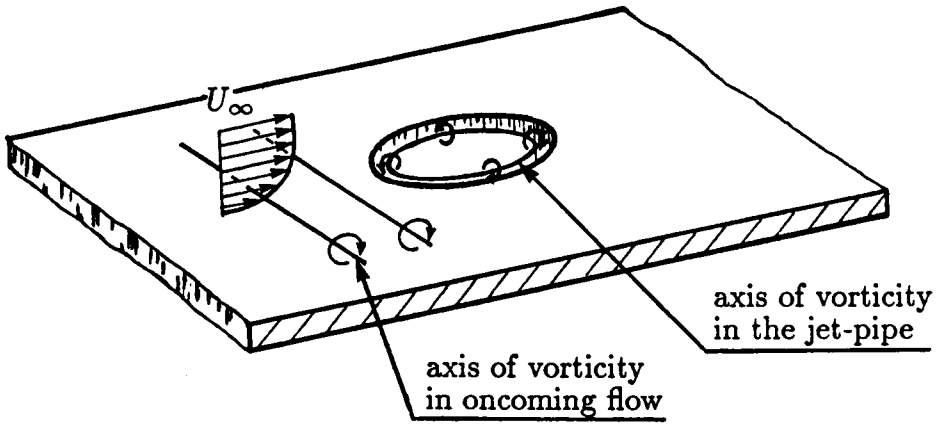
$$\vec{\sigma} = \vec{n} \cdot \nabla(\mu\vec{\omega}),$$

can be expressed as

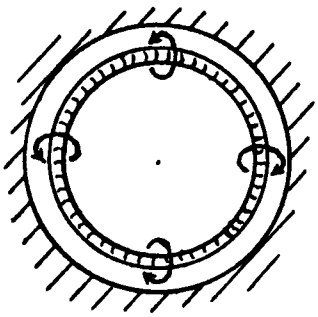
$$\vec{\sigma} = \vec{n} \times (\nabla p)_o + (\vec{n} \times \vec{\tau}_o) \cdot \nabla\vec{n} - \vec{n}\,[\vec{n} \cdot (\nabla \times \vec{\tau}_o)] \tag{1.4}$$

on solid boundaries, where subscript $(\ )_o$ indicates values on the solid boundary. On the right-hand side of Eq. (1.4), the first term $\vec{n} \times (\nabla p)_o$ is the vorticity flux due to the tangential pressure gradient. Indeed, Lighthill (1963) has pointed out earlier that the vorticity production mechanism is due to this term. Since there is a large pressure gradient with various directions on the solid surface near the jet orifice, this term introduces a large amount of vorticity into the fluid. The second term $(\vec{n} \times \vec{\tau}_o) \cdot \nabla\vec{n}$ is the vorticity flux due to the wall curvature. A large amount of vorticity is also brought into the fluid by this term because of the wall curvature of the jet-pipe, especially since the curvature approaches infinity at the edge of jet-orifice (see Figure 1.2). The third term $-\vec{n}\,[\vec{n} \cdot (\nabla \times \vec{\tau}_o)]$ accounts for the normal component of the curl of the wall shear stress which, according to Ref. [69, 70], introduces large vorticity flux near any separation or attachment line, in particular around spiral points. As we will see later, separations, attachments, and spiral points are common phenomena in the flowfield of a jet in a crossflow, therefore the third term of Eq. (1.4) is also important for our problem. Figure 1.2 shows the vorticity orientation next to the solid surfaces.

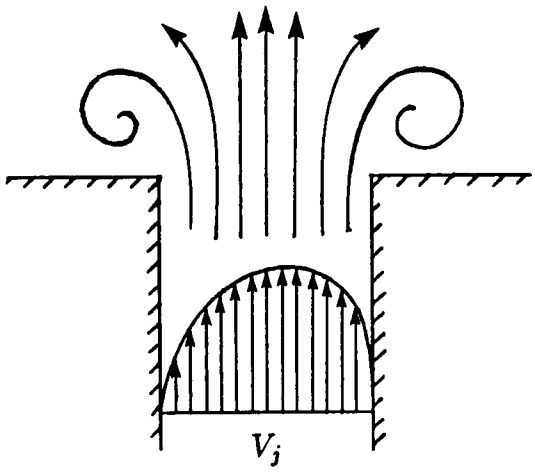
From the above discussion, it is clear that although there is no vorticity source within the fluid, a large amount of vorticity generated from the solid surfaces will be brought into it by the diffusion process. The vorticity then, of course, is advected by the jet flow and the crossflow, and evolves to form many strong, concentrated vortices mainly due to the first term on the right-hand side of Eq. (1.2).



(a). vorticity orientation on solid surfaces



(b). a cross-section view of jet-pipe



(c). a vertical-section view of jet-pipe

Figure 1.2 Vorticity orientation next to the solid surfaces.

CHAPTER II

NUMERICAL SOLUTION

Due to the complexity and true three-dimensional nature of the jet in crossflow problem, it is necessary to obtain a solution from the full Navier-Stokes equations in order to correctly represent the true nature of this flow. In this chapter, a three-dimensional numerical solution for unsteady, incompressible Navier-Stokes equations was developed for a single jet issuing normally into a uniform crossflow. Jet exits of various shape were adopted in this study. Laminar flow was assumed for all the calculations reported herein. The solutions for the circular jet case were produced first and compared with the reported experimental results to check the quality of the simulation. The main focus was on computing the flowfield of non-circular, non-symmetric jets in crossflow. It should be pointed out here, however, that experimental data was always for turbulent jets and approaching boundary layer. For this reason it is not possible to expect detailed quantitative agreement between computation and experiment.

§ 2.1 Governing Differential Equations

For the unsteady, three-dimensional, incompressible flow field in and around the deflected jet, the governing differential equations in Cartesian Coordinates are:

continuity:

$$\frac{\partial u}{\partial x} + \frac{\partial v}{\partial y} + \frac{\partial w}{\partial z} = 0. \tag{2.1}$$

momentum:

$$\frac{\partial u}{\partial t} + u\frac{\partial u}{\partial x} + v\frac{\partial u}{\partial y} + w\frac{\partial u}{\partial z} = -\frac{\partial p}{\partial x} + \nu(\frac{\partial^2 u}{\partial x^2} + \frac{\partial^2 u}{\partial y^2} + \frac{\partial^2 u}{\partial z^2}), \tag{2.2}$$

$$\frac{\partial v}{\partial t} + u\frac{\partial v}{\partial x} + v\frac{\partial v}{\partial y} + w\frac{\partial v}{\partial z} = -\frac{\partial p}{\partial y} + \nu(\frac{\partial^2 v}{\partial x^2} + \frac{\partial^2 v}{\partial y^2} + \frac{\partial^2 v}{\partial z^2}), \tag{2.3}$$

$$\frac{\partial w}{\partial t} + u\frac{\partial w}{\partial x} + v\frac{\partial w}{\partial y} + w\frac{\partial w}{\partial z} = -\frac{\partial p}{\partial z} + \nu(\frac{\partial^2 w}{\partial x^2} + \frac{\partial^2 w}{\partial y^2} + \frac{\partial^2 w}{\partial z^2}), \tag{2.4}$$

where, the body force has been neglected*, p is the fluid pressure divided by the constant density, and the kinematic viscosity ν is assumed to be a constant.

§ 2.2 Numerical Approximation

The solution algorithm used in the present work was SOLA (Solution Algorithm), which is a simple, straightforward numerical algorithm for incompressible flow. From the original 2-D program presented in reference [26, 27], the author developed the 3-D computer code used for the present computations.

A. Computational Grids

The finite-difference mesh used for numerically solving equations (2.1) to (2.4) consists of block cells of width δx_i, depth δy_j, and height δz_k. The active mesh region has $IBAR$ cells in the x-direction labeled with the index i, $JBAR$ cells in the y-direction labeled with the index j, and $KBAR$ cells in the z-direction labeled with the index k (see Figures 2.1 and 2.2). This region is surrounded by

---

* As the same fluid properties are assumed for both the free-stream and the jet fluid, no body force is needed.

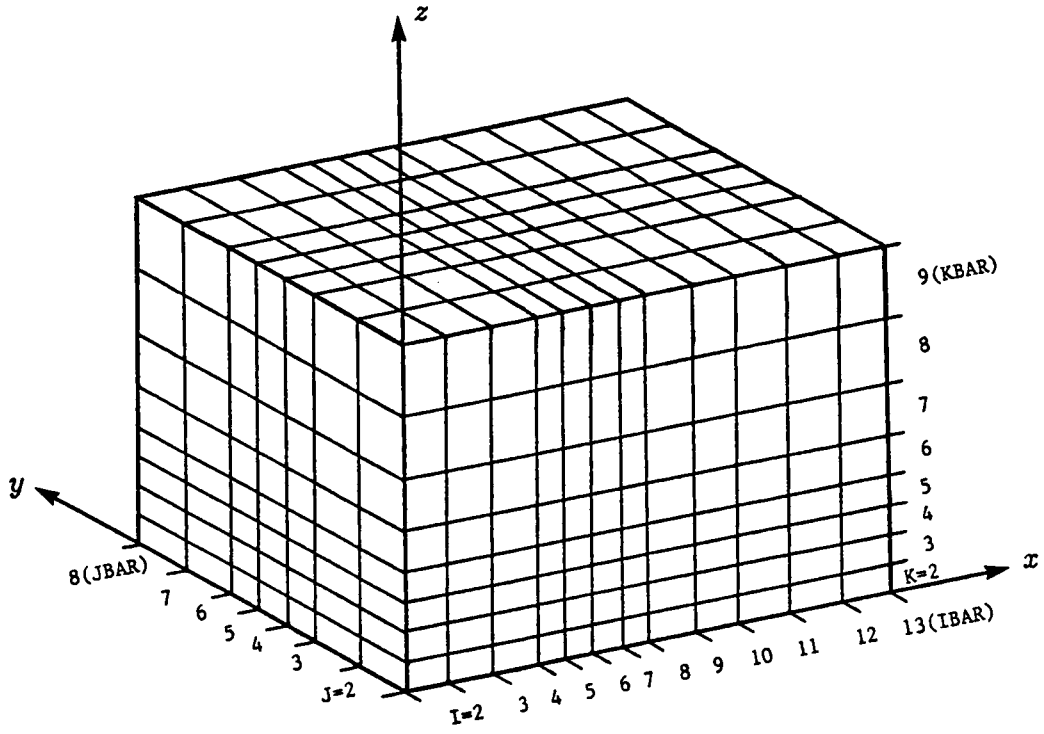


Figure 2.1 Computational mesh layout.

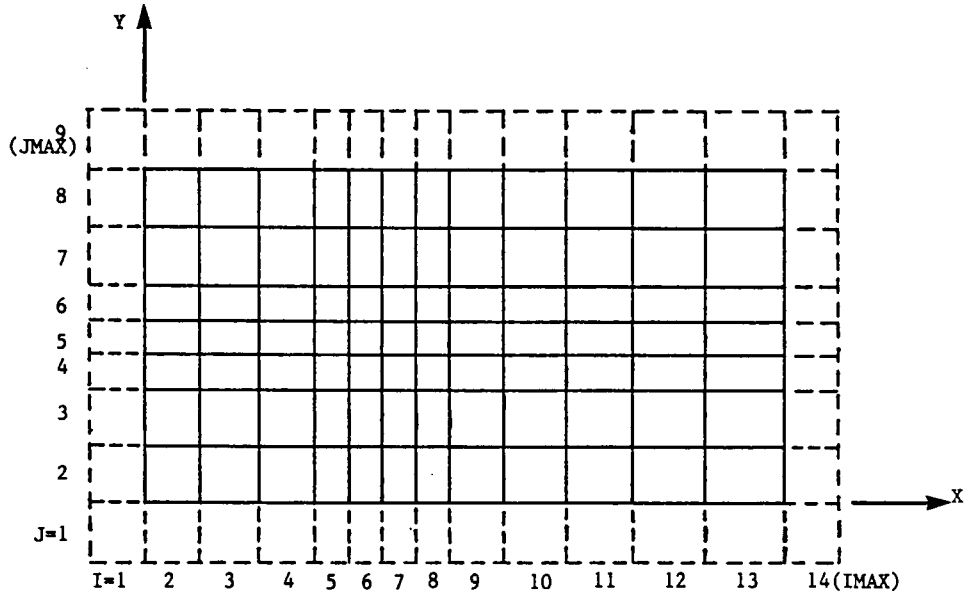


Figure 2.2 Two–dimensional mesh slice in normal to z–direction (the boundary cells are shown with dashed lines).

a layer of boundary cells used to set mesh boundary conditions. Thus, there are a total of $(IBAR+2)\times(JBAR+2)\times(KBAR+2)$ cells in the complete mesh. Figure 2.2 shows the placement of the boundary cells, which are shown as dashed lines, for a slice of the mesh normal to the z–direction.

The computer program has the capability of handling a non-uniform grid spacing. In each direction, fine grid spacing was employed near the injection location and gradually increased for locations away from the jet exit. The algorithm used in this work was first-order accurate in both space and time.

A typical mesh cell is shown in Figure 2.3. The cell-centered pressure is written as $p^n_{i,j,k}$ where the superscript n refers to the n^{th} time step value. The fluid velocity component in the x–direction, which is denoted by $u_{i,j,k}$, is located

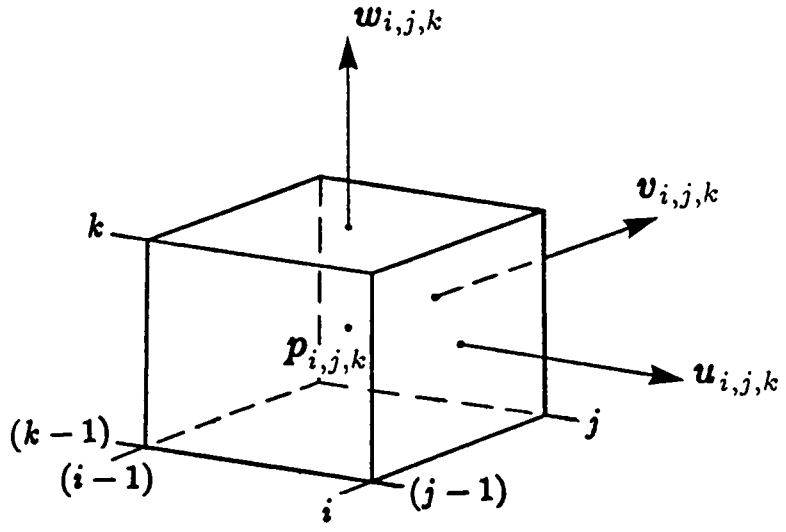


Figure 2.3 A typical mesh cell with the locations of the flow variables.

on the cell face between cells (i,j,k) and $(i+1,j,k)$. The velocity components $v_{i,j,k}$ and $w_{i,j,k}$ are defined similarly for the y and z directions. Thus,

$p^n_{i,j,k}$ = pressure at center of cell (i,j,k) at time level n,

$u^n_{i,j,k}$ = x–direction velocity component at the middle of the positive x cell face at time level n,

$v^n_{i,j,k}$ = y–direction velocity component at the middle of the positive y cell face at time level n,

$w^n_{i,j,k}$ = z-direction velocity component at the middle of the positive z cell face at time level n.

B. Finite Difference Approximation

Using the mesh index convention defined above, a generic form for the finite-difference approximations of equations (2.1) to (2.4) are:

$$\frac{u_{i,j,k} - u_{i-1,j,k}}{\delta x_i} + \frac{v_{i,j,k} - v_{i,j-1,k}}{\delta y_j} + \frac{w_{i,j,k} - w_{i,j,k-1}}{\delta z_k} = 0, \tag{2.5}$$

$$u^{n+1}_{i,j,k} = u^n_{i,j,k} + \delta t \left[-\frac{p^{n+1}_{i+1,j,k} - p^{n+1}_{i,j,k}}{\delta x_{i+1/2}} - FUX - FUY - FUZ + VISX \right], \tag{2.6}$$

$$v^{n+1}_{i,j,k} = v^n_{i,j,k} + \delta t \left[-\frac{p^{n+1}_{i,j+1,k} - p^{n+1}_{i,j,k}}{\delta y_{i+1/2}} - FVX - FVY - FVZ + VISY \right], \tag{2.7}$$

$$w^{n+1}_{i,j,k} = w^n_{i,j,k} + \delta t \left[-\frac{p^{n+1}_{i,j,k+1} - p^{n+1}_{i,j,k}}{\delta z_{i+1/2}} - FWX - FWY - FWZ + VISZ \right], \tag{2.8}$$

where, for example, $\delta x_{i+1/2} = (\delta x_i + \delta x_{i+1})/2$, FUX means the advective flux of u in the x–direction, $u(\partial u/\partial x)$, FUY means the advective flux of u in the y–direction, and $VISX$ is the x–component viscous acceleration term, $\nu(\partial^2 u/\partial x^2 + \partial^2 v/\partial y^2 + \partial^2 w/\partial z^2)$, etc. All the advective and viscous terms in Eq. (2.6) to (2.8) were evaluated using the n^{th} time level values.

The approximation of the advective terms were made by a combination of the donor-cell with a centered-difference approximation into a single expression with a parameter $\tilde{\alpha}$, which controls the relative amount of each one. The general form for FUX, for example, is

$$FUX = (u_e/\delta x_{\tilde{\alpha}})\,[DUL\delta x_{i+1} + DUR\delta x_i + \tilde{\alpha} sgn(u_e)(DUL\delta x_{i+1} - DUR\delta x_i)]\,, \tag{2.9}$$

where, u_e is the value of u at the location where FUX is evaluated and

$$DUL = (u_{i,j,k} - u_{i-1,j,k})/\delta x_i,$$

$$DUR = (u_{i+1,j,k} - u_{i,j,k})/\delta x_{i+1},$$

with:

$$\delta x_{\tilde{\alpha}} = \delta x_{i+1} + \delta x_i + \tilde{\alpha} sgn(u_e)(\delta x_{i+1} - \delta x_i),$$

and $sgn(u_e)$ means the sign of u_e. When $\tilde{\alpha}$=0, Eq. (2.9) reduces to a second-order accurate centered-difference approximation. When $\tilde{\alpha}$=1, the first-order donor-cell approximation was recovered. This type of approximation scheme was used for all advective terms in Eq. (2.6) to (2.8). All other terms in those equations were approximated by the standard centered difference.

§ 2.3 Solution Procedure

The pressures at the time level n+1 were unknown at the beginning of the time cycle, so Eq. (2.6) to (2.8) could not be used directly to evaluate the n+1 level velocities. Thus the basic procedure for advancing a solution through one time step had to consist of two steps:

(1) In the first step, the p^{n+1} values in equation (2.6) to (2.8) were replaced by p^n value to compute the first guess for new time level velocities.

(2) The velocities computed from step (1) would not satisfy the approximation form of the continuity equation

$$\frac{u_{i,j,k} - u_{i-1,j,k}}{\delta x_i} + \frac{v_{i,j,k} - v_{i,j-1,k}}{\delta y_j} + \frac{w_{i,j,k} - w_{i,j,k-1}}{\delta z_k} = 0. \qquad (2.5)$$

To satisfy this condition, the pressure must be suitably adjusted in each cell. The pressure change needed to drive $\nabla \cdot \vec{V}$ to zero is

$$\delta p = -\frac{\omega(\nabla \cdot \vec{V})}{2\delta t(1/\delta x^2 + 1/\delta y^2 + 1/\delta z^2)},$$

where ω is an over-relaxation parameter ($1 < \omega < 2$). Once δp was determined, the cell pressure was updated to $(p_{i,j,k} + \delta p)$ and the velocities were also updated to reflect this change,

$$u_{i,j,k} \ \ to \ \ u_{i,j,k} \pm \delta t \delta p_{i,j,k}/\delta x_i$$

$$v_{i,j,k} \ \ to \ \ v_{i,j,k} \pm \delta t \delta p_{i,j,k}/\delta y_j$$

$$w_{i,j,k} \ \ to \ \ w_{i,j,k} \pm \delta t \delta p_{i,j,k}/\delta z_k$$

The pressure adjustments had to be done iteratively, because the change in one cell would upset the balance in its six neighboring cells. The iteration process was carried out until a convergence criterion

$$|\nabla \cdot \vec{V}| \leq \epsilon$$

was satisfied for all cells, where ϵ is a small preset value. Figure 2.4 shows a typical convergence process for the present computation. Through compromise between

the accuracy and the computational time, a typical value of $\epsilon = 10^{-3}$ was used for most of the computation.

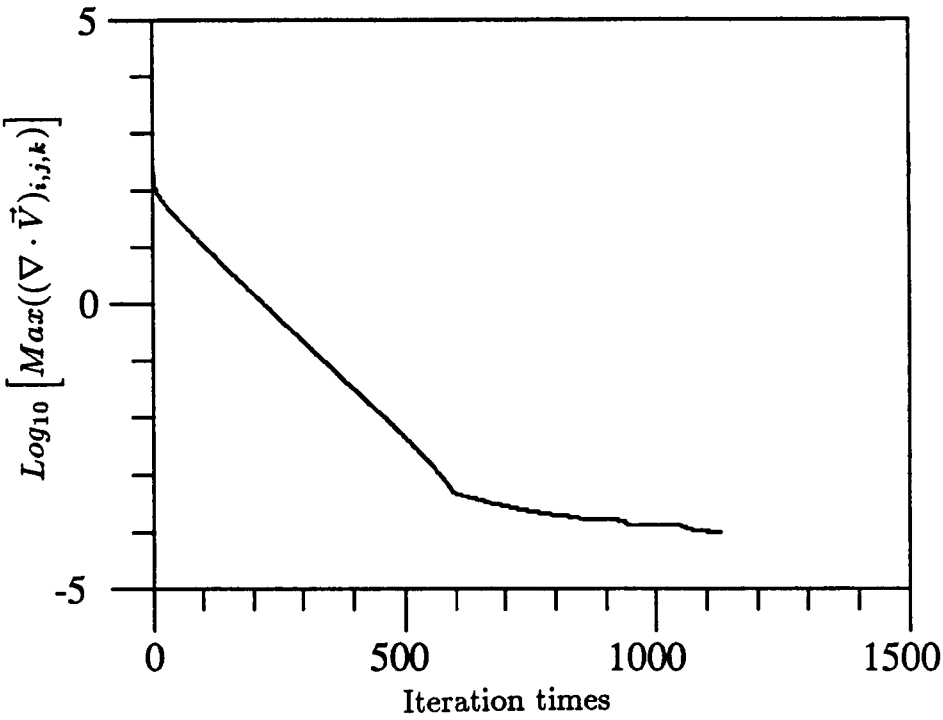


Figure 2.4 A typical convergence process ($R = 4$ circular jet, $t = 3.35$).

After the convergence was achieved, the time step was then advanced to $t_{n+2} = t_{n+1} + \delta t$ and the pressure and velocities at t_{n+1} were used as the starting values for the computation of the new time step t_{n+2}.

By repeating the above process, the solution would be advanced through a desired time interval. At each time step, suitable boundary conditions must be imposed at all boundary mesh-cells. The computational flow chart is presented in Figure 2.5.

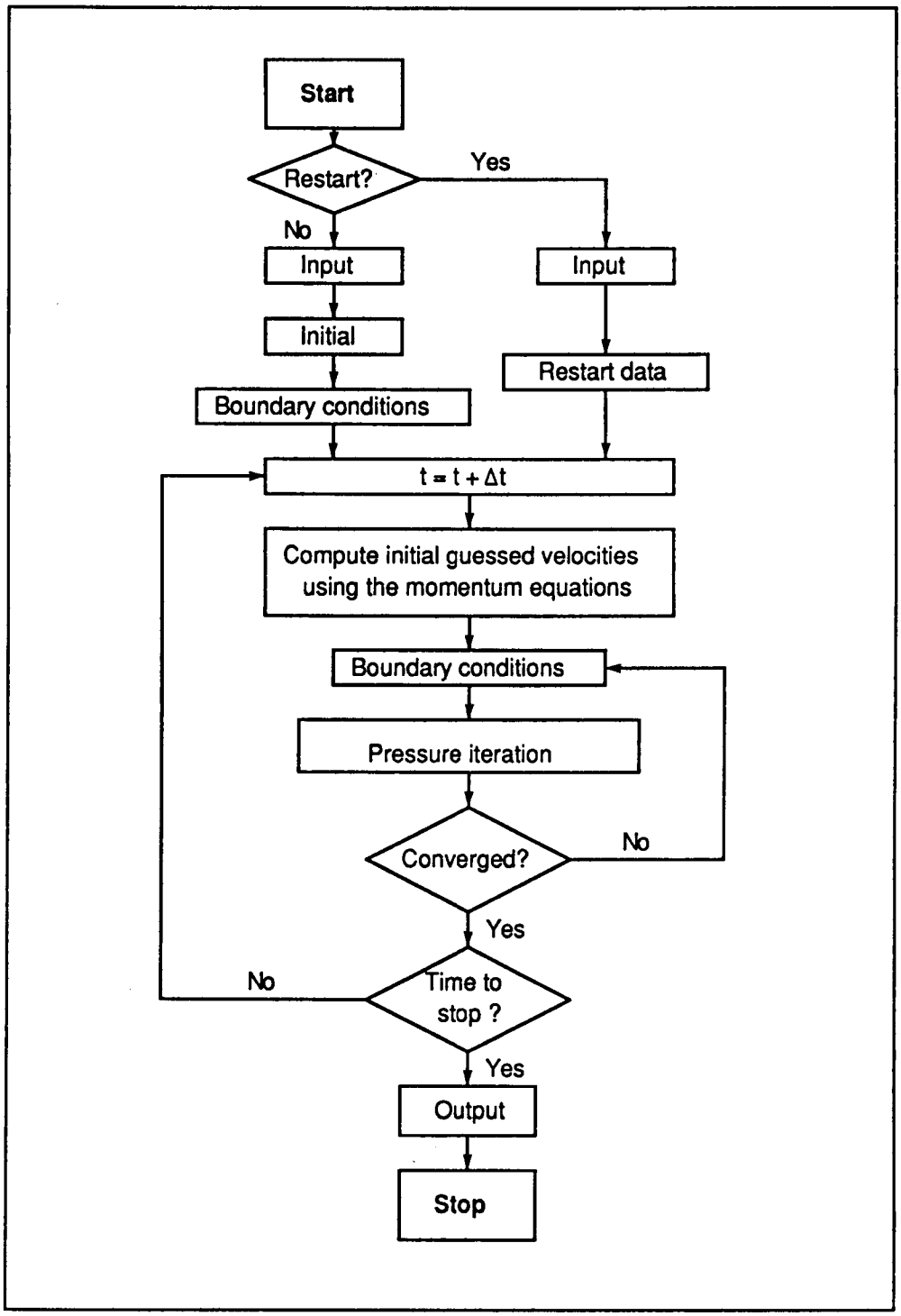


Figure 2.5 Computational flow chart.

§ 2.4 Computational Setting and Boundary Conditions

The computational domain adopted was a rectangular block as shown in Figure 2.6. The number of the grid planes used for most of the computations in the present work was 80 × 80 × 45, that led the computational domain to be $15D$, $15D$, and $20D$ in the x, y, and z directions respectively for the circular jet case, where D is the circular jet diameter.

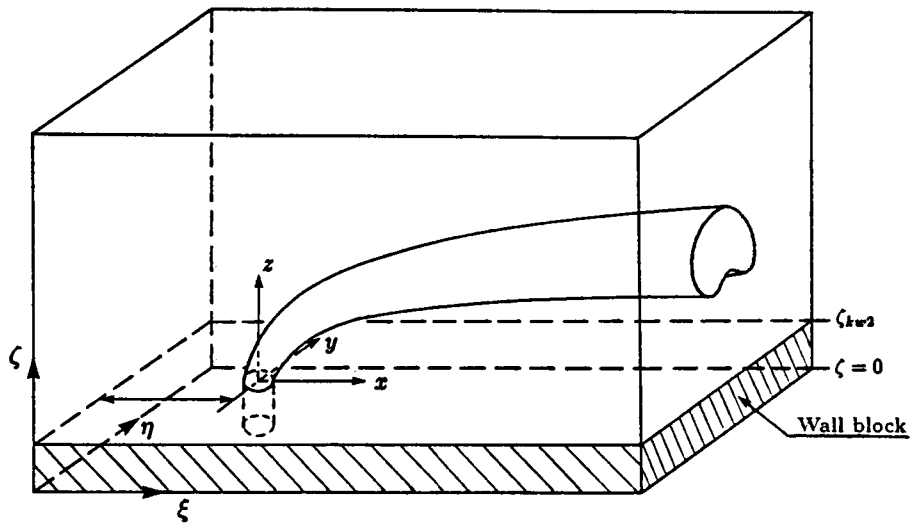


Figure 2.6 The layout of the computational setting.

Figure 2.6 shows the layout of the computational setting, where (ξ, η, ζ) are the computational coordinates and (x, y, z) the physical coordinates. The jet's center was located on the central plane in the y–direction (at $y = 0$) and 3.0 diameters downstream from the $\xi = 0$ plane (the left edge of the computational domain). The jet cross-section was constructed by specially arranged mesh cells for different shapes of the jet orifices (this will be discussed for individual cases later). For a better modeling of the real case, the jet was given a 1.5 jet-diameter depth because experiments (Reference [3]) have shown that the crossflow can affect

the flow in the jet-pipe up to two to three pipe-diameters deep depending on the jet-to-crossflow velocity ratio. This requirement was achieved by setting a wall-block from $\zeta = 0$ to $\zeta = \zeta_{kw2}$ except at the jet passage as shown in Figure 2.6, with the result that the actual channel area was $15D \times 15D \times 20D$ for the circular jet case. Figure 2.7 shows the nomenclatures used for the non-circular, asymmetrically placed jet orientation.

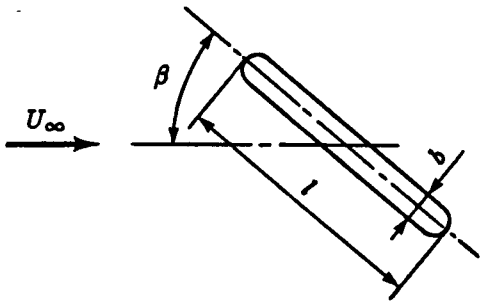


Figure 2.7 Sketch of non-circular, asymmetrically placed jet orientation.

The upstream, downstream, upper, and side boundary conditions were imposed by setting appropriate velocities in the fictitious cells surrounding the computational domain in the following manner:

(1). Upstream ($\xi = 0$) boundary condition:

For the channel entrance, a uniform flow boundary condition was specified, i.e., $u = U_o$, $v = w = 0$.

(2). Downstream ($\xi = \xi_{max}$) boundary condition:

Because of the highly three-dimensional nature of the problem, parallel flow would not be re-established for a very long distance downstream from the jet exit. So, what was needed for the downstream boundary condition was a prescription that permits fluid to flow out of the computational domain freely. For that reason, the extrapolation

$$Q^{n+1}_{imax,j,k} = 2Q^{n}_{imax-1,j,k} - Q^{n}_{imax-2,j,k}$$

was used for the downstream boundary, where Q is the computed flow velocities u, v, and w.

(3). Side boundaries ($\eta = 0$ and $\eta = \eta_{max}$):

Available experiments have shown that the lateral distance affected by the jet are rather limited, so the zero normal flow gradient condition was used for both side boundaries.

(4). Upper boundary condition ($\zeta = \zeta_{max}$):

The upper boundary was considered as a flat, fixed surface with velocity slip, i.e., $w = 0$. It was realized during the test stage, however, that the height of the computational domain largely affects the jet penetration into the free-stream, and hence affects the whole flowfield. For this reason a $20D$ height was used for all the computations.

The jet boundary condition was imposed by setting the jet inlet condition and the wall-block condition such that,

(5). Bottom wall-block boundary condition ($\zeta = 0$ to $\zeta = \zeta_{kw2}$):

All the velocities within this wall-block were set to be zero, i.e., $u = v = w = 0$, except for the jet passage, in which the velocities were calculated to be the same as those inside of the cannel.

(6). Jet inlet condition ($\zeta = 0$ and within the jet cross-section):

At the jet inlet, which was laid on the $\zeta = 0$ plane, a uniform velocity distribution, V_j=constant, was imposed over the inner points but satisfied the no-slip boundary condition on the pipe wall (in the sense of the discrete geometry).

The jet boundary conditions (5) and (6) automatically imply the non-slip condition on the bottom surface of the channel.

§ 2.5 Numerical Results and Discussion

Calculations were performed on the Alliant mini-super computer at the University of Tennessee Space Institute (UTSI). Computations required 2×10^{-5} CPU seconds/iteration/grid point. For most of the computations, a time step $\delta t = 0.01$, a relative factor $\tilde{\alpha} = 0.8$, and a over-relaxation parameter $\omega = 1.3$ to 1.7 were used to obtain the solutions.

A. Circular Jets

The circular jet cases were computed for two purposes. First, because there is much available experimental data for a circular jet in crossflow, the solutions for these cases could be used to check the quality of the simulation. Second, some phenomena, especially those related to vortex dynamics of a circular jet in crossflow, still remain to be explored or confirmed. The present computational results would help us to have a better understanding of this type of flow.

The circular jet orifice was approximated by a right-angled polygon of nearly equal area in the Cartesian grid system as shown in Figure 2.8. Those cells with

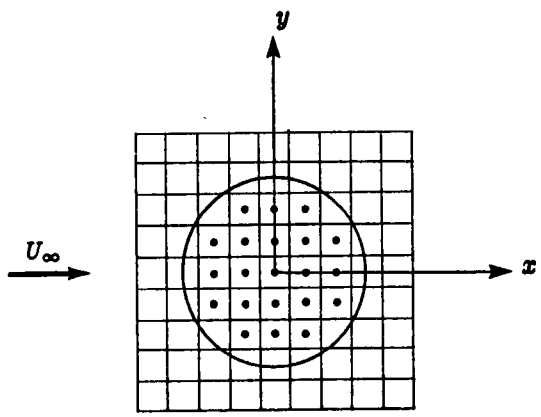


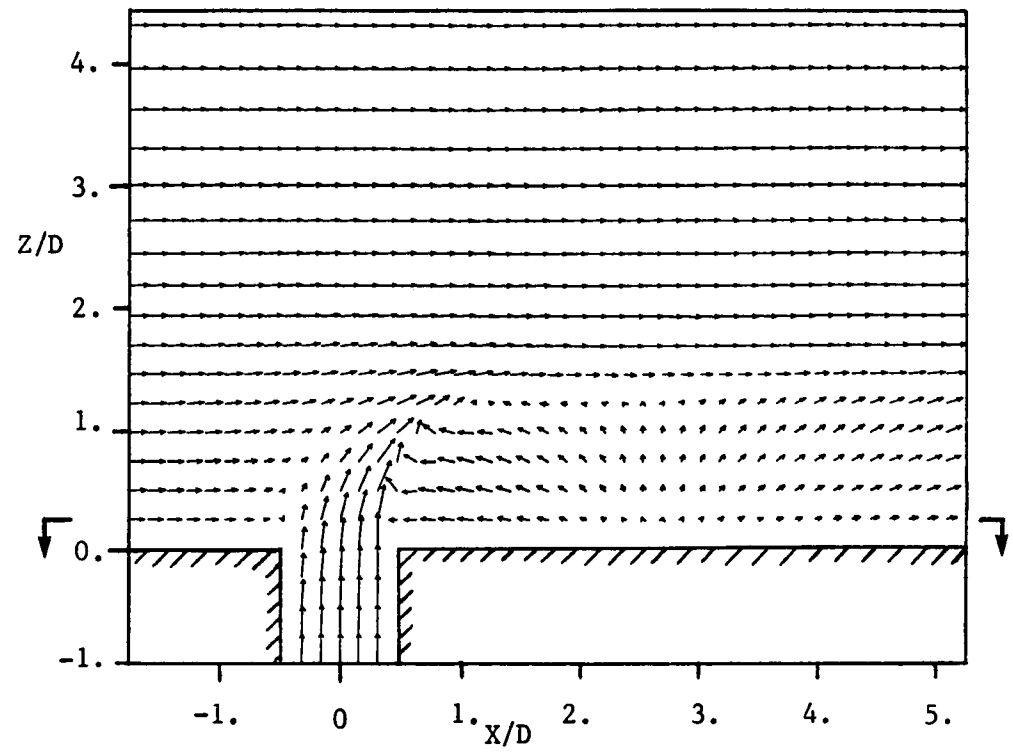
Figure 2.8 Grid structure used to approximate the circular jet orifice.

dark dots were the cells where the jet inlet velocity was imposed. As only 21 grid points fall on the jet cross-section, the simulation of the jet is rather coarse. The jet's non-dimensional cross-section area was taken approximately equal to unity. The Reynolds number based on the free-stream velocity and the jet-diameter was of the order of 5×10^4. Because of the availability of experimental data, jet-to-crossflow velocity ratios of $R = 2$ and 4 were used for the circular jet computations.

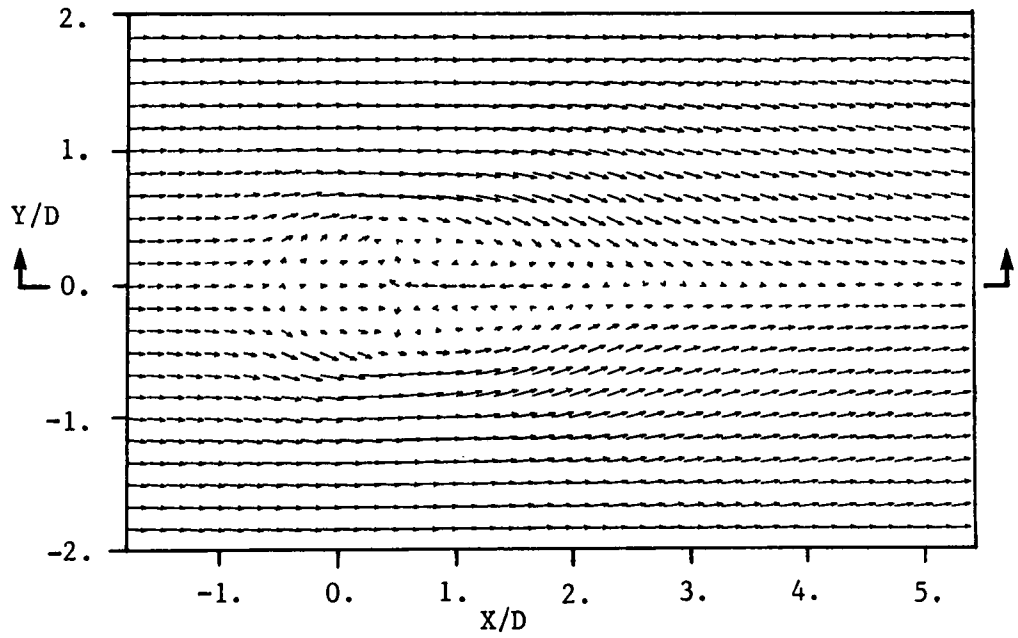
A.1. Circular Jet with Velocity Ratio $R = 2$

Selected velocity vector plots for a circular jet in a crossflow with $R = 2$ are presented in Figure 2.9. The vertical plane view, which was cut on the $y = 0$ plane, shows the oncoming flow, the deflected jet plume, and the reverse flow region behind the jet. Just upstream of the jet exit and close to the bottom surface, a downwards velocity vector suggests that a small flow separation has occurred right in front of the jet exit. This phenomenon became even clearer in higher jet-to-crossflow velocity ratio cases as we will see later. Figure 2.10 is a schematic of experimental results due to Foss (1980) and many flow features shown in this figure were captured by computation.

The horizontal plane view, which was cut parallel to the bottom plate, gives a better picture of the reversed flow region. Near the cannel bottom wall, the oncoming flow moved around the jet plume and formed two shear layers on each side of it. On the lee-side of the jet, the crossflow near the wall spiraled into the lower pressure region behind the jet and formed two large vortices in the wake. In Figure 2.9 (b), a saddle point associated with this separated flow can be seen near $x = 2.5D$. The crossflow boundary layer vorticity was reoriented along an axis inclined away from the wall, they were then free to stretch and turn to evolve into the vertical wake vortices (see Figure 2.10). Since the flow in this region was

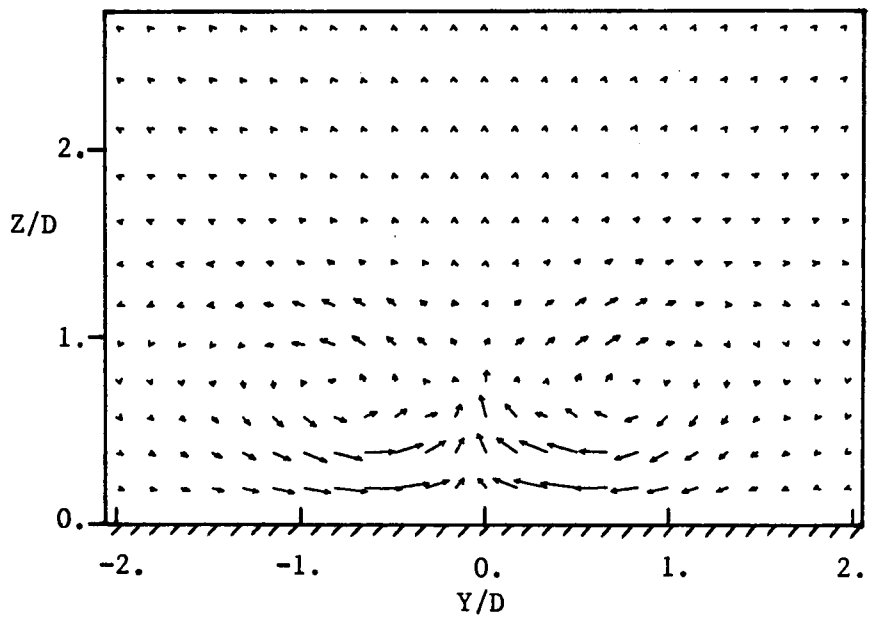


(a). vertical plane ($y = 0$)



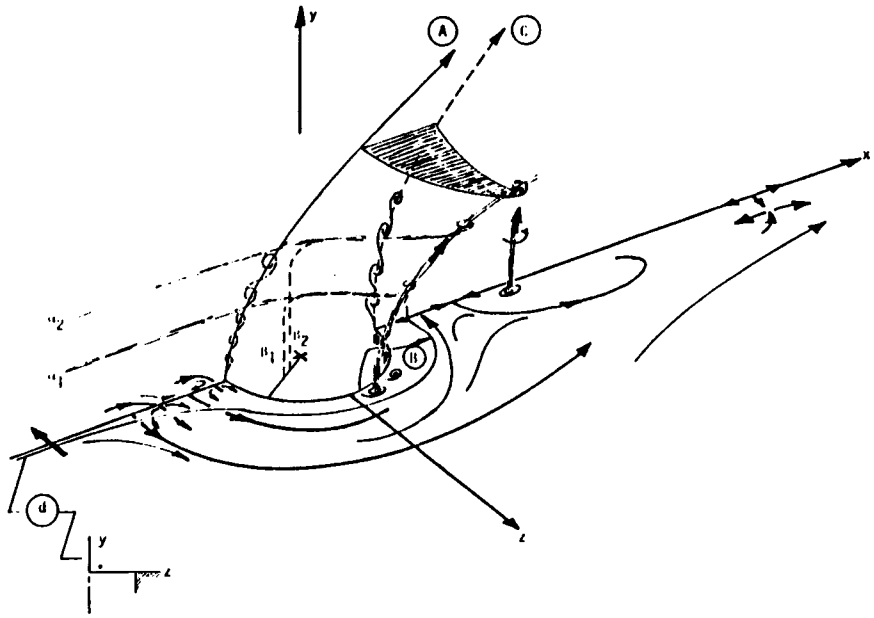
(b). horizontal plane ($Z/D = 0.25$)

Figure 2.9 The sectional velocity vectors for a circular jet ($R = 2$, t=1.0).

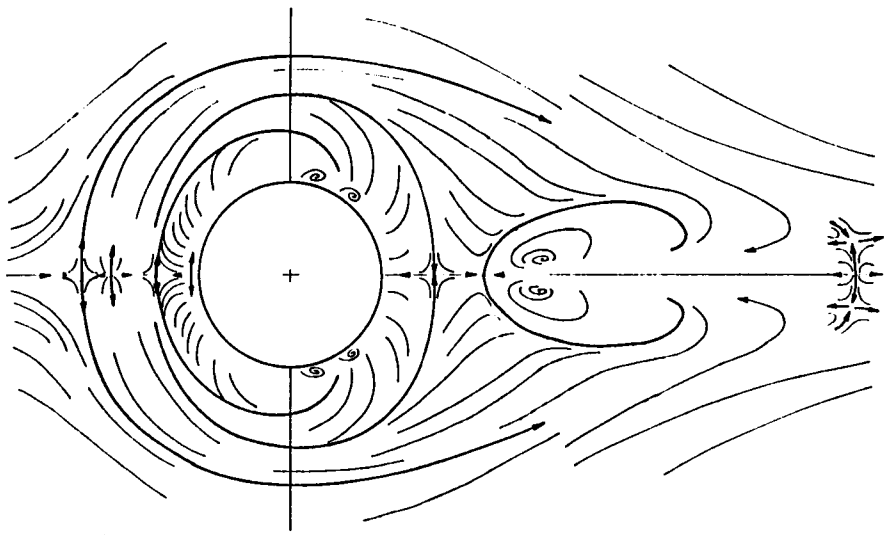


(c). cross-section plane (X/D = 2)

Figure 2.9 (continued).



(a). schematic representation of the flow field



(b). wall shear stress pattern

Figure 2.10 The schematic flow field of jet in a crossflow for $R = 1.5$ (Foss, 1980).

qualitatively similar in appearance to that in the wake of a solid cylinder, some authors concluded that these two flow fields have the same mechanism. Such an analogy is physically wrong and misleading; it leads to an incorrect explanation of the jet wake formation process. In the solid cylinder case, the wake vorticity is generated from the solid surface of the cylinder. Since the jet does not offer a solid surface to the crossflow, as a solid cylinder does, the vorticity in the jet's wake can only be generated from the bottom wall of the crossflow or from the jet-pipe wall. And according to the experiments in Reference [22], the source of the wake vortices is the vorticity generated on the crossflow wall.

A qualitative discussion of how these vortices are formed from the existing vorticity field may help us to further understand this matter. The most significant mechanism for the the formation of wake vortices is the non-linear interaction between the velocity gradient and the vorticity. Mathematically, it is the term containing the rate-of-vortex-deformation, $(\vec{\omega} \cdot \nabla)\vec{V}$ (the first term on the right-hand side of Eq. (1.2)), that is responsible for such an interaction.

Using the notation in Reference [39] (pp. 145-147), write

$$(\vec{\omega} \cdot \nabla)\vec{V} = \vec{\omega} \cdot D + \vec{\omega} \cdot W, \tag{2.10}$$

where, D is the rate-of-deformation tensor,

$$D = \frac{1}{2}(u_{i,j} + u_{j,i}),$$

and W is the spin tensor,

$$W = \frac{1}{2}(u_{i,j} - u_{j,i}) = \frac{1}{2}\epsilon_{ijk}\omega_k.$$

It may be noted that D is symmetric and W is skew. Since the vorticity vector is in the kernel of W (as a map on three dimensional space), there is no contribution

from the term $(\vec{\omega} \cdot W)$, i.e.,

$$\vec{\omega} \cdot W = \frac{1}{2}\omega_i \epsilon_{ijk} \omega_k = 0,$$

Eq. (2.10) then reduces to

$$(\vec{\omega} \cdot \nabla)\vec{V} = \vec{\omega} \cdot D. \tag{2.11}$$

Our main concern is in the region next to the sides of the jet, where the major interaction takes place. In the crossflow boundary layer, the vorticity, ω, has mostly a ω_y component (and $\omega_y > 0$), we can approximate $\vec{\omega}$ as

$$\vec{\omega} \sim (0,\ \omega_y,\ 0),$$

so that Eq. (2.11) can be written as

$$(\vec{\omega} \cdot \nabla)\vec{V} = \vec{\omega} \cdot D \sim \omega_y \begin{pmatrix} \frac{1}{2}(\partial u/\partial y + \partial v/\partial x) \\ \partial v/\partial y \\ \frac{1}{2}(\partial v/\partial z + \partial w/\partial y) \end{pmatrix}. \tag{2.12}$$

An order-of-magnitude analysis gives (refer to Figure 2.11)

$$\partial v/\partial x \sim 0, \quad \partial v/\partial y \sim 0, \quad \partial v/\partial z \sim 0,$$

$$\partial u/\partial y \sim (U_\infty/d), \quad \partial w/\partial y \sim (V_j/d).$$

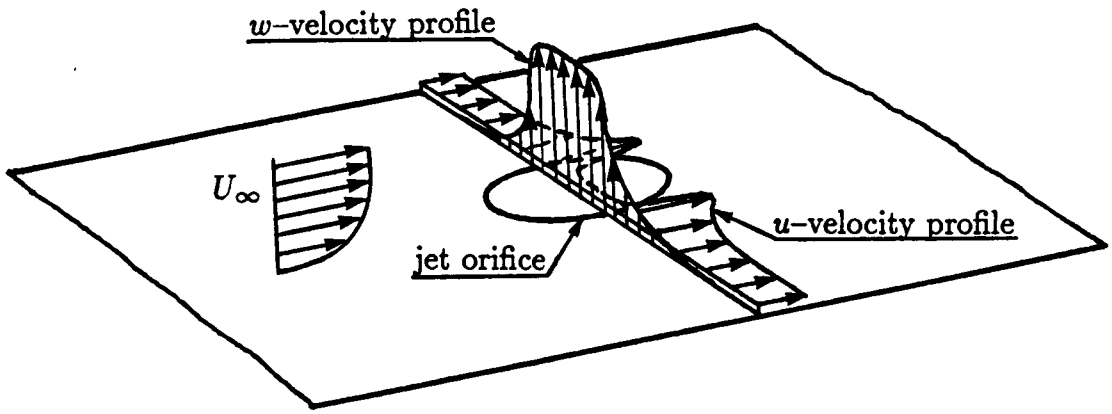


Figure 2.11 Schematic of the velocity profiles near the jet-orifice.

Hence

$$(\vec{\omega}\cdot\nabla)\vec{V} \sim \frac{1}{2}\omega_y(\partial u/\partial y\ \vec{i} + \partial w/\partial y\ \vec{k}).$$

By referring to Figure 2.11 (a), the sign of these velocity derivatives can be decided. On the Y^- side, $\partial u/\partial y > 0$ and $\partial w/\partial y > 0$, so

$$(\vec{\omega}\cdot\nabla)\vec{V} \sim \frac{1}{2}\omega_y((U_\infty/d)\ \vec{i} + (V_j/d)\ \vec{k}).$$

Applying the same argument to the Y^+ side leads to

$$(\vec{\omega}\cdot\nabla)\vec{V} \sim \frac{1}{2}\omega_y(-(U_\infty/d)\ \vec{i} - (V_j/d)\ \vec{k}).$$

Writing in a single expression, we have

$$(\vec{\omega}\cdot\nabla)\vec{V} \sim \mp\frac{U_\infty}{2d}\omega_y(\vec{i} + R\ \vec{k}) \quad for \quad \begin{matrix} y > 0 \\ y < 0 \end{matrix}, \tag{2.13}$$

where, $R = V_j/U_\infty$ is the jet-to-crossflow velocity ratio. From the above discussion, it is realized that on the side of the jet, a large amount of crossflow vorticity will be reoriented to have both x and z components, and so form the concentrated wake vortices as sketched in Figure 2.12. The directions of the axis of these vortices

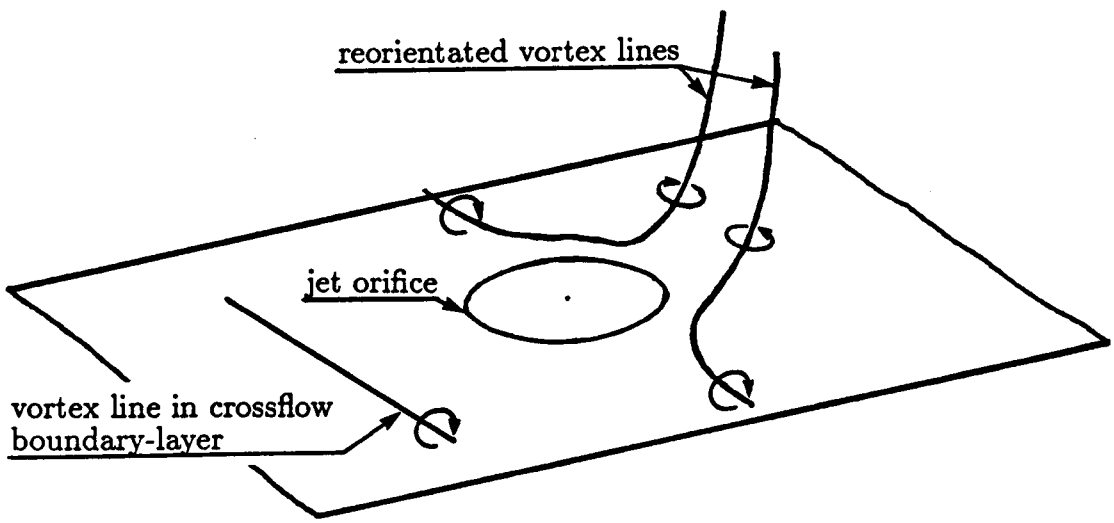


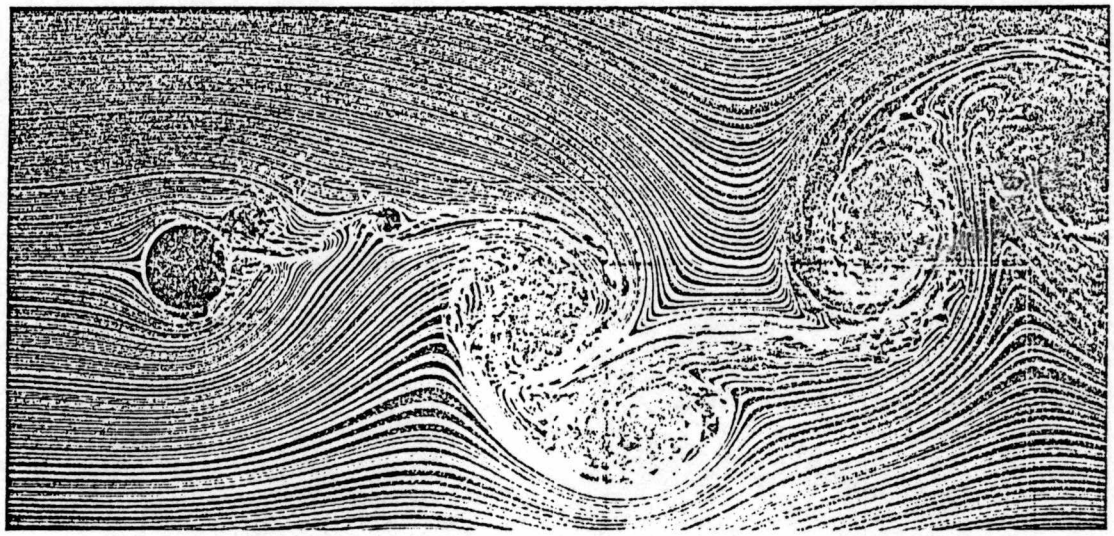
Figure 2.12 The reorientation of the crossflow boundary-layer vorticity.

will depend directly on the velocity ratio R; the vortices will be more aligned with the z–direction for large R. This qualitative conclusion agrees very well with the computed and experimental results. Figure 2.13 (a) and (b) are two photographs from different experiments which show the features of the wake vortices as we have discussed above.

A counter-rotating vortex pair can be seen in cross-sectional view, Figure 2.9 (c), which was cut normally to the y–direction. This vortex pair evolved from the shear layer vorticity inside the jet-pipe, that is, the jet's cylindrical vorticity sheet which is shown schematically in Figure 1.2 (p.10). The counter-rotating vortex pair started to form on both the Y^+ and the Y^- sides of the jet plume immediately after leaving the jet-pipe and developed quickly within a short distance (0.5 to 1.0 jet diameter). This counter-rotating vortex pair become the dominating phenomenon of the jet flow structure as it passes downstream. As a comparison, Figure 2.14 presents a laser induced fluorescence sectional view of a circular jet at $X/D = 3$ taken by Yu (1987). The qualitative similarity between the computed and experimental results is obvious. Since the intersecting angle between the laser sheet and the bottom plate was 45°, the real height of the vortex center should be scaled by the factor $1/\sqrt{2}$.

The computed results indeed gave a global picture very similar to the experimental results such as the one shown in Figure 2.10. Some details were missing, however, in the computed flow field. We believe this was due to the coarse mesh of the present numerical simulation.

Velocity profiles for w/V_j and u/V_j at the jet exit on the $y = 0$ plane are shown in Figure 2.15 along with the experimental data given by Reference [3]. The computed velocities agreed reasonably well with the measured data but with a small deviation near the wall of the jet-pipe. In view of the difficulty in measuring



(a). near wall cross-section view of wake vortices in wind tunnel (Fric & Roshko, 1989, $R = 4$, $Re_d = 11400$)



(b). wake vortices observed in water tunnel (Yu, 1987, $R = 6.3$)

Figure 2.13 Wake vortices formation for circular jet.

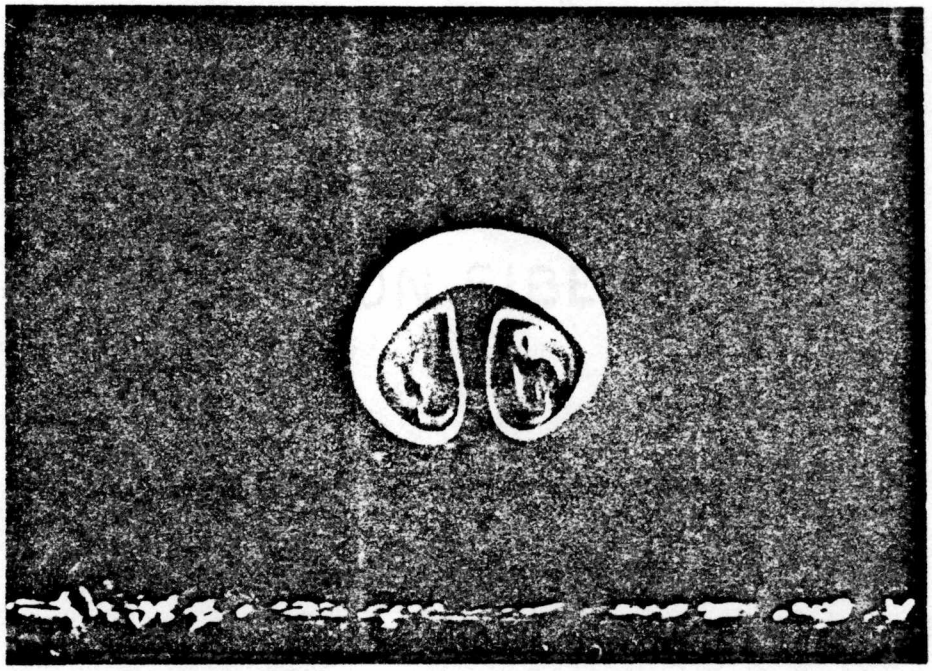
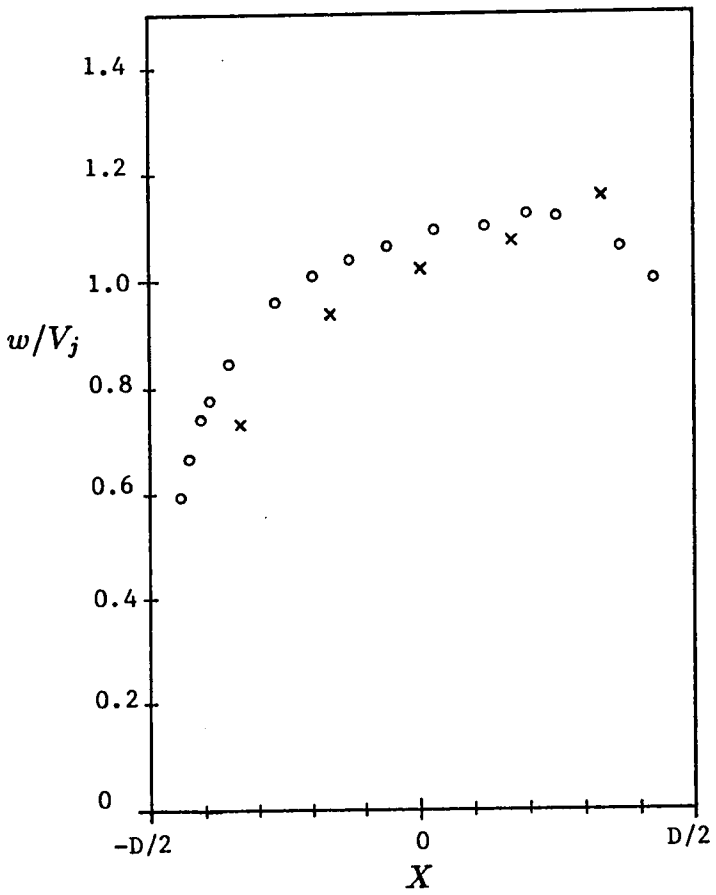
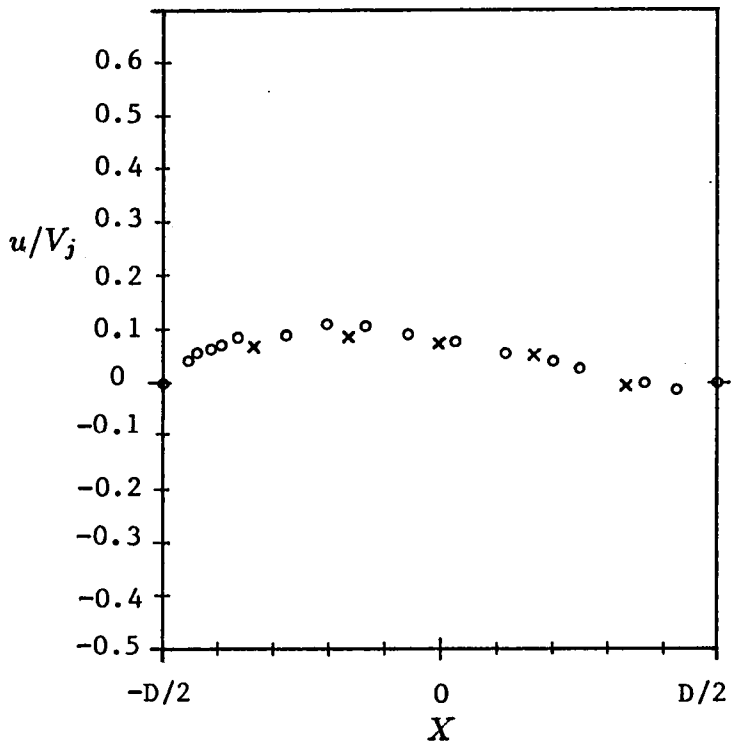


Figure 2.14 Laser induced fluorescence sectional view of a circular jet (Yu, 1987, $R = 3$, $X/D = 3$).



(a). mean w–velocity profile



(b). mean u–velocity profile

× — computed results in present work
o — experimental data by Andreopoulos (1982)

Figure 2.15 The velocity profiles at the circular jet exit (R = 2, t = 3.0).

the velocity profiles within a fine tube, we believe the computation might offer a more correct flow picture in this case. As described before, both the u and w velocity components in the jet-pipe were influenced by the crossflow. From the jet inlet to the exit, the fluid at the front portion of the jet-pipe was decelerated while that at the rear portion of the jet-pipe was accelerated. The computed results also showed that the jet exit velocity profile is nearly symmetric in the y–direction about the $y = 0$ plane.

The information about the location of the deflected centerline of circular jets are available in many early publications. The jet centerline is defined as the locus of maximum velocity points in the $y = 0$ plane. In the present computation, all the computed centerlines of the circular jet compared favorably with the experimental results as shown in Figure 2.16.

A comparison of the computed u–velocity profile in the $y = 0$ plane with the experimental data from Reference [4] is presented in Figure 2.17. In some regions, especially the reverse flow region, the computed results seem to deviate significantly from the experimental data. The error might be caused by the differences in media and flow speeds between these two cases, since the experimental data were measured for a subsonic air flow in a wind tunnel but this is the only quantitative data available for making such a comparison. It should be noticed that the sketched flowfield in Figure 2.10 (p.27), which was an experimental result conducted in a water tunnel, indicates that there is a reverse flow region before $X/D = 3$, and the computed u profile was qualitatively comparable with it. Some error in computation might also be attributed to the lack of the turbulence model. In general, turbulence enhances local flow mixing and therefore shifts the saddle point upstream compared to the laminar case.

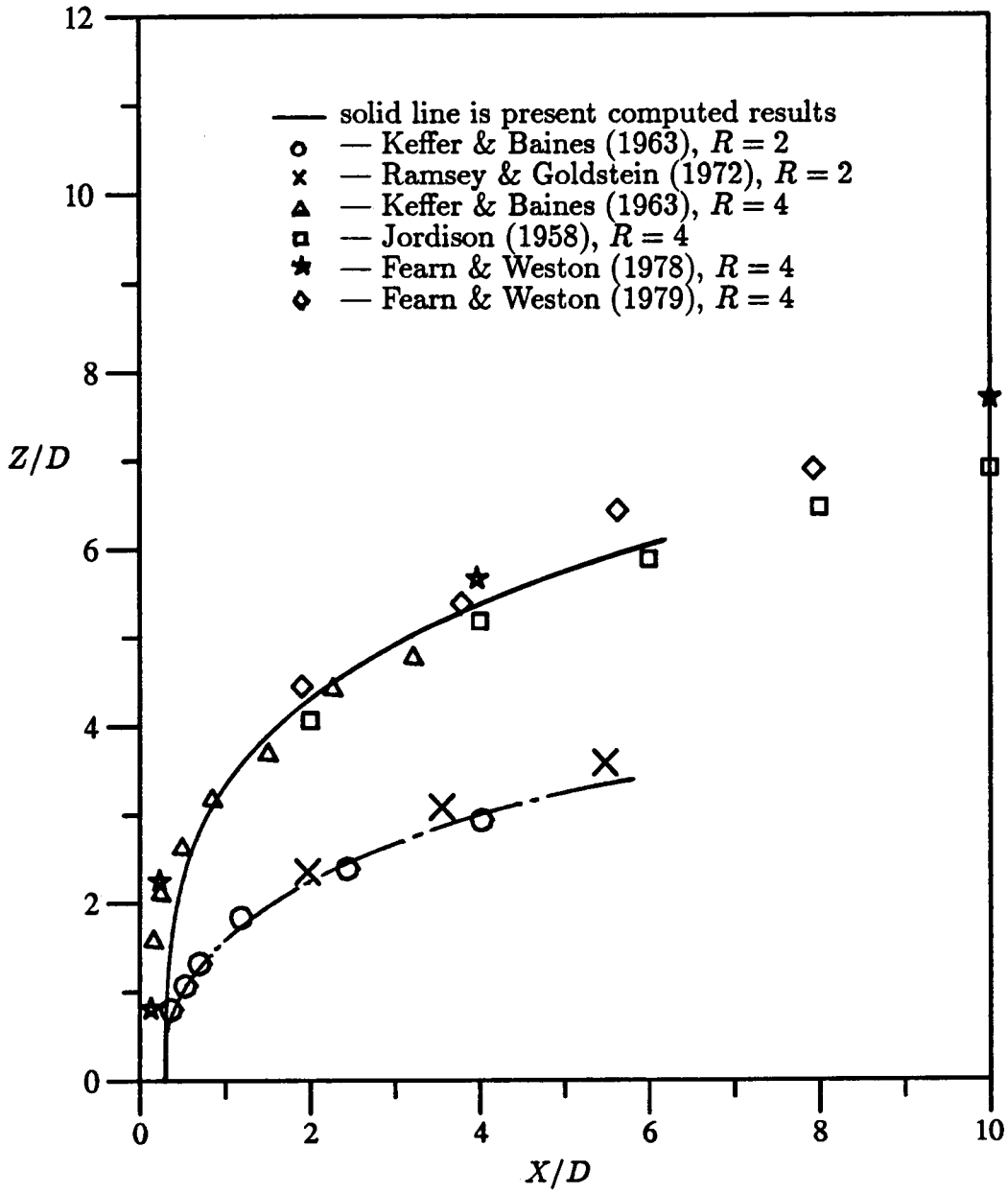


Figure 2.16 A comparison of computed and experimental jet centerlines.

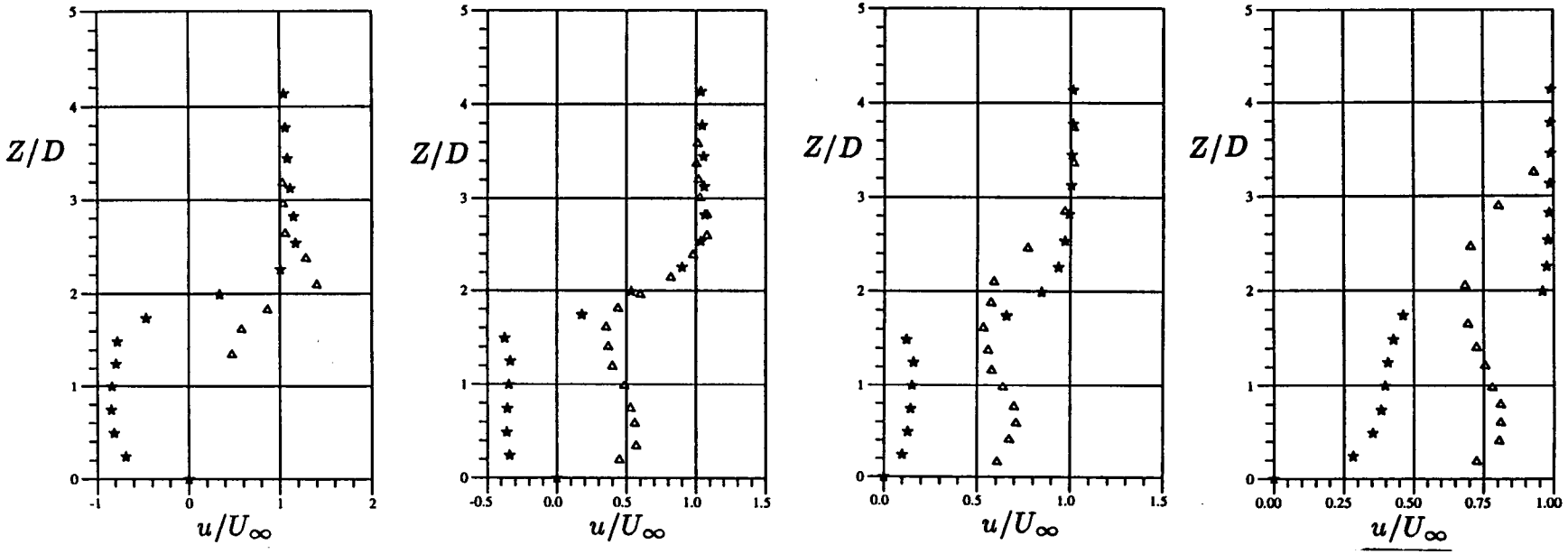
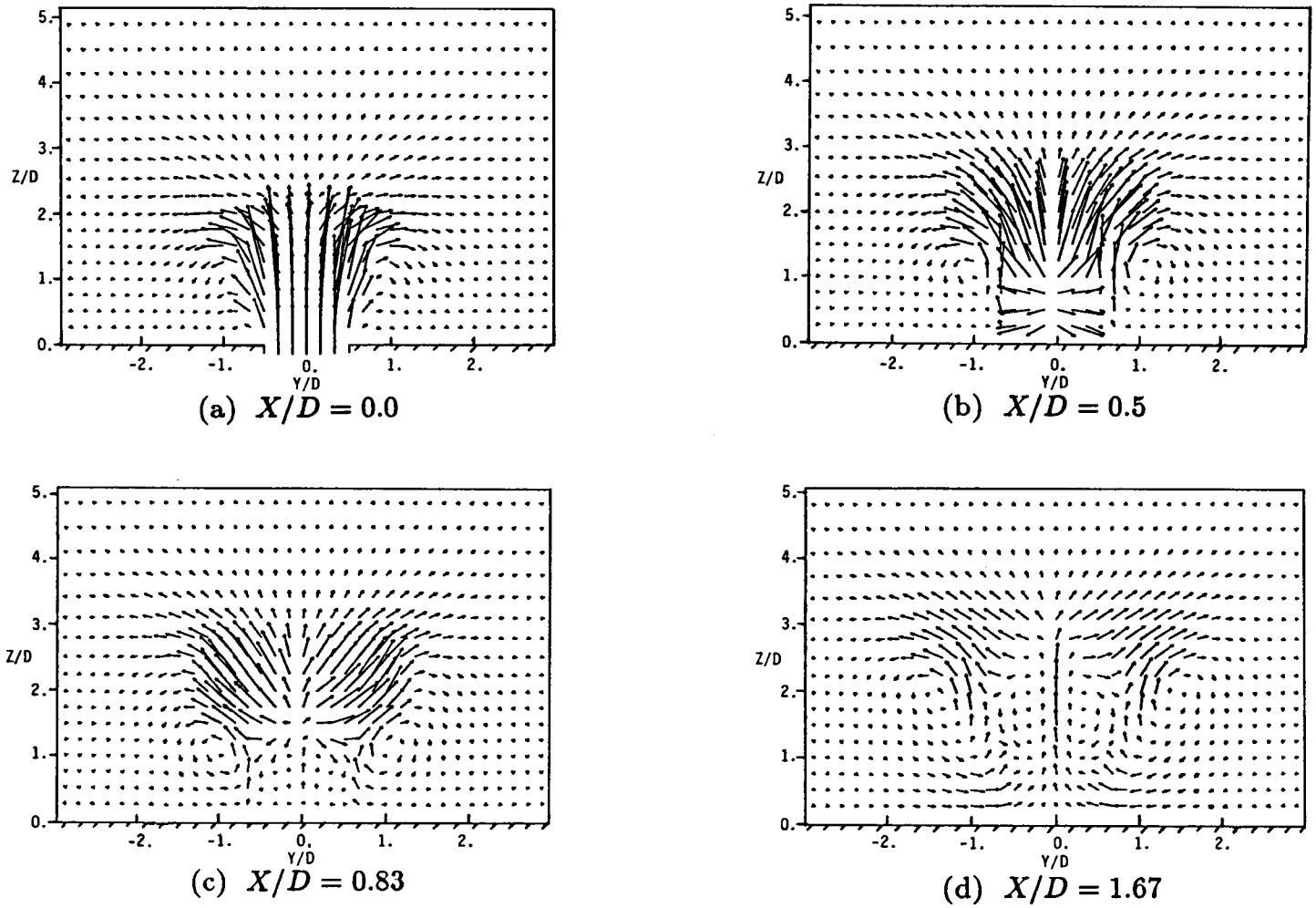


Figure 2.17 The u–velocity profile in the $y = 0$ plane for a circular jet with $R = 2$.

A.2. Circular Jet with Velocity Ratio $R = 4$

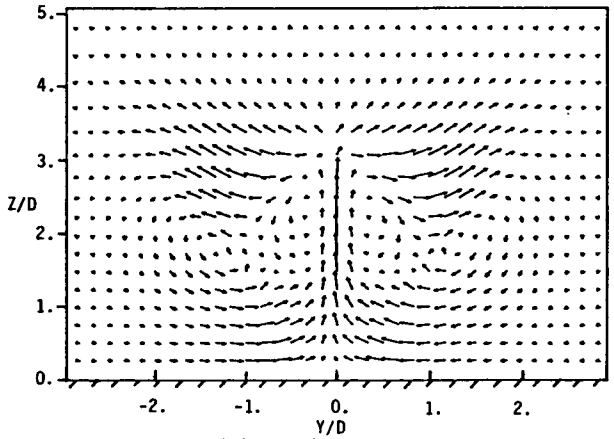
By keeping U_∞ unchanged and doubling the jet velocity, the $R = 4$ case was computed for the circular jet geometry. Some additional interesting vortical phenomena appeared in the computational results in this case. A sequence of sectional views, Figure 2.18, illustrates the development of the counter-rotating vortex pair. The evolution of this vortex pair was more complicated than that in the $R = 2$ case. Its vorticity source was still the jet-pipe boundary-layer vorticity, i.e., the jet's cylindrical vorticity sheet generated inside of the jet-pipe as shown in Figure 1.2 (p.10). Figure 2.18 (a) is a view at the $x = 0$ section which shows large amounts of X^+-directional boundary-layer vorticity, which were from the front portion of the jet's cylindrical vorticity sheet, were brought out to the mainstream by the jet at the Y^- sides of the jet plume while the X^- vorticity was brought out at the Y^+ side of the plume. Immediately downstream of the jet exit, in Figure 2.18 (b), this vorticity formed a counter-rotating vortex pair outboard of the jet plume. The lee-side of the jet's cylindrical vorticity sheet resulted in a second vortex pair inboard of the first pair at a short distance downstream of the jet exit as shown in Figure 2.18 (c). One or two jet diameters downstream from the jet exit, the near wall crossflow moved toward the $y = 0$ plane due to the lower pressure region behind the jet and thus brought more crossflow boundary-layer vorticity into the second vortex pair. While moving further downstream (Figures 2.18 (d) to (h)), the second counter-rotating vortex pair increased its intensity and moved upward. These two pairs of counter-rotating vortices had the same rotation direction and they started to merge together while flowing downstream. Finally the second vortex pair became the dominant one at the far field as shown in Figure 2.18 (h).



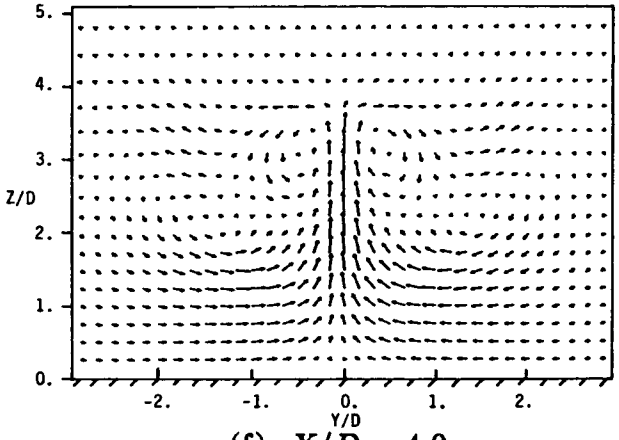
(a) $X/D = 0.0$ (b) $X/D = 0.5$

(c) $X/D = 0.83$ (d) $X/D = 1.67$

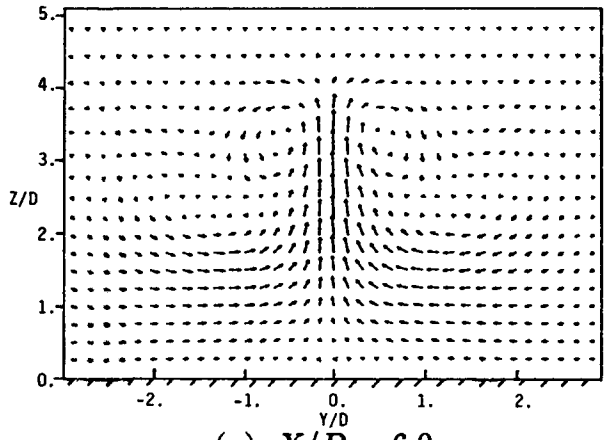
Figure 2.18 The counter-rotating vortex pairs for circular jet with $R = 4$.



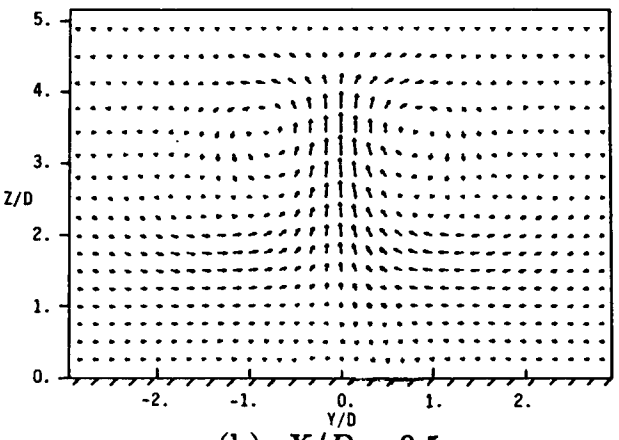
(e) $X/D = 2.17$



(f) $X/D = 4.0$



(g) $X/D = 6.0$



(h) $X/D = 9.5$

Figure 2.18 (continued).

Another noticeable phenomenon was the jet's front-bound vortices which were generated on the intersection of the jet with the main-flow. Figure 2.19 is a photograph of these periodic vortices from Reference [22] and Figure 2.20 illustrates

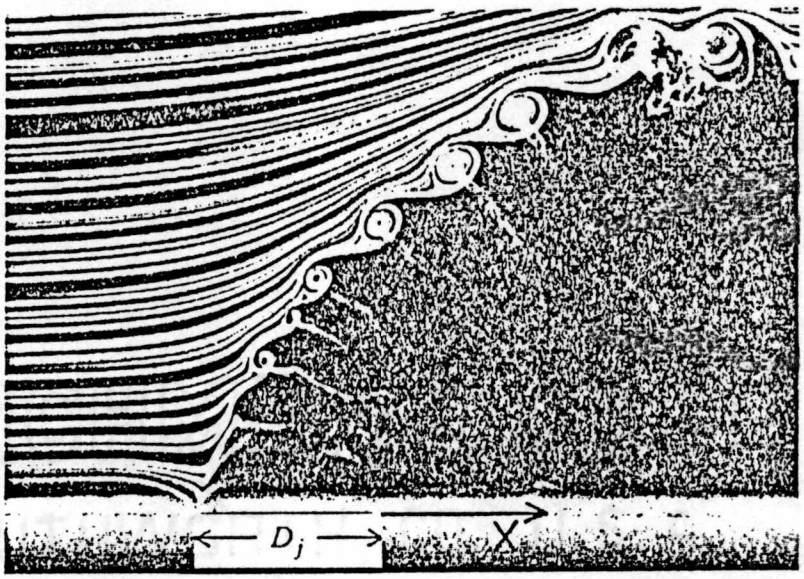
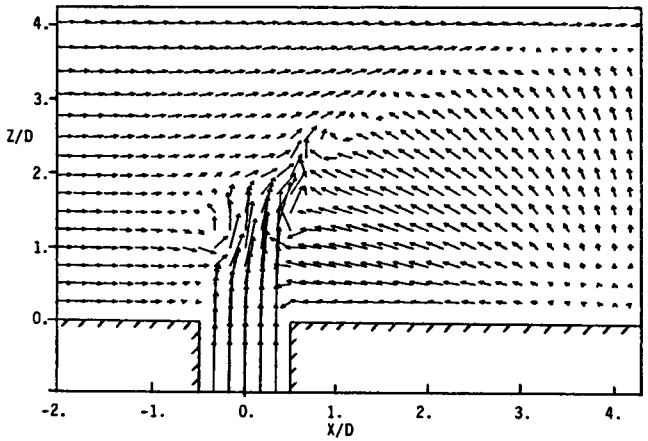
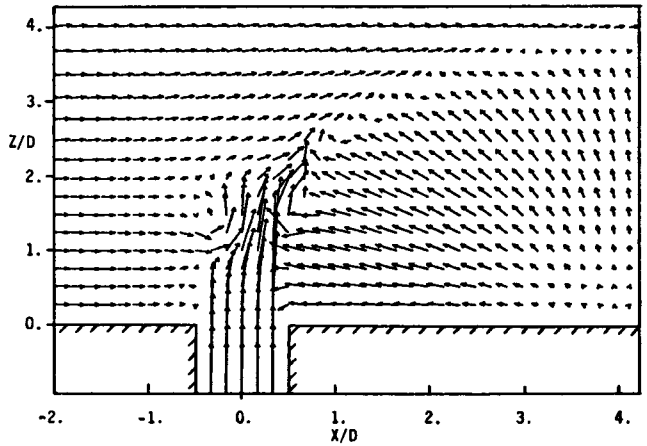


Figure 2.19 The front-bound vortices observed during wind tunnel test (Fric & Roshko, 1989, circular jet, $R = 2$, Re_d=3800).

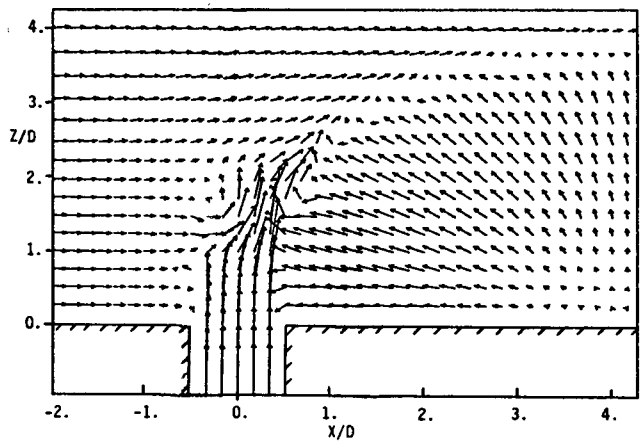
this phenomenon from a sequence of computed results. By observing these results, it was possible to establish the "periodicity" of the flow which repeated itself during each time period. Starting from an arbitrary time, say at t=3.0 in Figure 2.20 (a); a developed front-bound vortex was shown at $x = 1.0$; this vortex was continuously moving upward in Figure 2.20 (b) and (c) as time increased. In Figure 2.20 (d), it was noticed that a new vortex started to form underneath the jet plume while the first vortex kept moving upward. The newly formed vortex grew up in Figure 2.20 (e) and (f), while the intensity of the first vortex was gradually reduced. Finally, in Figure 2.20 (g), the flow "returned" to its original pattern as has been



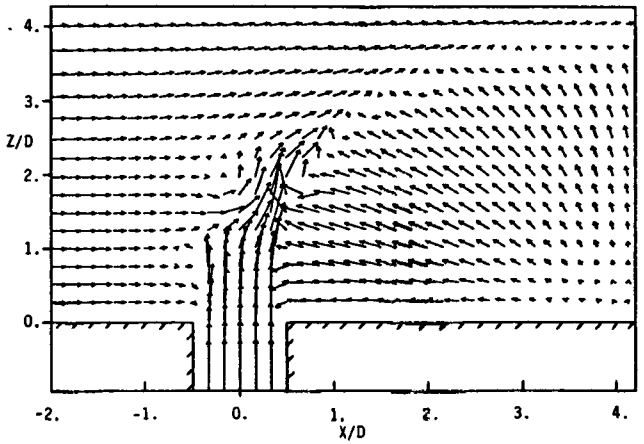
(a) $t = 3.0$



(b) $t = 3.04$

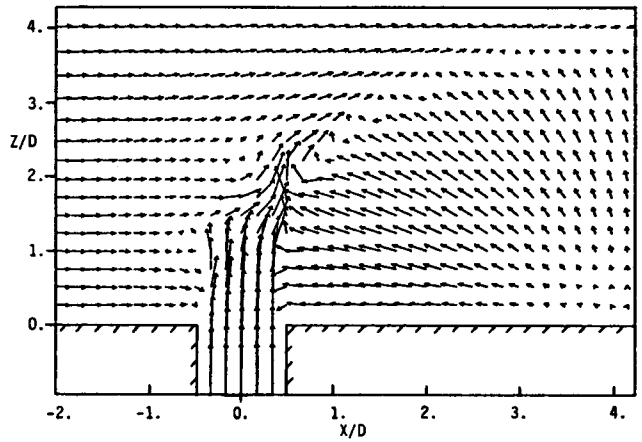


(c) $t = 3.08$

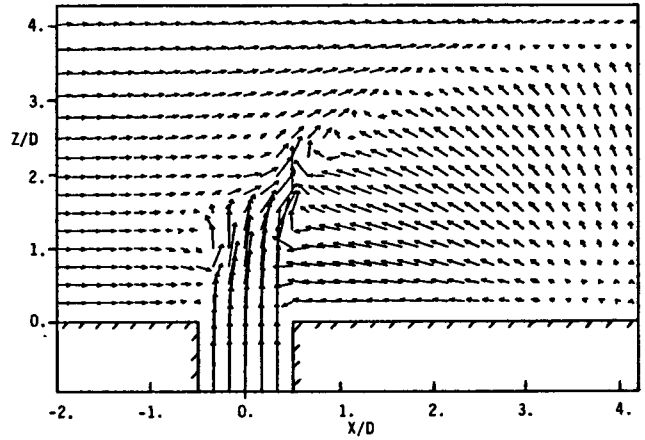


(d) $t = 3.12$

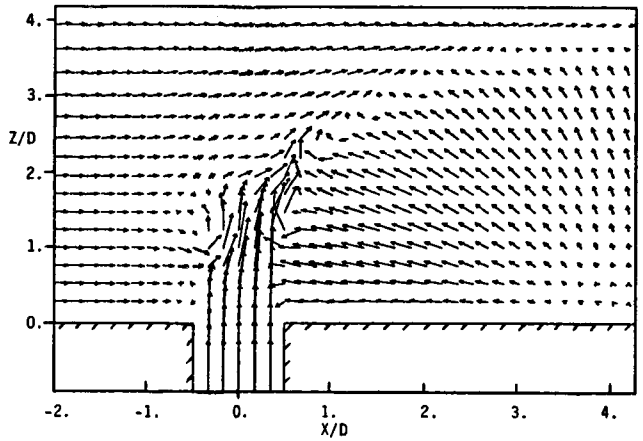
Figure 2.20 Computed jet's front-bound vortices (circular jet, $R = 4$).



(e) $t = 3.16$



(f) $t = 3.20$



(g) $t = 3.24$

Figure 2.20 (continued).

shown in Figure 2.20 (a) and started its cycle again. The time for this period was $t = 0.24$ of computational time and the corresponding Strouhal number, which is defined as

$$S_t = \frac{fD}{U_\infty},$$

was $S_t = 0.25$. It should be noted that the computational time and the physical time may not exactly coincide. The source of the jet's front-bound vortices was also the boundary layer vorticity generated inside of the jet-pipe; the shear layer on the front portion of the jet rolls up immediately after leaving the jet exit and forms the periodic vortices.

Along the lee-side boundary of the jet plume, the downward velocity vectors indicate that there is a series of rear-bound vortices as sketched in Figure 2.10 (a) (along line C). Similar to the front-bound vortices, the rear portion of the original jet's cylindrical sheet vorticity was the source for these rear-bound vortices. A periodic flow pattern, which had the same periodic frequency as the front-bound vortices, was also noticed at the middle to upper potion of the jet's rear-boundary; a kink was initiated at $x = 1.0$ and then moved upward. For a better picture of the flowfield in this region a denser mesh has to be employed in that region.

The small separation zone in front of the jet plume was larger in this case than in the $R = 2$ case, but still much smaller than that found for the $\beta = 90^o$ slot-jet case as will be discussed later. It should be mentioned that this separation region changed its shape periodically with the same frequency as the jet's front-bound vortices.

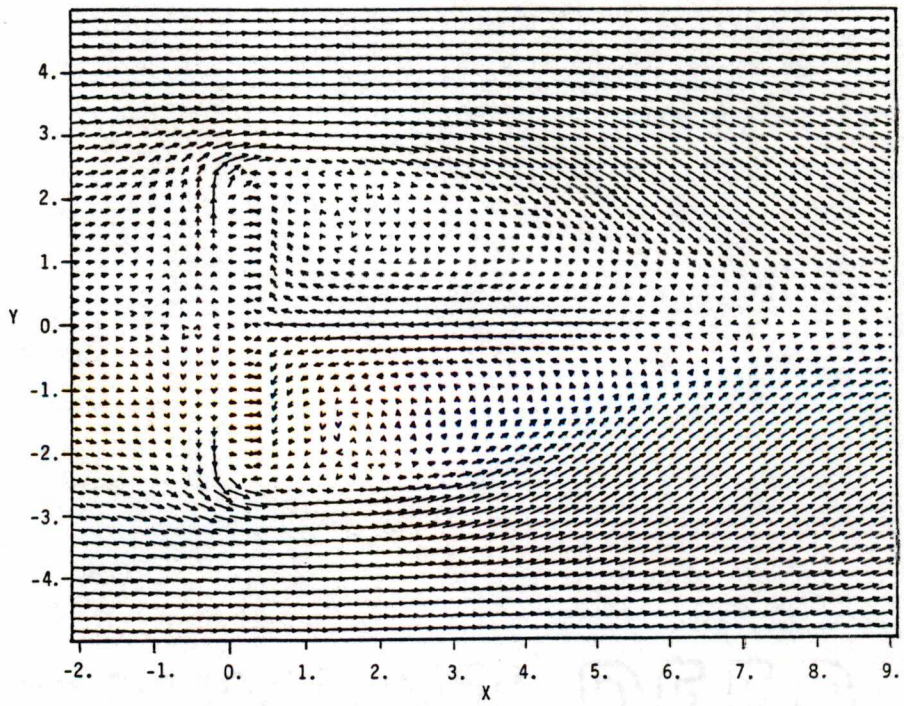
Although it has been observed in many experiments [22, 68, 72], no periodic vertical wake vortex formation was detected for the circular jet cases in this computation. It is believed that the computation time was not sufficient long to carry out this kind of motion for these cases.

B. Large Aspect Ratio Rectangular Jet with 90° Yaw Angle

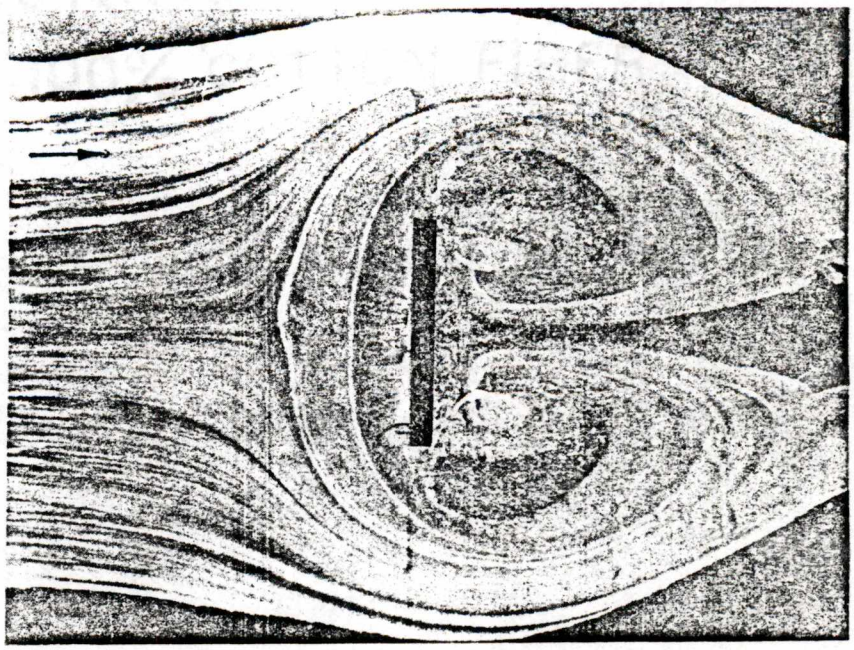
The solution for a rectangular jet with a large aspect ratio were computed for a yaw angle of $\beta = 90^o$ and with the long axis of the jet-port perpendicular to the main stream. The jet had a non-dimensional width of 0.6 and an aspect ratio of approximately 8 which was in the middle range of the aspect ratio of 6 to 10 used in the experimental investigation conducted by Krothapalli et al. (1989). The computational domain was 5/4 wider than that for other cases because the larger length of the jet. For a better comparison with experiments, velocity ratios of $R = 3$ and 10 were used in this computation.

Figure 2.21 (a) is a sectional velocity vector plot at a plane very near the base wall ($z = 0.3$) for the $R = 3$ case. It is very comparable with the surface streak pattern shown in Figure 2.21 (b) which was from Reference [33]. A pair of tornado-like vortices is clearly shown behind the jet orifice in both figures. The size of these vortices are considerably larger than those for other jet geometries investigated in this study because the jet's length here was much larger. This resulted in a larger blockage to the main flow and consequently a larger wake flow.

The separation lines in Figure 2.21 indicated a "horseshoe" type vortex system and this separation zone is shown more clearly in Figure 2.22. Although two vortices are shown in front of the jet in Figure 2.22 (b) -a photograph from Reference [33]- the authors stated that most of their frames show the existence of only a single large vortex with varying location. In the present computed result, only one vortex was formed in front of the jet-orifice as shown in Figure 2.22 (a). The sectional views from the computed results show that in the y–direction, this vortex extended to the two side-edges of the jet-orifice but gradually reduced in size.

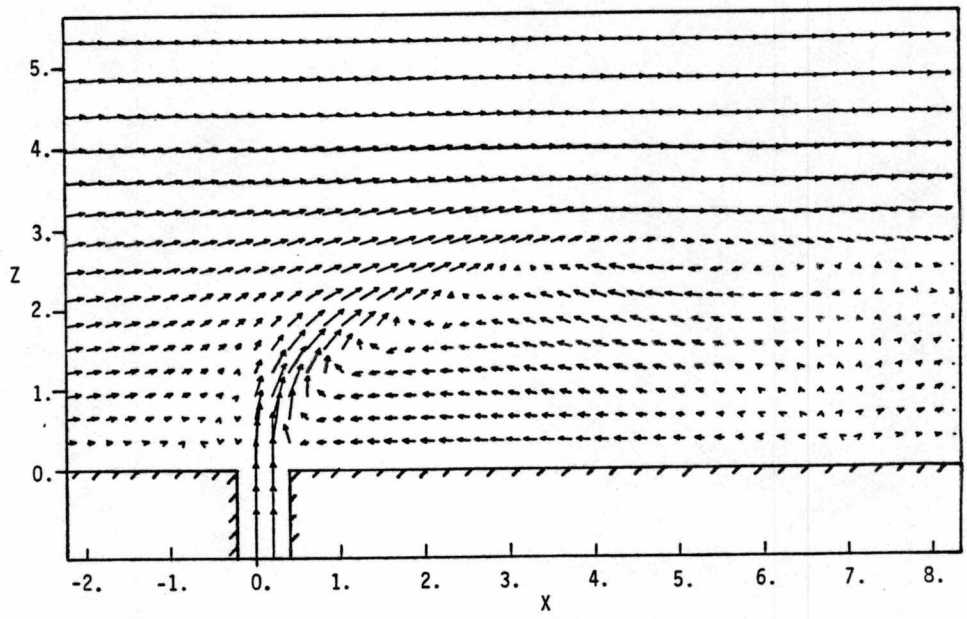


(a) computed velocity vector plot at $Z = 0.3$ plane ($t = 2.5$)

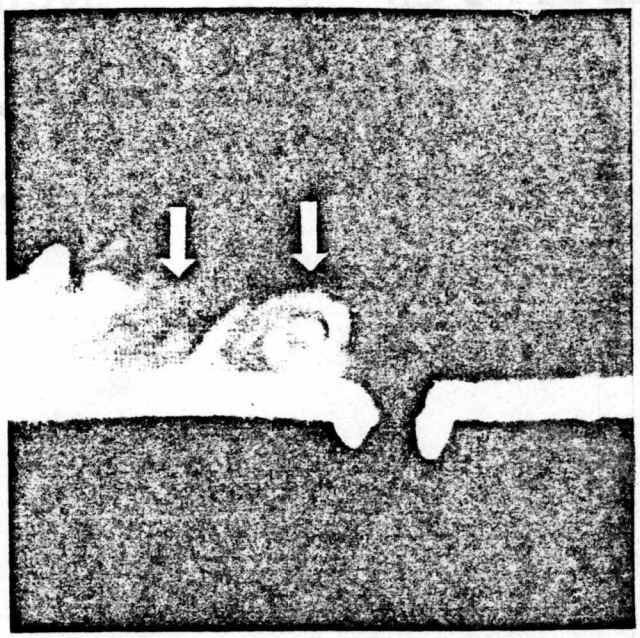


(b) surface streaking pattern on bottom wall (Krothapalli et al., 1989)

Figure 2.21 Horizontal sectional view for $\beta = 90^{\circ}$ slot-jet ($R = 3$).



(a) computed velocity vector plot ($R = 3$, $t = 2.5$)



(b) instantaneous laser sheet picture (Krothapalli et al. , 1989, $R = 2.5$, the arrows indicate the "horseshoe" vortices)

Figure 2.22 Vertical sectional view at the $y = 0$ plane for $\beta = 90^o$ slot-jet.

More information was revealed by the computational results. Figure 2.23 contains a series of cross-section views of the jet wake at different x–stations (viewed from the downstream direction). Again, the counter-rotating vortex pair, which is the dominant feature of the jet plume, evolved from two vortex pairs as in the $R = 4$ circular jet case. The second counter-rotating pair, however, appeared much further downstream than that in the circular jet case. In the circular jet case, this pair has been clearly observed at the $x = 2.8$ station, but not until about the $x = 4$ station for the long-slot jet case.

According to Krothapalli et al., there are two different types of flow structure in the wake region; the near wake structure shows a symmetric pair of wake vortices for jet-to crossflow velocity ratio $R = 1$ to about 5; when R is increased beyond 5, a periodic wake vortex formation will occur. For this reason, a computation for $R = 10$ was carried out to examine this interesting phenomenon. The vortical flow appeared very strong in this case as shown in Figure 2.24. But no periodic wake vortex motion had appeared up time $t = 2.0$.

C. Slot Jet with 45° Yaw Angle

The solution for a rectangular jet placed at a yaw angle of $\beta = 45^o$ relative to the free stream was computed. The jet orifice for this configuration was also approximated by a set of square grids as shown in Figure 2.25. The jet had a non-dimensional width of 0.566 and an aspect ratio approximately of 3.75, which was close to the aspect ratio of Model 2 in Wu, Vakili, and Yu's experiments [68, 72]. For a better comparison with the circular jet case, the jet port's cross-section area was kept approximately equal to unity and the jet-to-crossflow velocity ratios $R = 2$ and 4 were used for this configuration.

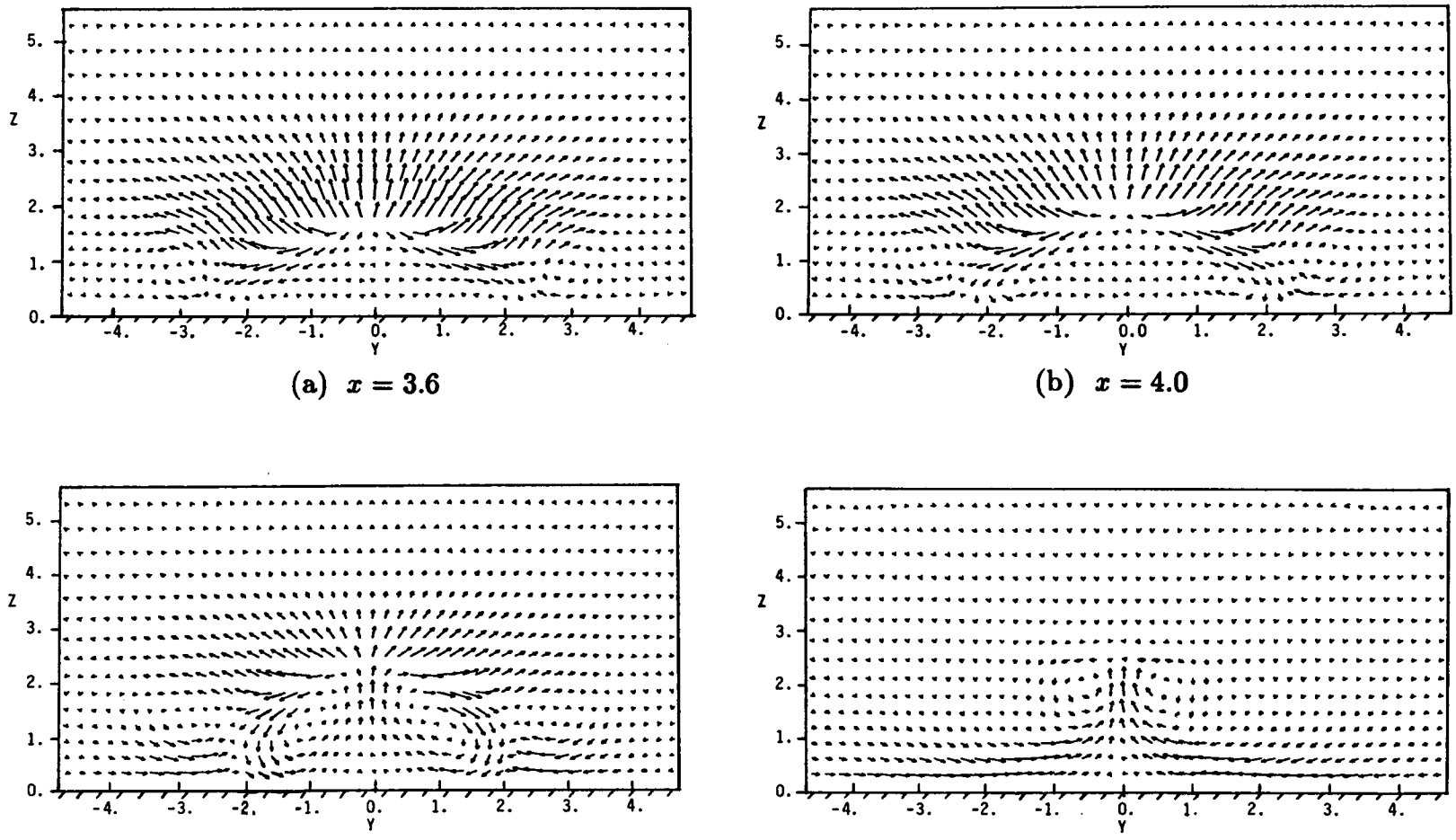
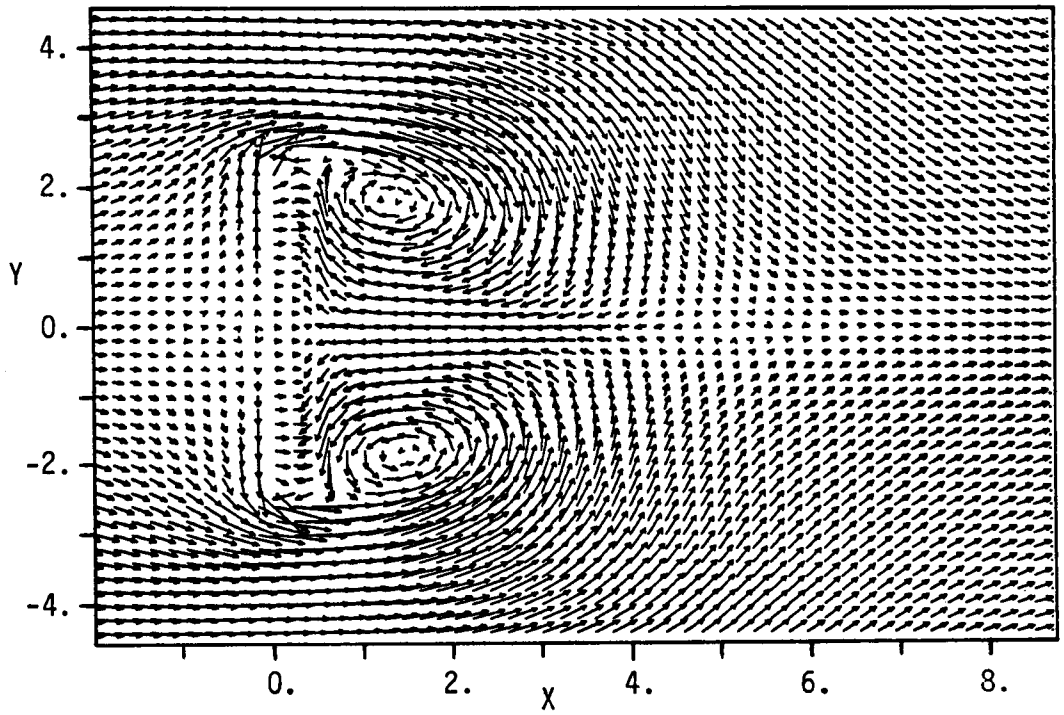
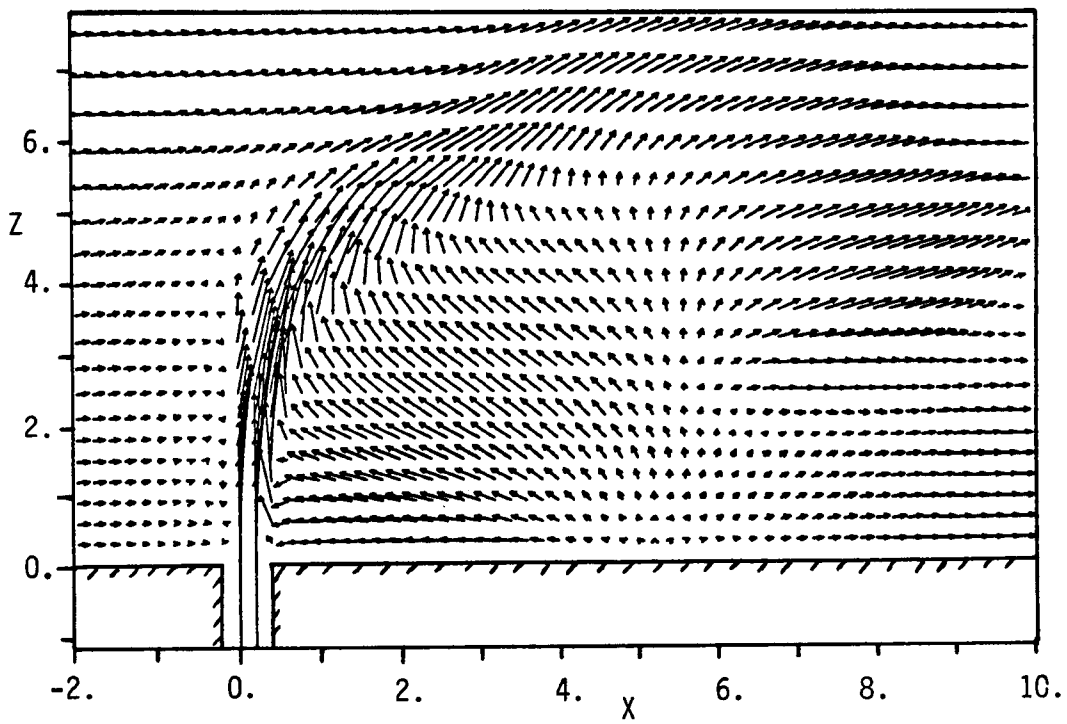


Figure 2.23 The development of the counter-rotating vortex pair for $\beta = 90^o$ long-slot jet (cross-sectional views, $R = 3$, $t = 2.5$).

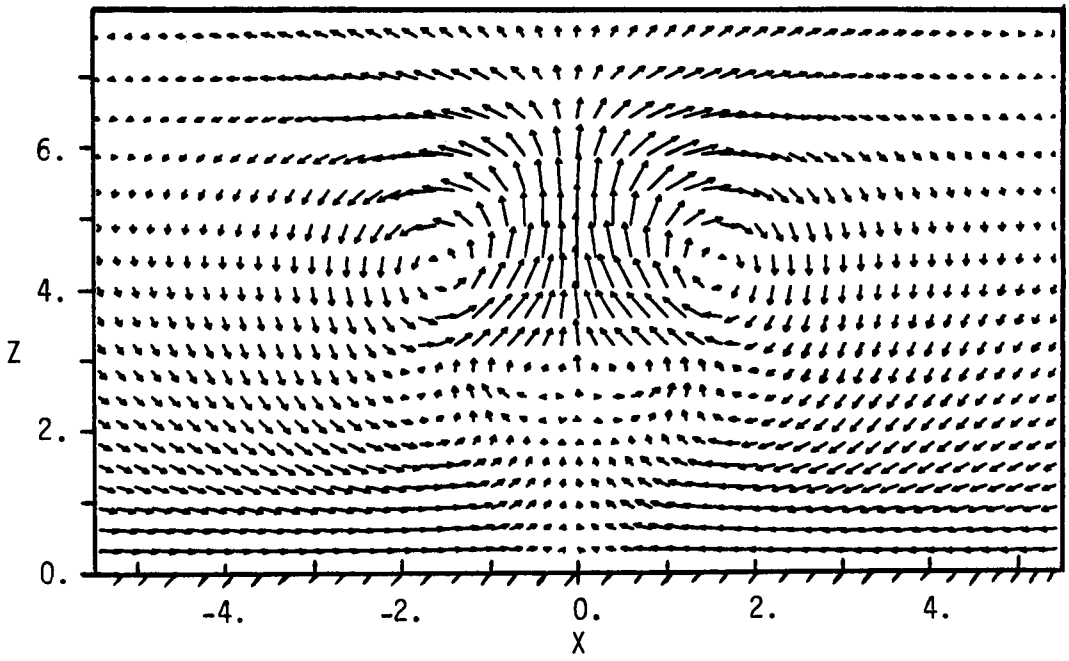


(a) horizontal sectional view at $z = 0.3$ plane



(b) vertical sectional view at $y = 0$ plane

Figure 2.24 Sectional velocity vector plots for $R = 10$ long-slot jet ($\beta = 90°$, t=2.0).



(c) cross-sectional view at $x = 9.0$ plane

Figure 2.24 (continued).

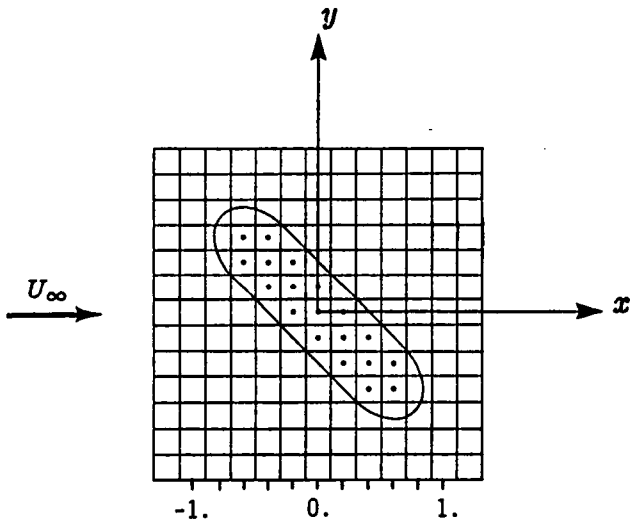
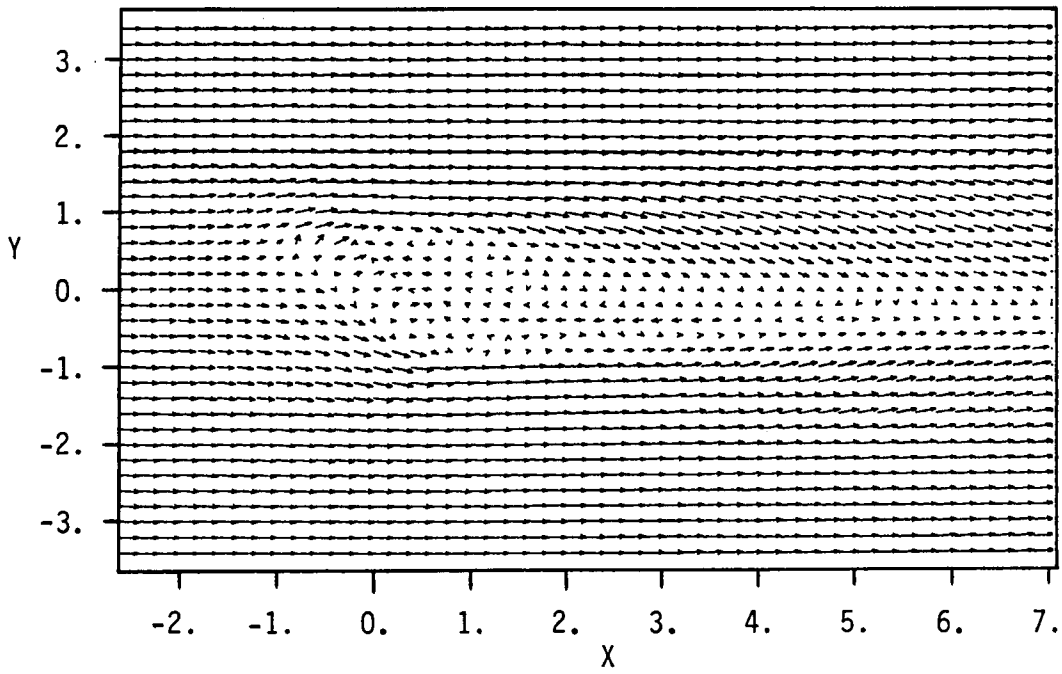


Figure 2.25 Grid structure used to approximate the $\beta = 45°$ asymmetric jet orifice.

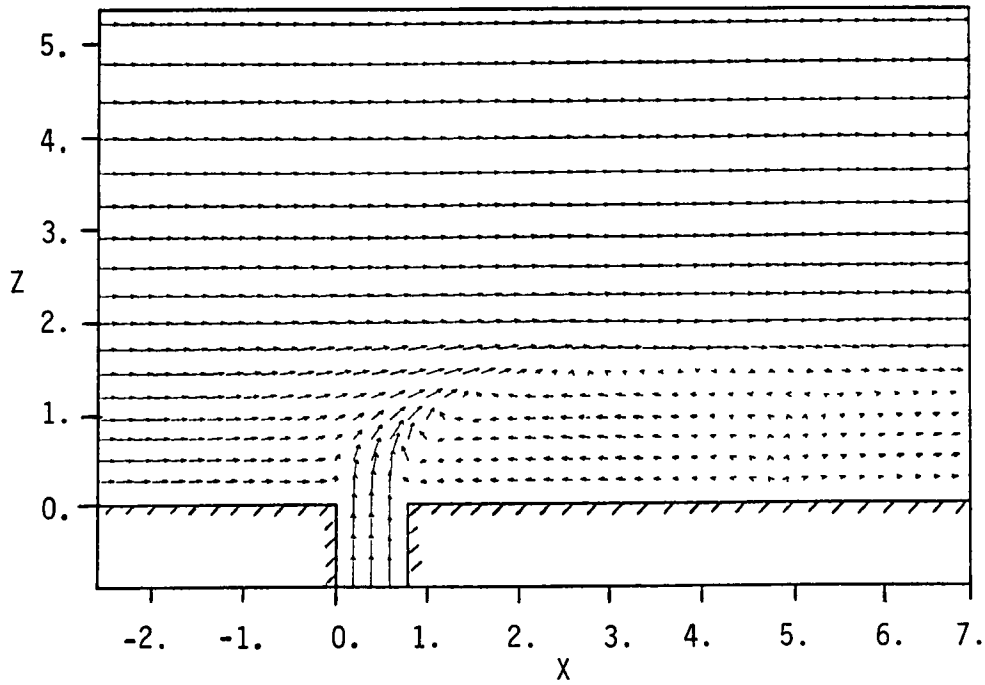
Figure 2.26 contains three typical sectional views of the flowfield for the 45° asymmetric jet with $R = 2$. Some basic features of the symmetric jet in a crossflow still remained but several major changes in the flowfield were also noticed. In the horizontal plane, Figure 2.26 (a), the wake vortices now formed asymmetrically behind the jet plume. The larger vortex was behind the front corner, the Y^+ side of the jet, while the smaller one formed behind the rear corner. The size of the wake vortices was reduced compared to that in the symmetric cases and the fluid spiraled out from the bottom wall right behind the jet corners just like as was observed in our water tunnel testing [68, 72]. The saddle point corresponding to these two vortices was no longer on the $y = 0$ plane but moved toward the Y^- direction. It was also noticed that the stagnation point in front of the jet moved towards the Y^+ direction as observed in the experiments. Figure 2.26 (b) is a view which was cut through the saddle point and shows the center plane of the reverse flow.

In Figure 2.26 (c), the original symmetric counter-rotating vortex pair now became very asymmetric. The vortex corresponding to the front corner of the jet was much stronger then the one corresponding to the rear corner. This was due to the fact that the lee-side edge of the jet was inclined toward the Y^+ side and thus the shear layer corresponding to that side provided more X^+–directional vorticity than the X^-–directional vorticity produced on the Y^- side. Figure 2.27 contains a set of cross-section views (viewed from downstream), and illustrates the early development of the counter-rotating vortex pair. It is clear from these plots that even when the jet plume was just out of the jet-pipe, the flow already had a much stronger rotational tendency on the Y^+ side than on the Y^- side.

The computational results for the $R = 4$ jet showed similar behavior to that for the $R = 2$ jet but with a larger jet/free-stream flow interaction. Figure 2.28

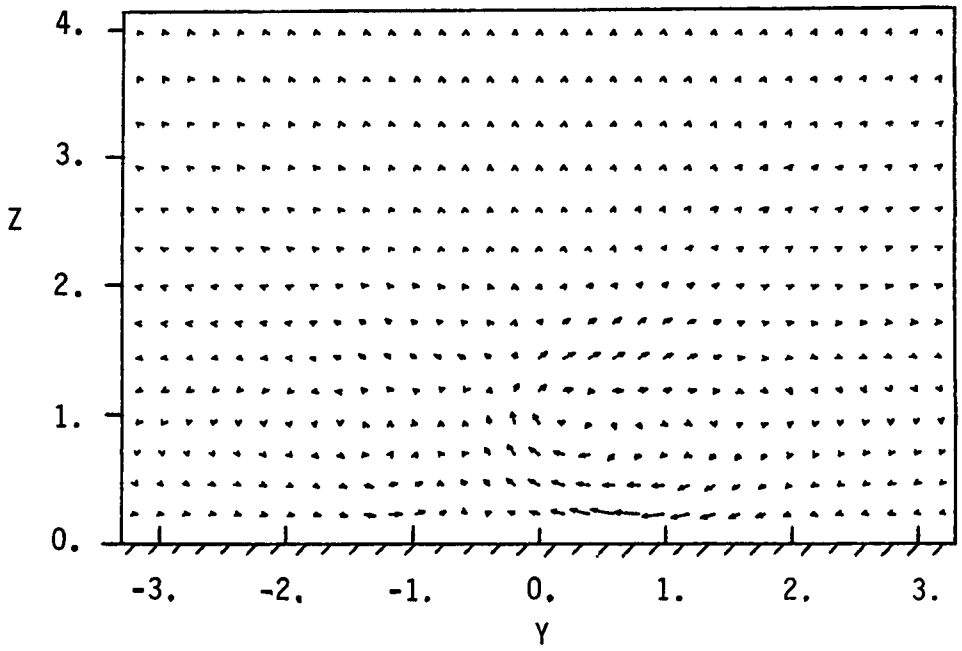


(a). horizontal plane (Z = 0.2)



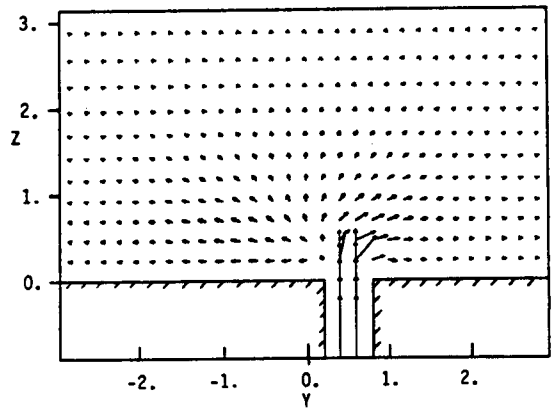
(b). vertical plane (Y = -0.4)

Figure 2.26 The sectional velocity vector plots for 45° asymmetric jet (R = 2, t=3.0).

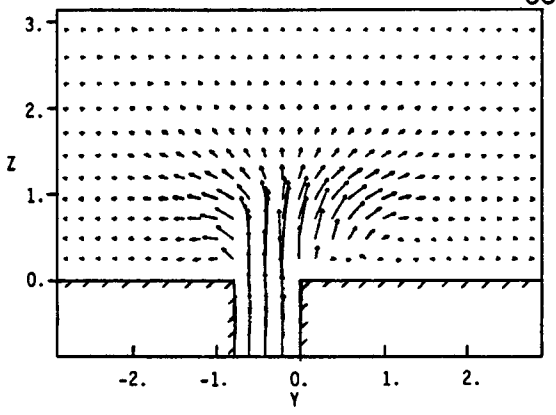


(c). cross-section plane (X = 3.)

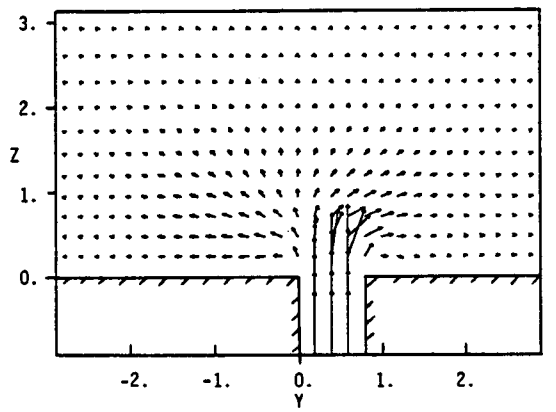
Figure 2.26 (continued).



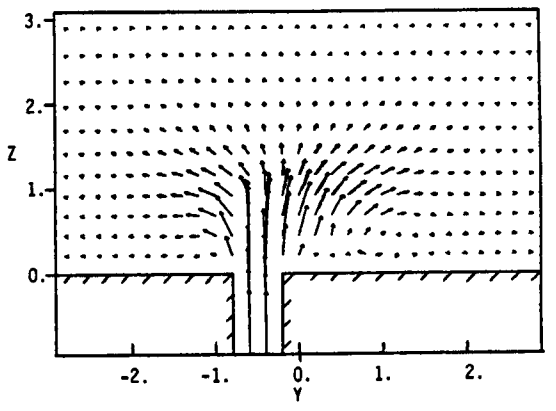
(a) $x = -0.6$



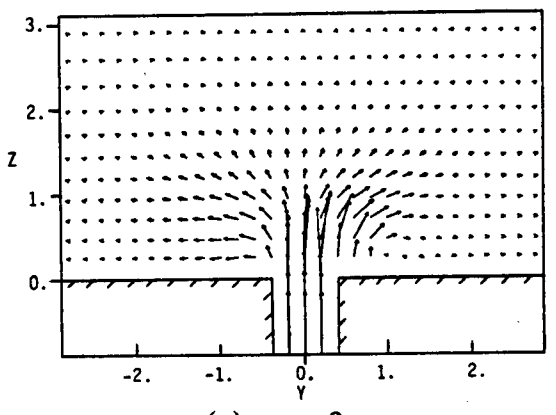
(d) $x = 0.4$



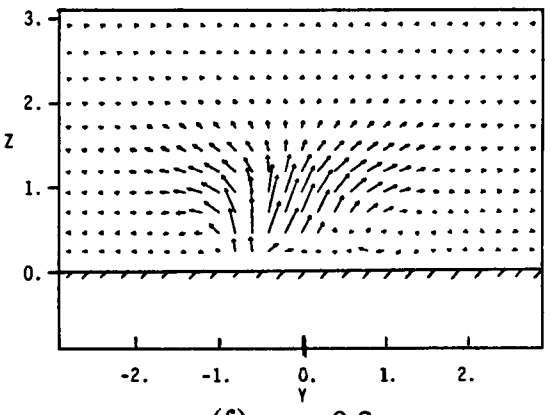
(b) $x = -0.4$



(e) $x = 0.6$



(c) $x = 0.$



(f) $x = 0.8$

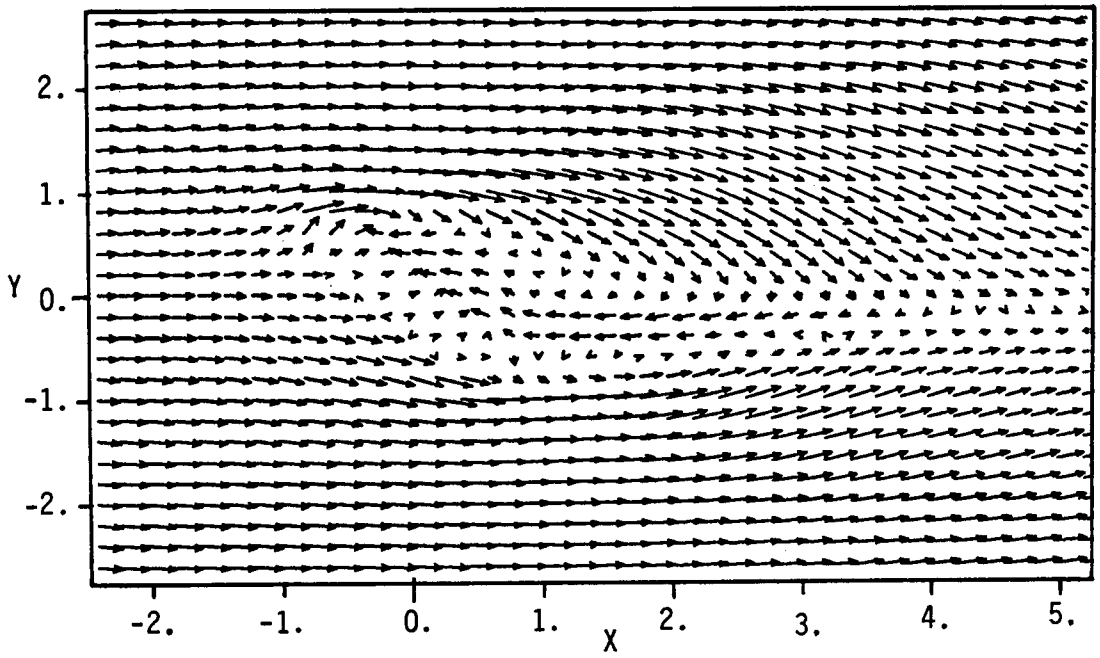
Figure 2.27 The development of the counter-rotating vortex pair along jet exit at various x–stations ($\beta = 45°$, $R = 2$, $t = 3.0$, x–locations refer to Figure 2.25).

shows some sectional velocity vector plots for the $R = 4$ case. In the vertical view, the front-bound vortex phenomenon was repeated here but was weaker than that for the $R = 4$ circular jet case. In cross-sectional view, the skewed counter-rotating vortex pair is shown with the one corresponding to the jet front corner being stronger but slightly lower in the z–direction.

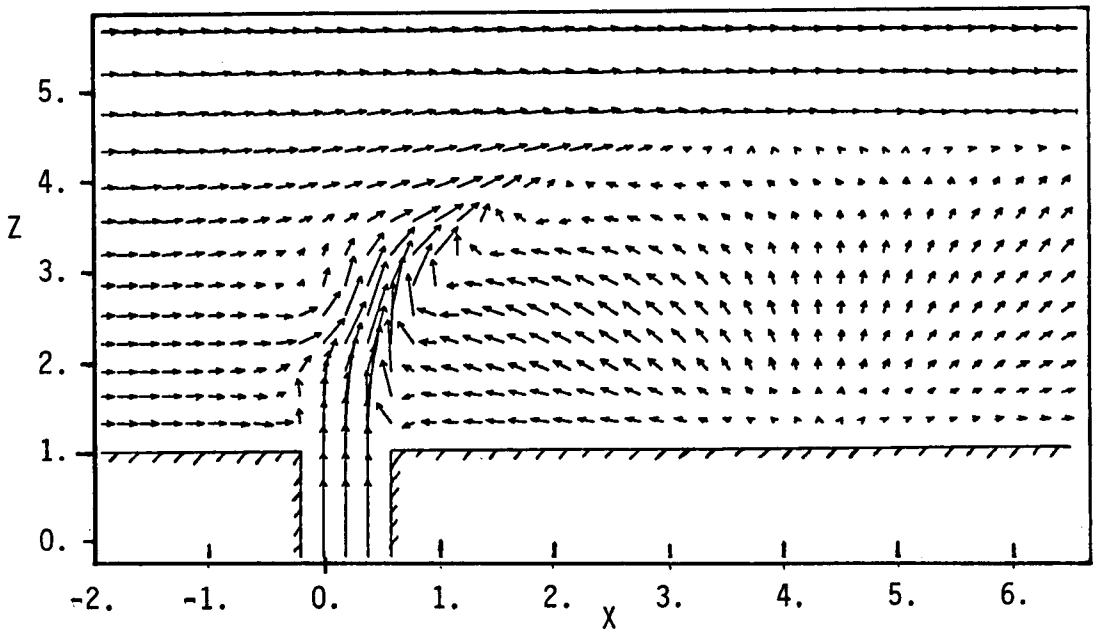
D. Slot Jet with 30° Yaw Angle

The solution for a rectangular jet placed at a yaw angle of $\beta = 30^o$ relative to the free stream was computed. The jet orifice for this configuration was represented by a set of rectangular grids as shown in Figure 2.29. The jet had a non-dimensional width of 0.69 and an aspect ratio of approximately 4.6, Again, for comparison with other cases, jet-to-crossflow velocity ratios of $R = 2$ and 4 were used for this configuration.

In general, the flowfield of the 30° asymmetric jet in crossflow was very similar to that of the 45° asymmetric jet with most of its basic features remaining. Figure 2.30 shows sectional velocity vector plots of the flowfield of the 30° asymmetric jet in crossflow and some changes of the flowfield were noticed. In the horizontal plane, Figure 2.30 (a), the reverse flow region behind the jet was much smaller than that in the $\beta = 45^o$ case. The vertical wake vortex pair was even more skew than before, i.e., the vortex behind the front corner of the jet grew relatively larger while the one behind the rear corner of the jet became smaller. Figure 2.30 (b) is a vertical-plane view which shows the center plane of the reverse flow. Unlike that in the $\beta = 45^o$ asymmetric jet case, the vortices along the front boundary of the jet did not appear clearly here and so the front-boundary was relatively smooth. We believe that this is because the jet blockage area was smaller than before and

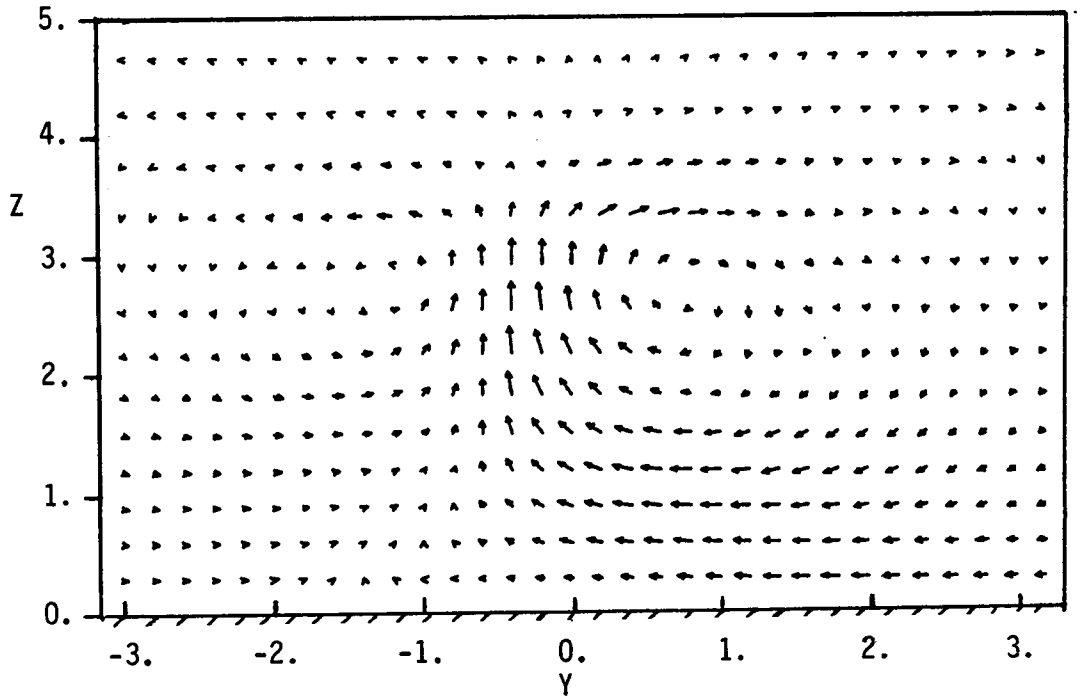


(a) horizontal plane (Z = 0.2)



(b) vertical plane (Y = -0.2)

Figure 2.28 The sectional velocity vectors for 45° asymmetric jet ($R = 4$, t=2.1).



(c) cross-section plane (X = 11.0)

Figure 2.28 (continued).

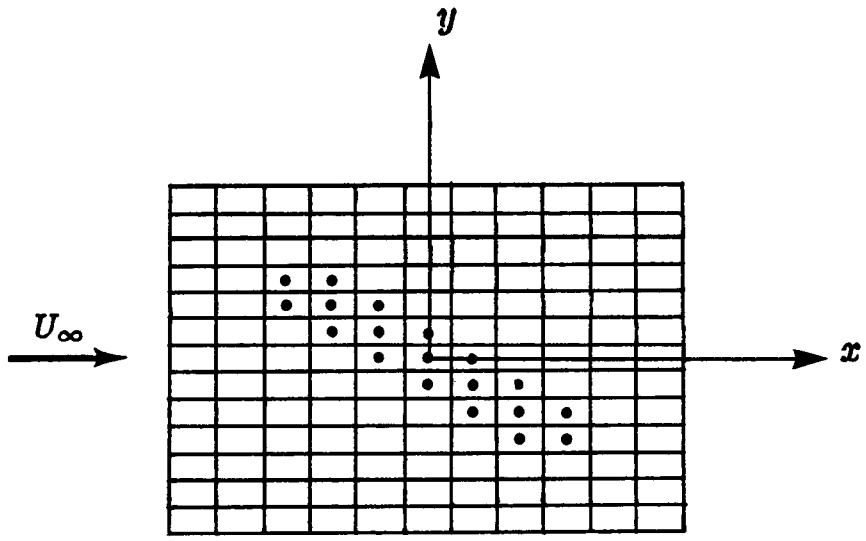
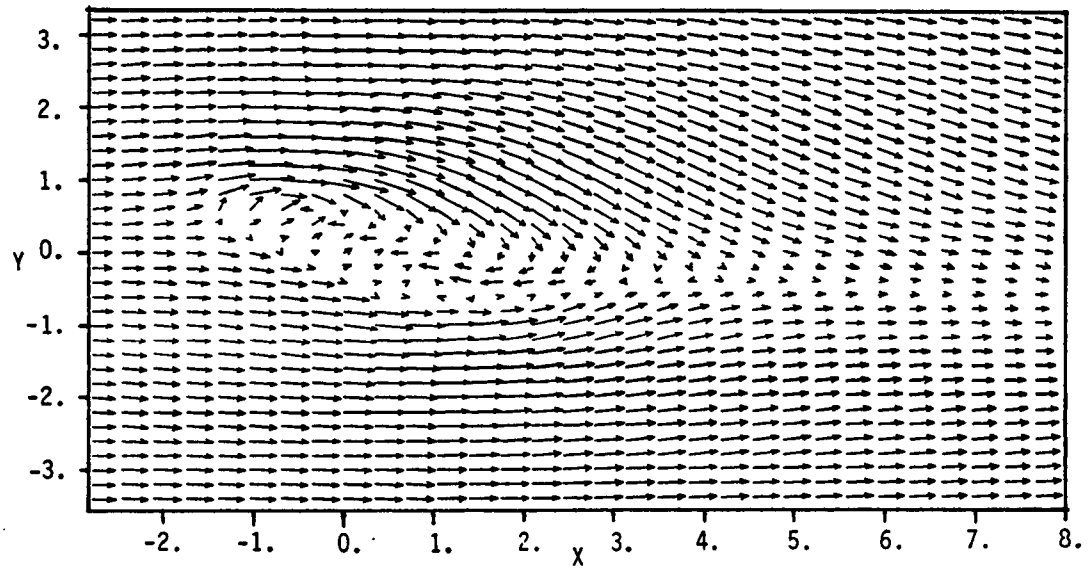
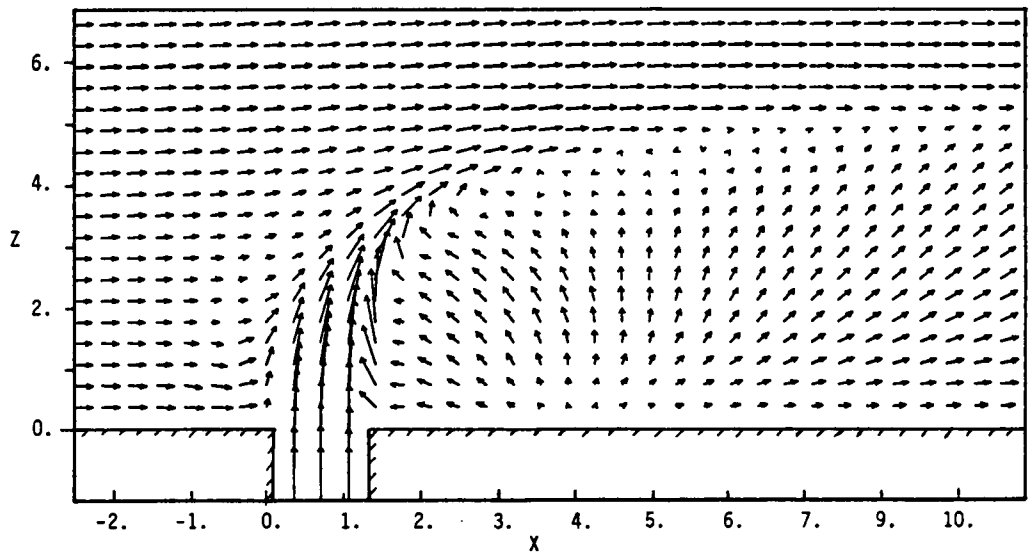


Figure 2.29 Grid structure used to approximate the $\beta = 30°$ asymmetric jet orifice.

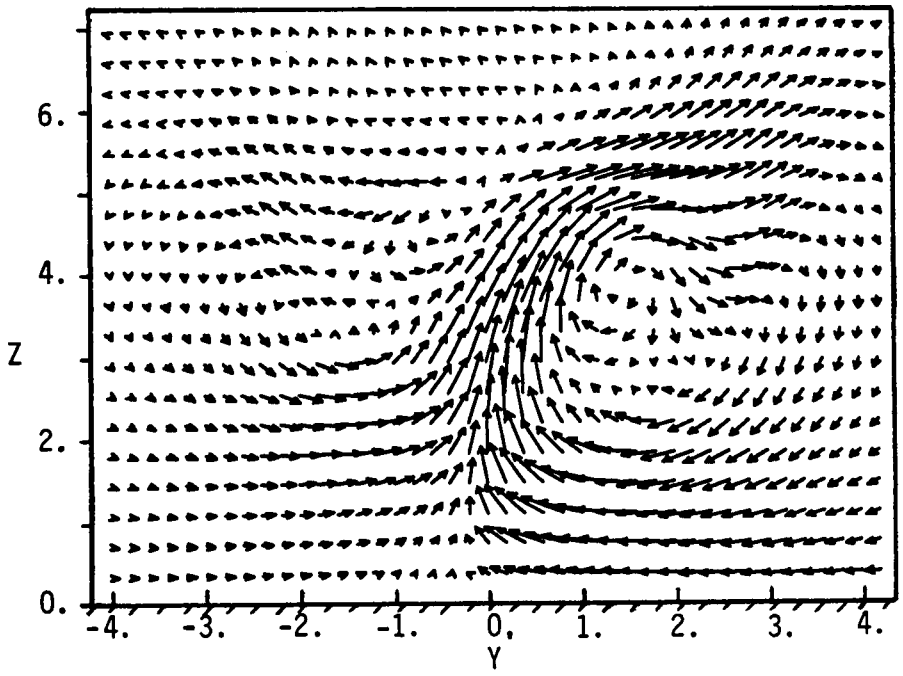


(a) horizontal plane (Z = 0.2)



(b) vertical plane (Y = -0.4)

Figure 2.30 Sectional velocity vectors for 30° asymmetric jet in a crossflow.



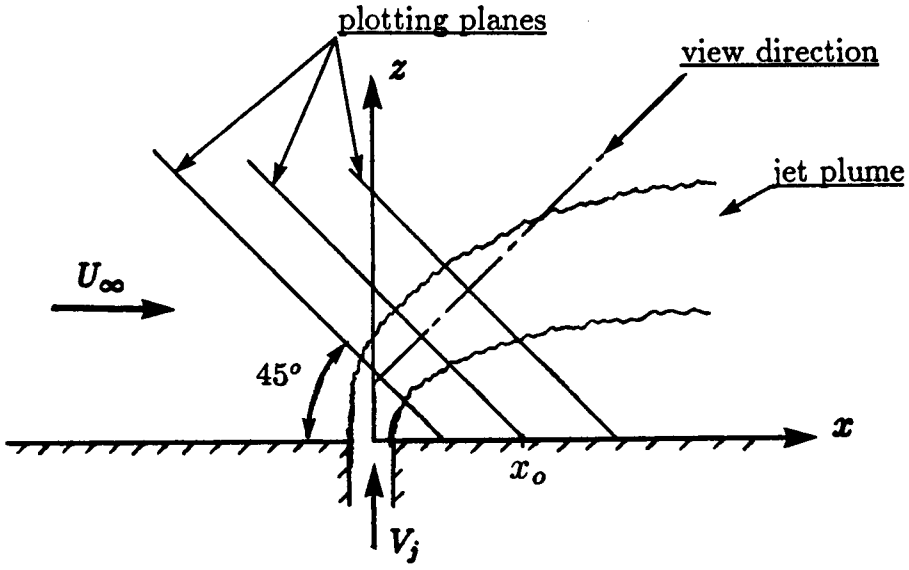
(c) cross-section plane (X = 7.6)

Figure 2.30 (continued).

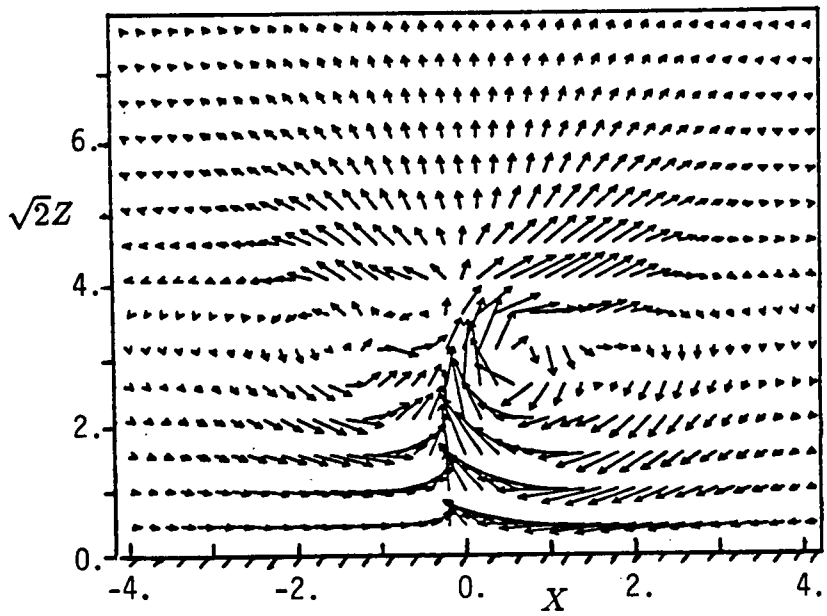
thus the oncoming flow suffered less resistance. In the cross-section plane, Figure 2.30 (c), the counter-rotating vortex pair is even more skewed than that in the $\beta = 45^o$ case. The vortex corresponding to the jet front corner was much stronger than the one corresponding to the rear corner.

The experimental results from References [68, 72] showed illuminated sectional-views at 45^o to the base plane (see Figure 2.31 (a)) and so similar sections are taken for the computed results discussed herein. Figures 2.31 (b) and (c) show two plots of computed results, and they are qualitatively comparable to the experimental results in Figure 2.31 (d); which are sectional view photographs obtained from laser-induced fluorescence studies [68, 72].

A major difference of the flow behavior in a $\beta = 30^o$ jet from that of a $\beta = 45^o$ jet is that the vortices form on both the wind-side (vortex A in Figure 2.32) and the lee-side (vortex B) at the front jet corner (corner F) in the 30^o jet case while only one vortex (vortex B) forms on the lee-side in the $\beta = 45^o$ case. As we have seen in Figure 2.21 (p.46), a symmetric wake vortex pair (vortices B and C in Figure 2.32) was formed behind the jet in the $\beta = 90^o$ case. When the angle β is reduced, these two vortices become asymmetric (vortex B is larger and stronger that vortex C) as we saw in the $\beta = 45^o$ case (Figure 2.26 (p.54)); but no vortex is formed on the windward-side of the corner F until β is reduced to less than a certain value (about 35^o to 40^o degrees). When β becomes less than this value, the flow starts to turn around from both sides of the corner F and form a weak vortex on the windward-side (vortex A). When β is continuously reduced, vortex A grows stronger while vortex C becomes weaker. Finally, vortices A and B become symmetric about the x–axis when β reaches zero as shown in Figure 2.33. The sketch in Figure 2.32 illustrates the phenomenon described above.

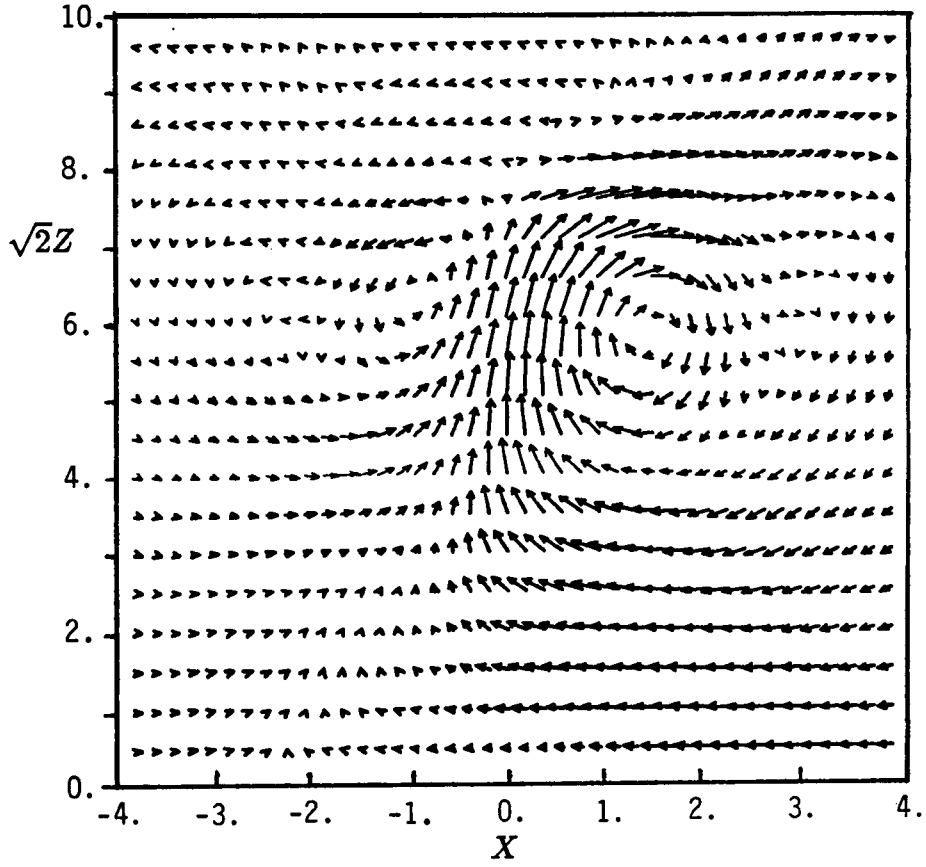


(a) schematic of plotting planes and view direction



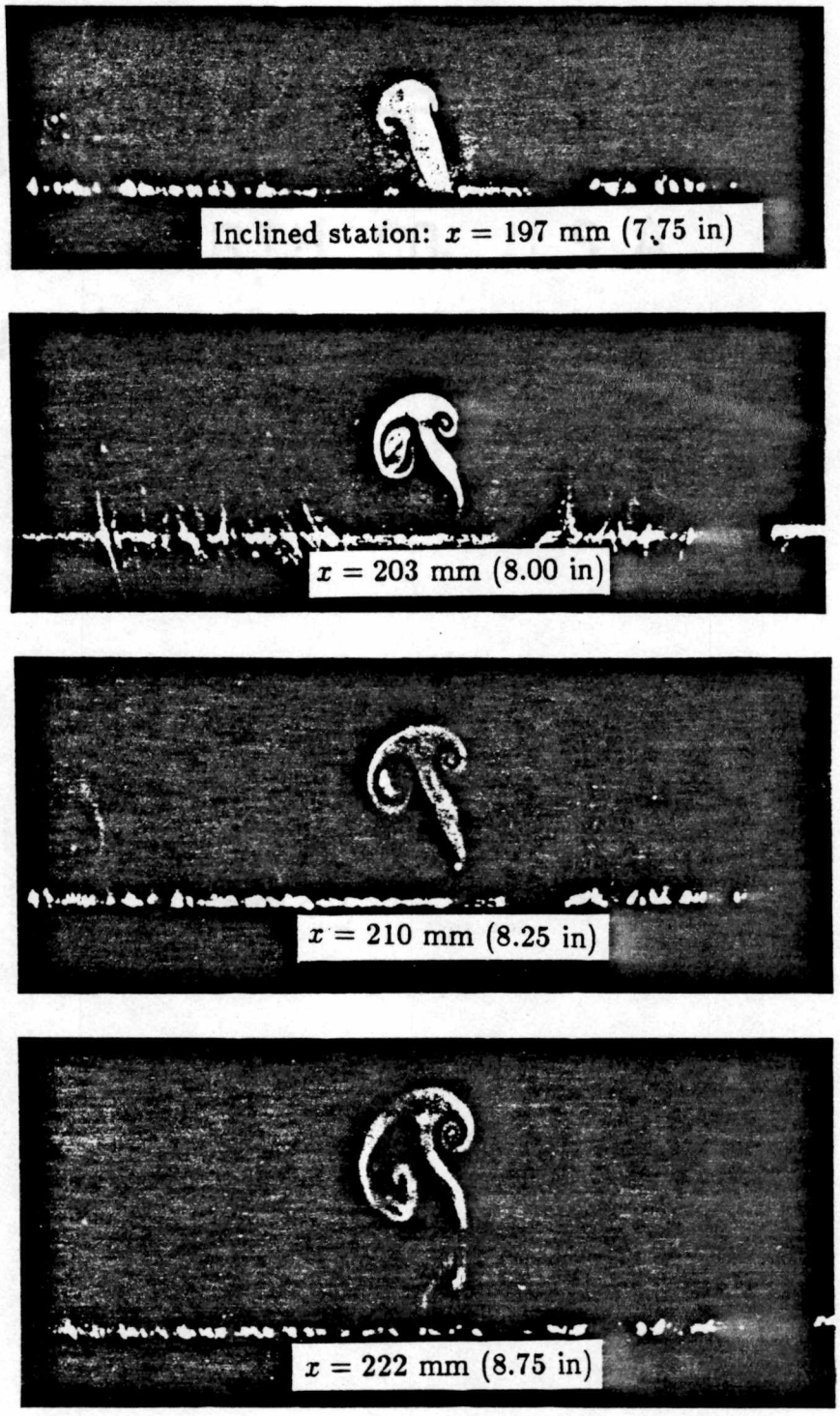
(b) computed results for $R = 2$ jet ($t = 3.0$, $X_o = 6.2$)

Figure 2.31 Cross-sectional views on 45° inclined plane at discrete x–stations.



(c) computed results for $R = 4$ jet ($t = 2.5$, $X_o = 14.5$)

Figure 2.31 (continued).



(d) laser-induced fluorescence sectional views (Wu, Vakili, & Yu, 1986, $R = 2$, $\beta = -30^o$, $Re_d = 470$)

Figure 2.31 (continued).

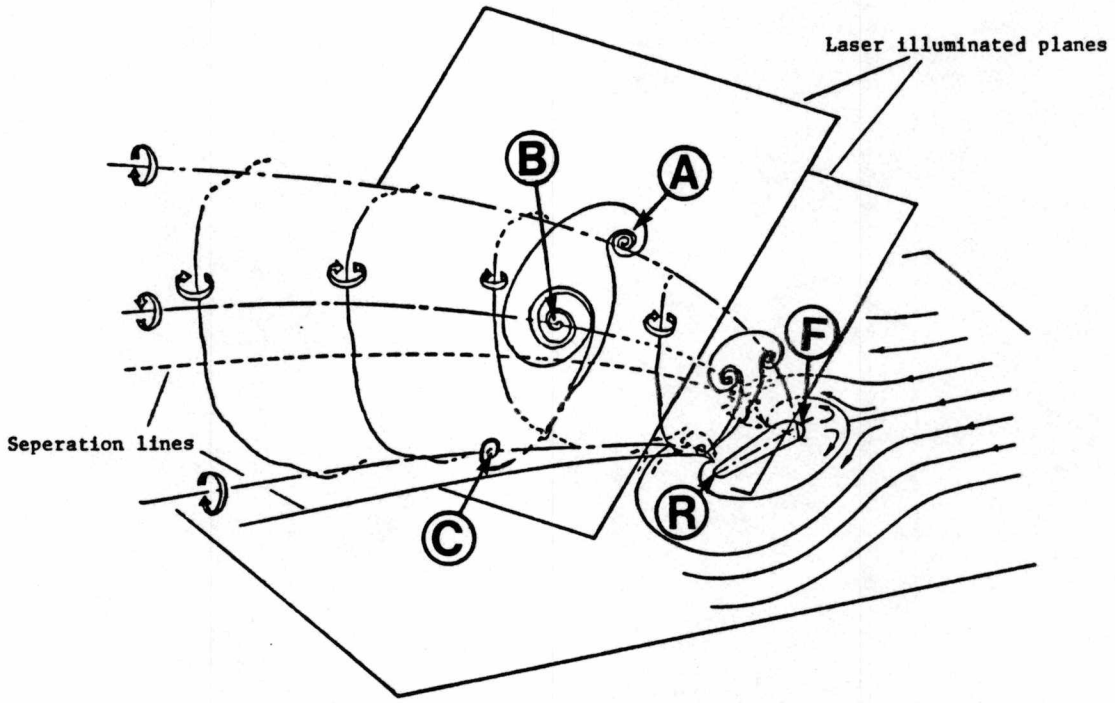


Figure 2.32 Schematic of the flowfield of a non-symmetric jet in crossflow (Wu, Vakili, & Yu, 1986).

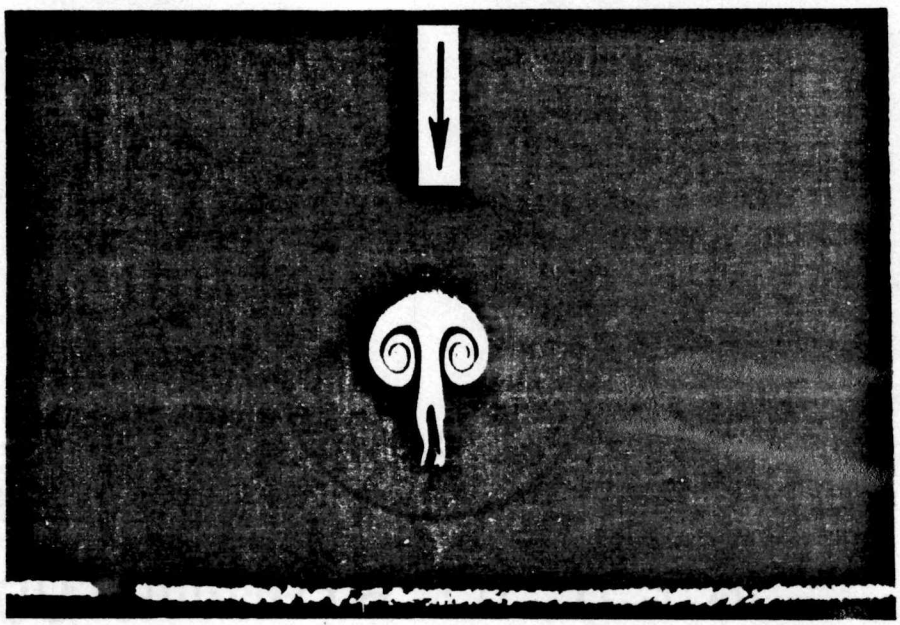


Figure 2.33 A 45° cross-sectional view of a slot-jet at $\beta = 0°$ (Yu, 1987, $R = 3$, $Re_d = 470$).

CHAPTER III

WATER TUNNEL EXPERIMENTS

The flow structure in the tip region of any lifting wing has a large influence on the performance of the wing. Ever since it has been recognized that the three-dimensional wing produced an induced drag, much effort has been made to reduce this drag and increase the lift/drag ratio by modifying the wing configuration, including its tip. Among numerous works done on this subject, Ayers and Wilde started the idea of improving the wing performance by using spanwise-blowing from the tips in 1956. Since then, much work has been done both experimentally [9, 24, 34, 35, 38, 45, 55, 57, 64–68] and theoretically [11, 12, 56] in this area.

Although it has been established that the wingtip blowing can improve the wing performance, the detailed flow structure and its physical mechanism are still not clear. The lack of clarity occurs because the wingtip flowfield with jet blowing is so complex. The tip flowfield is affected by a combination of free stream velocity, angle of attack, and the momentum of the blowing jet, thereby resulting in a flowfield which is unsteady, turbulent, and containing many vortices. Theoretical and computational studies of the wingtip flowfield have, therefore, become tremendously difficult. For this reason, a single non-symmetrically placed jet in a uniform crossflow was chosen as a preliminary model to study the basic flow phenomena around the wingtip with discretely positioned tip-jets.

The second part of this work is an experimental investigation of the flowfield around a wingtip with discretely positioned tip jets. With the knowledge gained from Chapter 2 and earlier experimental studies conducted by Wu, Vakili, and Yu [68, 71, 72], the structure and behavior of the flowfield created by wingtip-jet blowing became less difficult to understand. Both water-tunnel flow visualization

and surface oil-flow technique for the wind-tunnel model were used to establish the knowledge about the flowfield, and to identify the complicated vortex system generated by the wingtip jets. The water tunnel experiments are presented in this chapter, and the experiments conducted in the low-speed wind tunnel will be discussed in Chapter 4.

§ 3.1 Water Tunnel Facility

The flow visualization was conducted in the UTSI water tunnel. It is a closed circuit continuous flow facility especially designed for high quality flow visualization. Major components of the facility are illustrated in Figure 3.1. The circuit of the tunnel lay in a horizontal plane with the test section and a portion of the return circuit enclosed in a building. The test section is 30.5 cm high by 45.7 cm wide by 150 cm long (12 in. $\times$ 18 in. $\times$ 60 in.) and is constructed primarily of Plexiglas for versatility in observing and photographing the flowfield.

The tunnel is powered by a one horsepower electric motor connected via a variable speed transmission to a 25 cm diameter, twin-bladed propeller which was located at the second bend downstream of the test section. This system allows a continuous variation of tunnel speed from 1.5 to 60 cm/sec.

The tunnel is controlled from a control panel, where the propeller speed is displayed with a digital meter. This meter was calibrated against the tunnel flow velocity using a cylindrical hot-film probe.

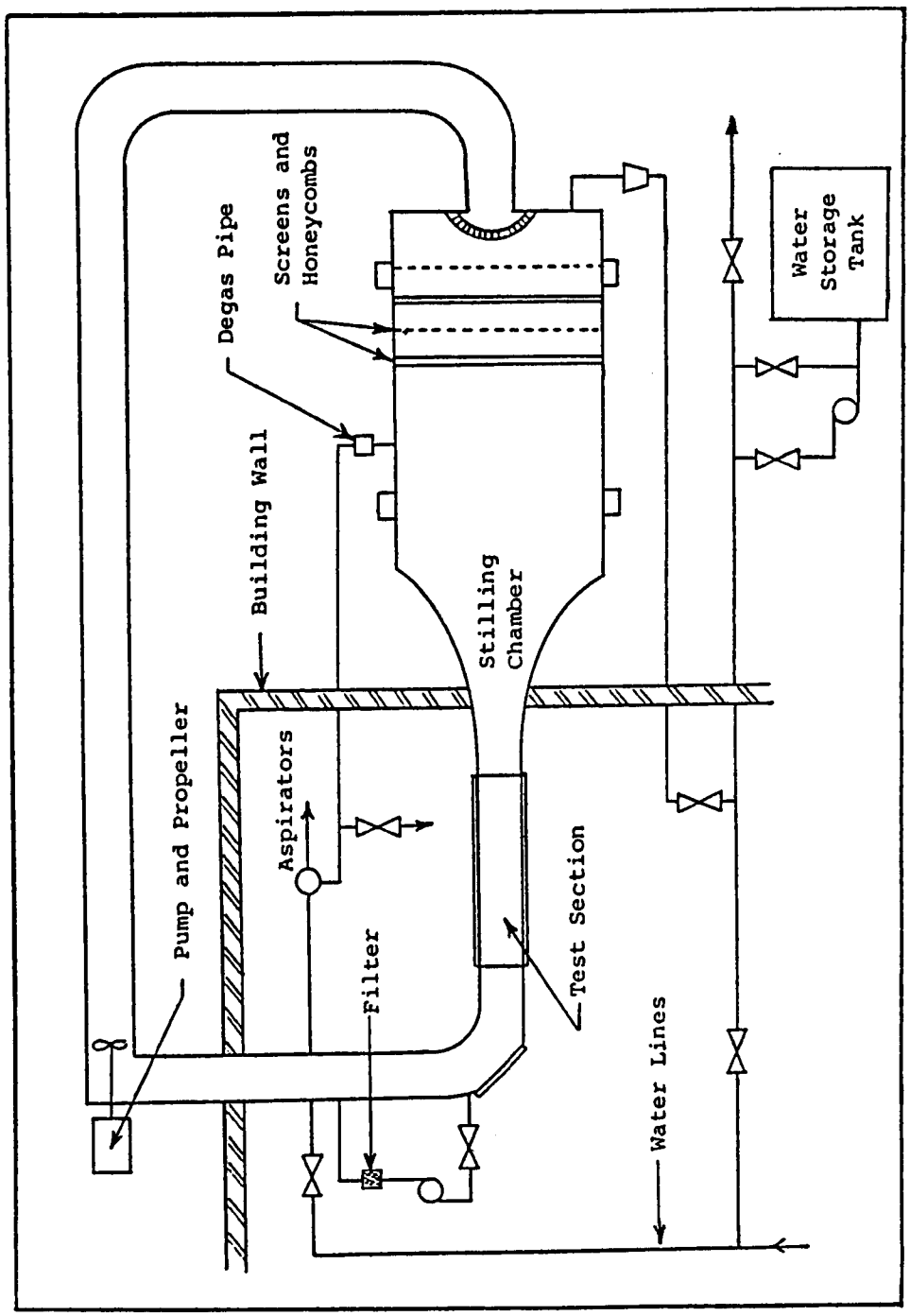


Figure 3.1 General layout of the UTSI water tunnel facility (Collins, 1982).

§ 3.2 Flow Visualization Technique and Analysis

Flow visualization was achieved by bleeding colored dye through several small holes located on the surface near the wingtip. As the dye was continuously supplied to the surface around the jet exit, it followed the roll-up of vortices and made them visible. Dye could also be introduced upstream or downstream of the model through several movable dye probes if needed.

The dye injection system consists of pressurized dye reservoirs which supplied the dye to the model through 0.17 cm diameter tubes. The dye flow rate was carefully controlled by adjusting the pressure in the dye reservoirs to insure that the dye velocity did not produce its own jet effect when it left the model. This also insured that the streak line traced by the dye was turbulent or unsteady only if the flow itself was turbulent or unsteady.

Two flow visualization techniques, regular colored dye and laser induced fluorescence, were used in this experimental study. The former gave the global flow pattern while the later was confined to selected cross-sections of the flowfield. The regular dye was a mixture of milk, alcohol, and commercial food color in such a composition so as to ensure that its specific gravity was equal to that of water.

Structure of the flowfields were recorded using regular photographs and video taped by a Panasonic video camera (VHS Omni Movie PV-530).

§ 3.3 Model Design and Experimental Set-up

The wing model used in this study was an NACA 0012-64 airfoil section with semi-span of 27.1 cm and chord of 16.2 cm and was made of aluminum. One end of the model was mounted to a shaft which extended through the side wall of the water tunnel. Model angle of attack was controlled by this shaft and measured

by a counter assembly exterior to the tunnel. The model was located at 12 inch from the beginning of the test section so that the free-stream was in good uniform condition yet permit visualization of vortex development for approximately 7 chord lengths downstream of the model trailing edge. The wingtip was located at 60% of the width of the tunnel. The maximum blockage of the model was less than 10%.

Three sweep configurations of the model were tested: unswept, backward swept, and forward swept. A zero dihedral angle was used for all cases. These configurations are described in Table 3.1, and Figure 3.2 contains the photographs of all three configurations.

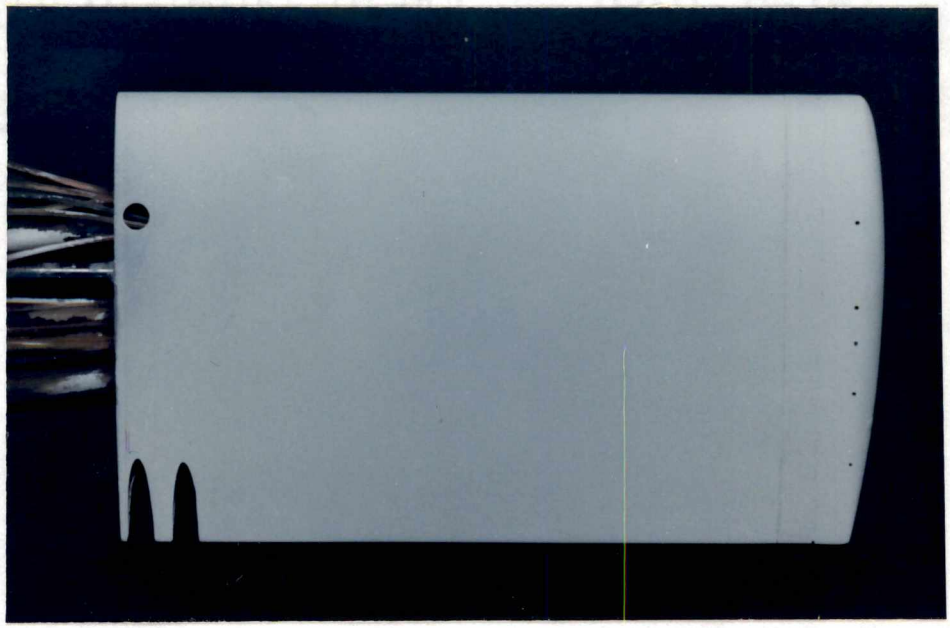
Table 3.1 Swept Model Descriptions

Configuration	Sweep Angle*	Effective Chord Length
Unswept	0	6.375"
Backward Swept	30^o	7.155"
Forward Swept	-30^o	7.155"

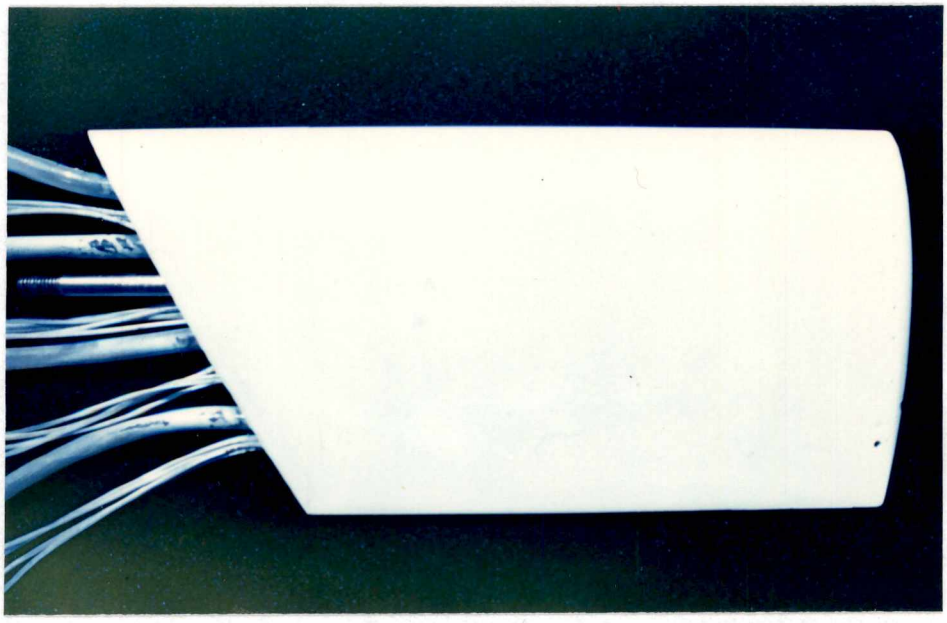
* The sweep angle was measured from the direction normal to the free-stream.

The models were designed such that the wingtips were interchangeable on the airfoil base. So the different blowing configuration could be achieved for each sweep configuration without great difficulty. A sketch of a wingtip is shown in Figure 3.3 (a).

Three types of wingtip jets were used in this study. Type I tip utilized three rounded end rectangular shaped tip-jets which were located on the outboard edge

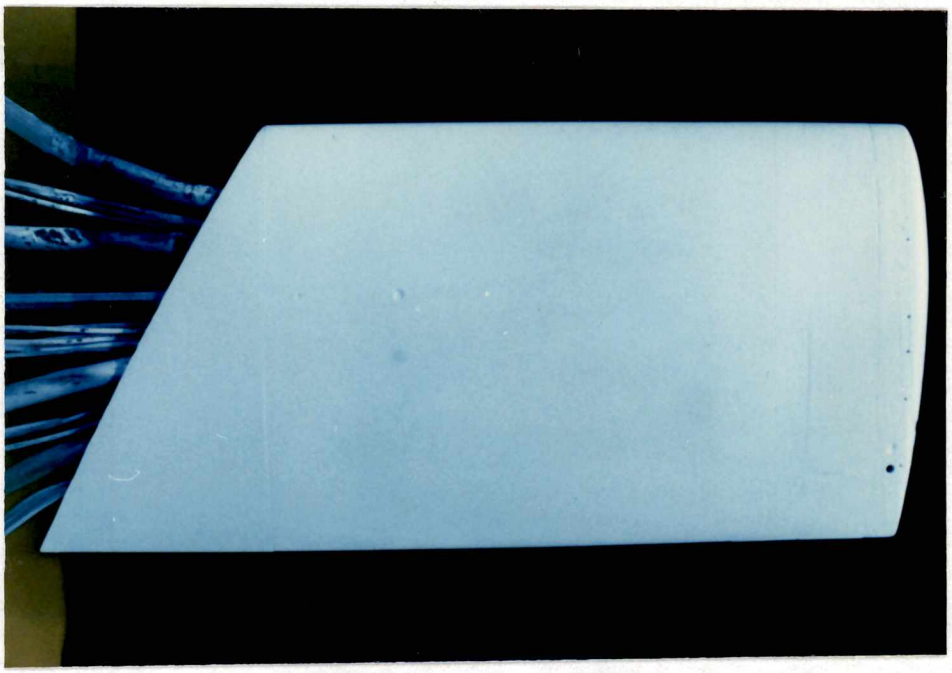


(a) unswept configuration

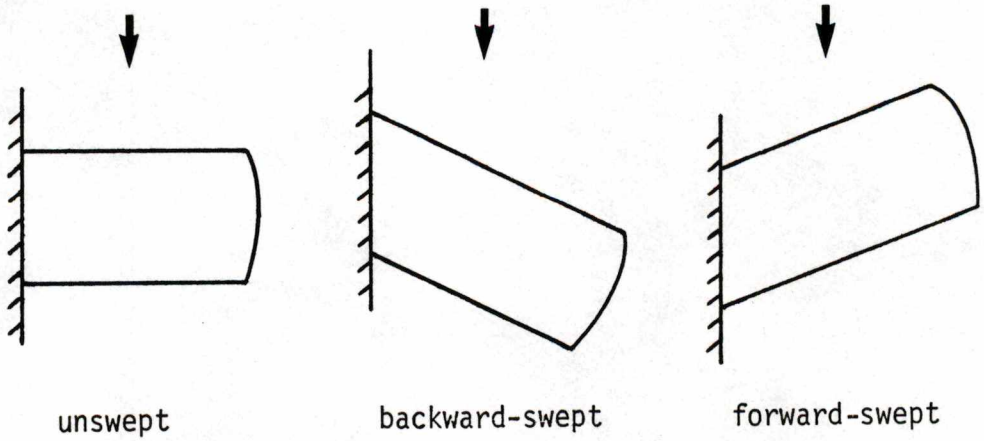


(b) backward swept configuration

Figure 3.2 Basic models used in water tunnel experiments.

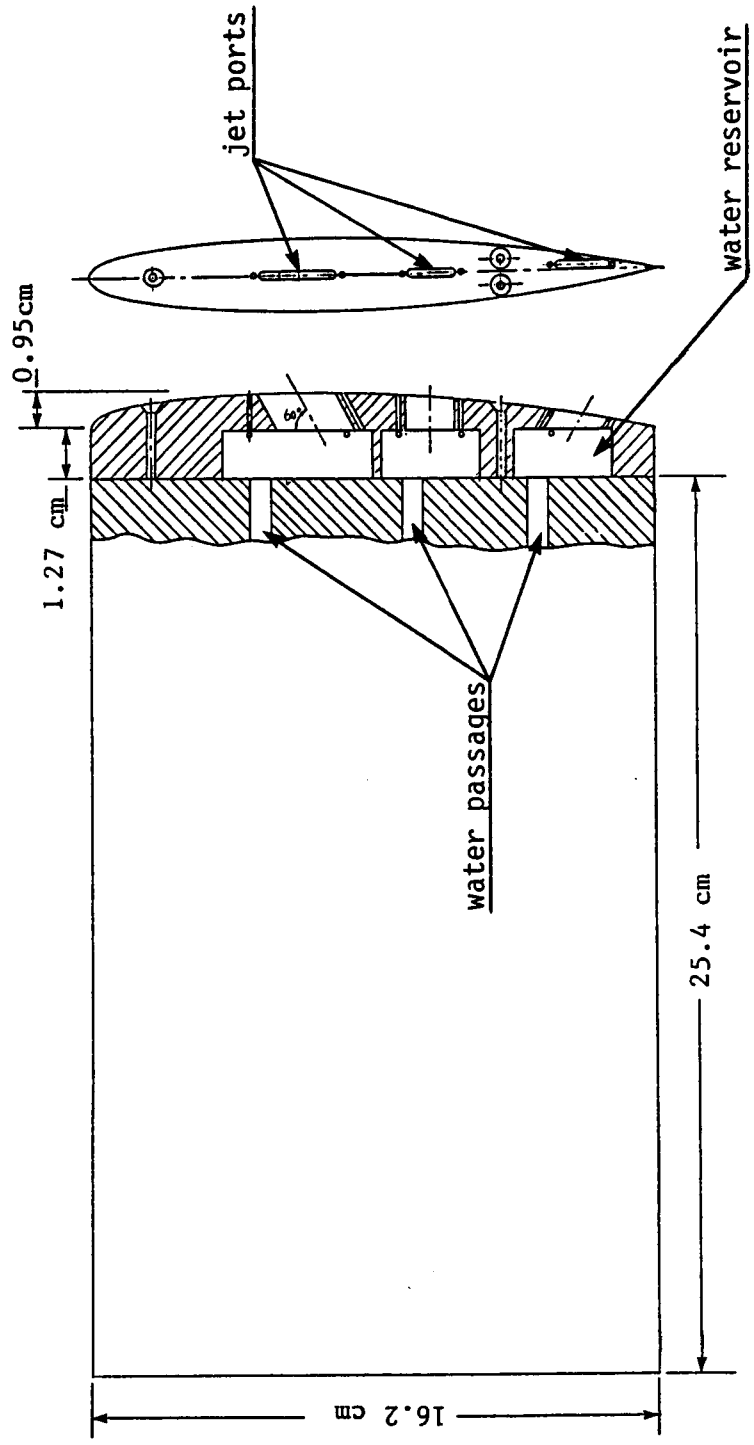


(c) forward swept configuration



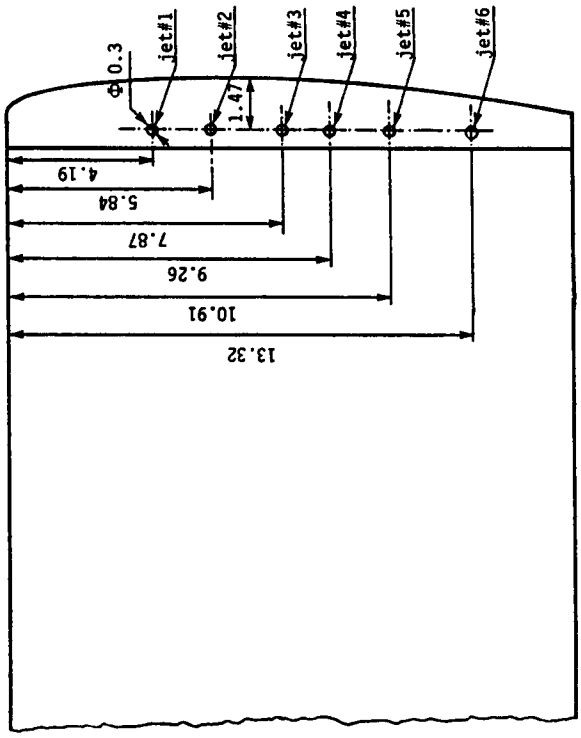
(d) sketch of the swept configuration

Figure 3.2 (continued).

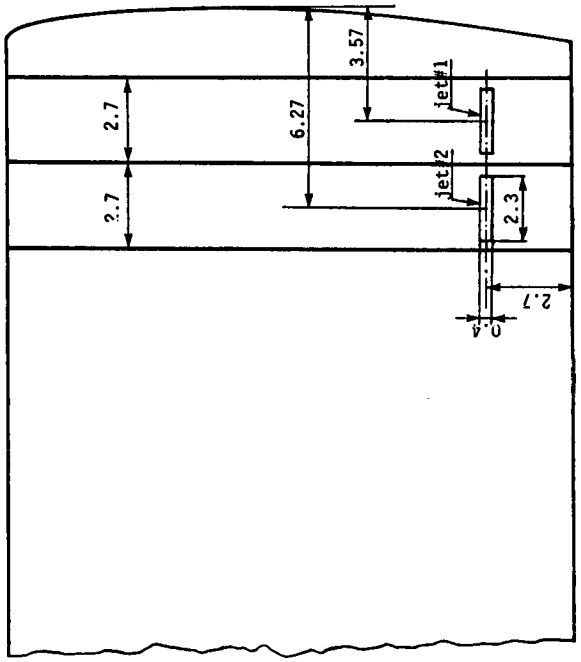


(a) Type I tip configuration

Figure 3.3 Wingtip configurations used in water tunnel experiments.



(c) Type III tip configuration



(b) Type II tip configuration

(all dimensions in cm.)

Figure 3.3 (continued).

of the wingtip as shown in Figure 3.3 (a). Table 3.2 lists the configuration of this tip. Type II tip utilized slot-jets which were located on both the upper and lower wing surfaces and parallel to the trailing-edge as shown in Figure 3.3 (b). The type III tip contained six circular holes which were located on both the upper and lower wing surfaces. The configuration of the type III tip is shown in Figure 3.3 (c).

Table 3.2 Jet Configurations of Tip I

Jet Port	Sweep Angle*	Dihedral Angle**	Length	Width
jet port 1	-30^o	0^o	22.2 mm	1.8 mm
jet port 2	0^o	0^o	13.7 mm	1.8 mm
jet port 3	30^o	-15^o	16.5 mm	1.8 mm

* Sweep angle 0^o was measured from the direction of the leading-edge.

** Dihedral angle was positive for blowing upward from wing's center plane.

The jet ports were simple openings machined through the tip surface into the water reservoirs built inside the wing. The water to the jet ports was supplied from a water line via three 3.5 mm inner-diameter tubes. The flow rate in each tube was measured by a flowmeter and could be individually controlled. Various combinations of jets and jet blowing ratios were used to investigate the effects of the blowing. During these experiments, any un-selected jets were temporarily plugged to isolate their effects.

§ 3.4 Water Tunnel Test Results and Discussion

A. Wingtip Flowfield due to Single Jet Blowing

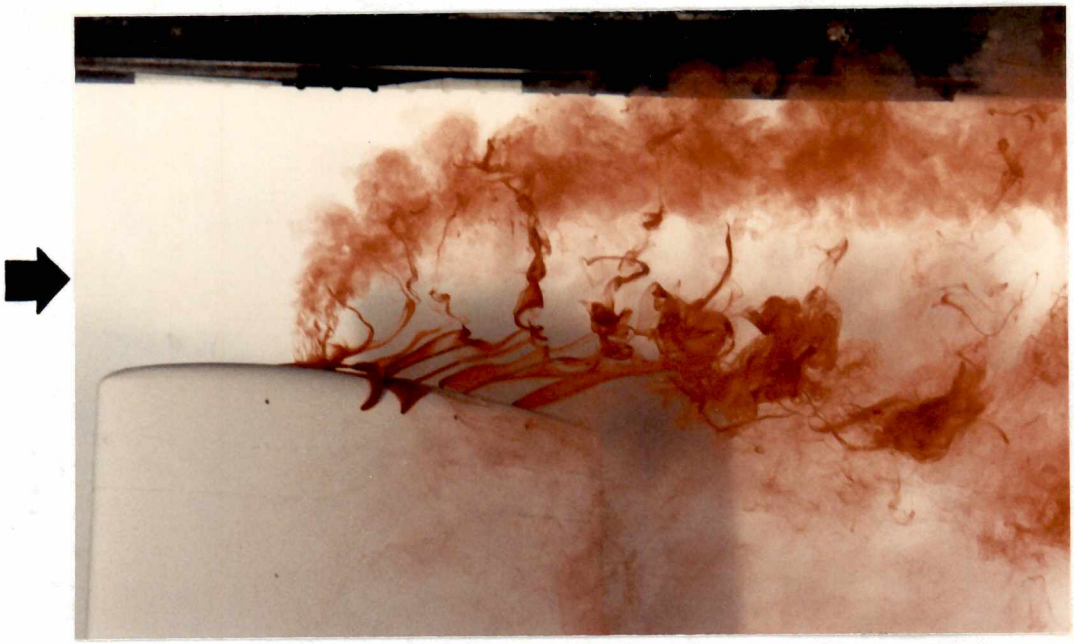
The experimental study of an asymmetric single jet in a crossflow conducted by Wu et al. and the numerical investigation in Chapter 2 led to a better understanding of this type of flow. This knowledge provided a good base for a further study of the flowfield around a wingtip with blowing jets. During the water tunnel testing, it was found that the complicated flowfield created by a wingtip-jet blowing contains many of the basic phenomena that were observed for a single jet in a uniform crossflow. This confirms the importance and usefulness of the basic model studied above.

The non-dimensional parameters used in the water tunnel study were the jet-to-crossflow velocity ratio R and the jet momentum coefficient C_μ, which was defined as

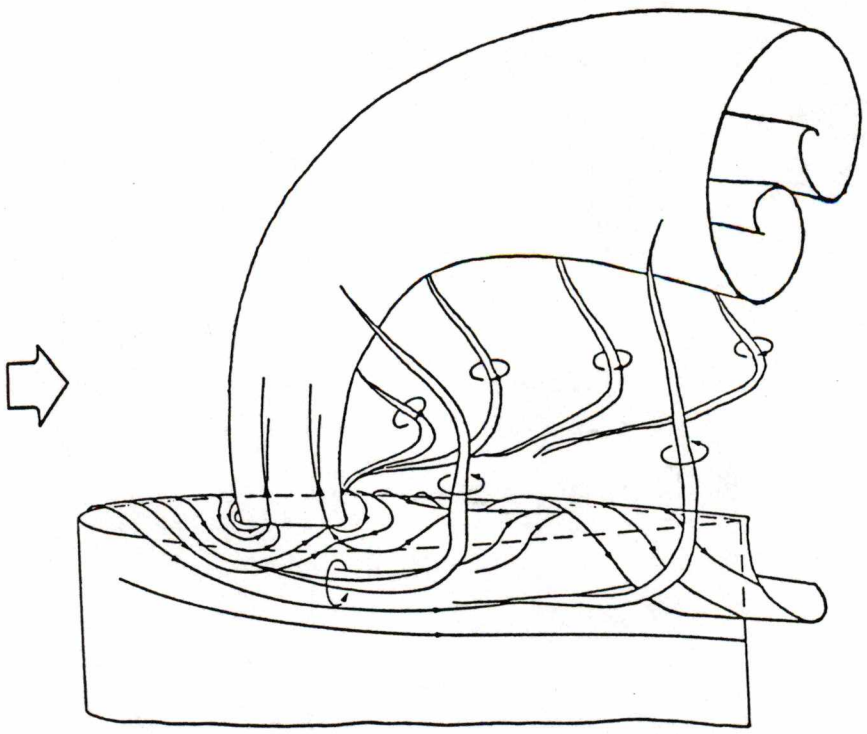
$$C_\mu = \dot{m}V_j/0.5\rho U_\infty^2 S,$$

where $\dot{m}$ is the jet mass-flow rate, V_j is the jet-exit velocity, U_∞ is the freestream velocity, and S is the semispan wing area.

In order to compare the test results with the established knowledge of the subject, a single wingtip-jet blowing at different locations were first investigated. It was found that the flow pattern created by a single wingtip-jet was similar to that of a non-symmetric plane-jet in a uniform crossflow but with the composition of the wingtip effect. Figure 3.4 (a) is a photograph of a typical single wingtip-jet flowfield, and Figure 3.4 (b) is a sketch of the same flowfield. The similarity between this flow pattern and that of a single non-symmetric plane-jet (shown in Figure 3.4 (c)) can be seen by a comparison of these figures.



(a) tip-jet #1 blowing ($U_\infty = 4.3$ cm/s, $\alpha = 24^o$, $C_\mu = 0.07$)



(b) a sketch of wingtip flowfield

Figure 3.4 Flow pattern for the wingtip with a single blowing jet.



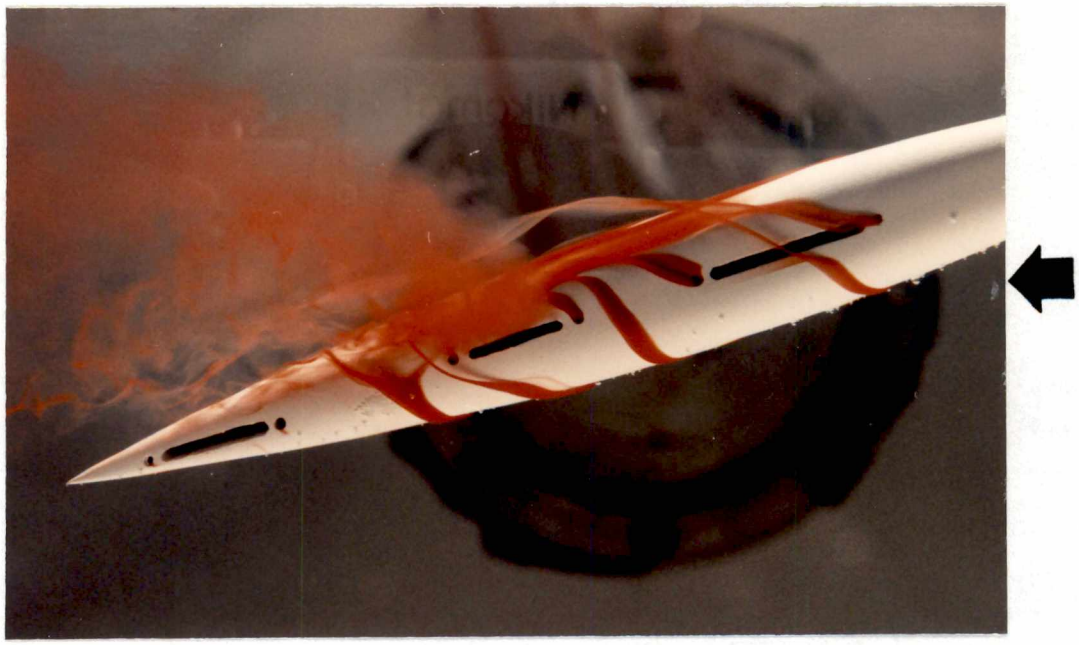
(c) single non-symmetric jet in crossflow (Wu, Vakili, & Yu, 1986, $R = 3.3$, $\beta = 20^o$, $Re_d = 240$)

Figure 3.4 (continued).

Some distance upstream of the jet, the flow pattern appeared to be similar to that without jet blowing, with the flow rolling from the lower to the upper surface of the wing. Due to the presence of the wingtip jet plume downstream, however, the fluid rolling from the lower surface could not roll-up to form a tight tip-vortex as it would in a no-blowing case. Instead, part of this fluid was rolled into the jet-wake to form the wake-vortices which have completely different orientations from the regular wingtip vortex (see Figures 3.4 (b) and Figure 3.5).

Near the jet-exit, a typical interaction of a non-symmetric jet with a crossflow started to appear, the original wingtip effect was mainly shown as a change in the on-coming flow direction, i.e., the flow came non-uniformly from the lower surface of the wingtip while flowing downstream. Near the wing surface, the oncoming fluid moved around the jet and formed two shear layers on each side of the jet plume. On the lee-side of the jet, the wing surface boundary layer was spiraled into the low pressure region behind the jet and separated from the wing surface. The wing surface boundary layer vorticity was then free to stretch and turn to form the vertical wake vortices. Similar to the plane non-symmetric jet in a uniform crossflow, the jet-plume itself was dominated by the counter-rotating vortex pair and had a kidney shaped cross section. The structure of the flowfield around the wingtip with a tip jet was shown in Figures 3.4 to 3.6, and was very comparable to what have been known for single plane-jet from the experiments [68, 71, 72] and the discussion of Chapter 2. Figure 3.6 (a) shows a near surface flow-pattern around the blowing tip-jet; this pattern is very similar to that of a non-symmetric plane-jet shown in Figure 3.7.

About one or two jet-diameters downstream from the jet, the flow pattern near the wing surface gradually returned to the usual wingtip flow pattern. It still rolled-up from the lower surface to the upper surface but with lesser rotational



(a) side view



(b) top view

Figure 3.5 Global view of the flowfield for single wingtip jet blowing (Tip I, jet #2, $U_\infty = 8$ cm/s, $\alpha = 16°$, $C_\mu = 0.02$).



(a) side view



(b) top view

Figure 3.6 Near surface flow pattern for single jet blowing (Tip I, jet #1, $U_\infty = 8$ cm/s, $\alpha = 16^o$, $C_\mu = 0.02$).

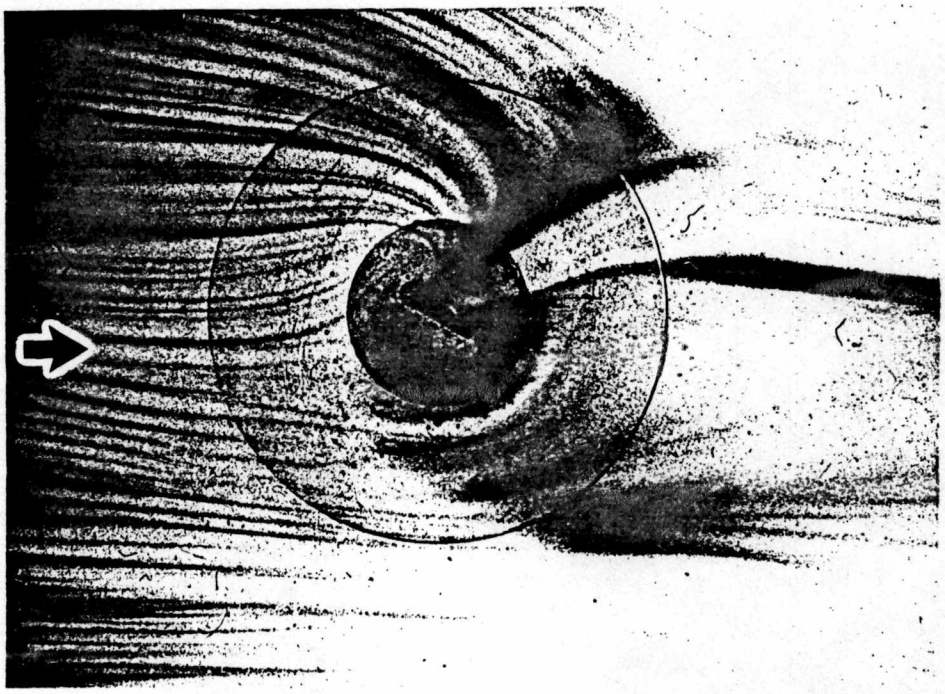


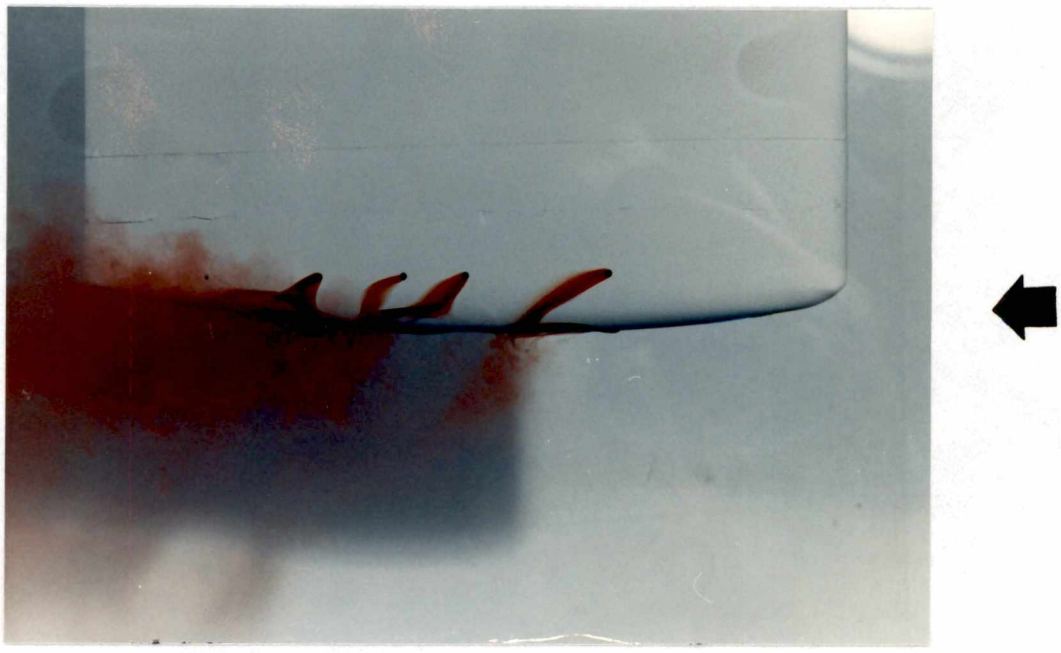
Figure 3.7 Near surface flow pattern for a non-symmetric jet in crossflow (Wu, Vakili, & Yu, 1986, $R = 9$, $\beta = 31^o$, $Re_d = 240$).

tendency than found in a no-blowing case. This phenomenon can also be seen in Figures 3.4 (b) and 3.5. From the above discussions, it is clear that the tip-jet blowing expanded the original tight tip-vortex.

Multi-jets blowing cases were also tested. It was found that if two jet ports were far enough apart and with only a small C_μ, then each jet would behave the same as if it were a single jet. There would, however, be a big interaction between two jets if they were closely placed and with higher C_μ, or if one jet was placed in the wake of another. Figure 3.8 shows a two jets blowing case, where the interaction was small owing to the small C_μ for each jets. A flow pattern for a three jets blowing case is presented in Figure 3.9; there is also no large interaction between the blowing jets.



(a) side view

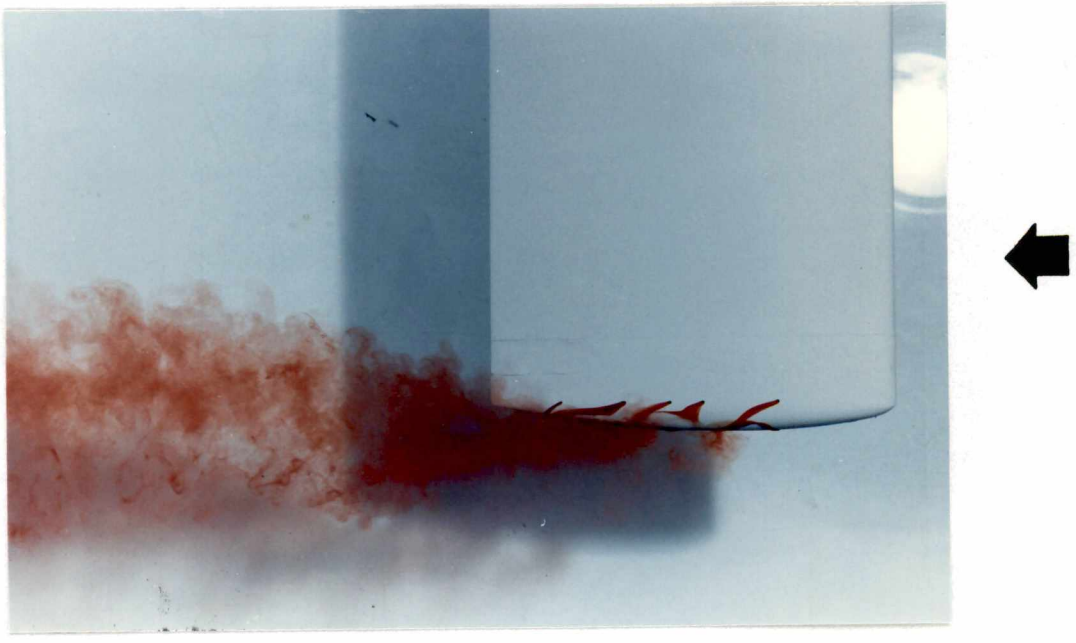


(b) top view

Figure 3.8 Near surface flow pattern for two jets blowing (Tip I, $U_\infty = 8\text{cm/s}$, $\alpha = 16^o$, $C_{\mu I} = C_{\mu II} = 0.02$).



(a) side view



(b) top view

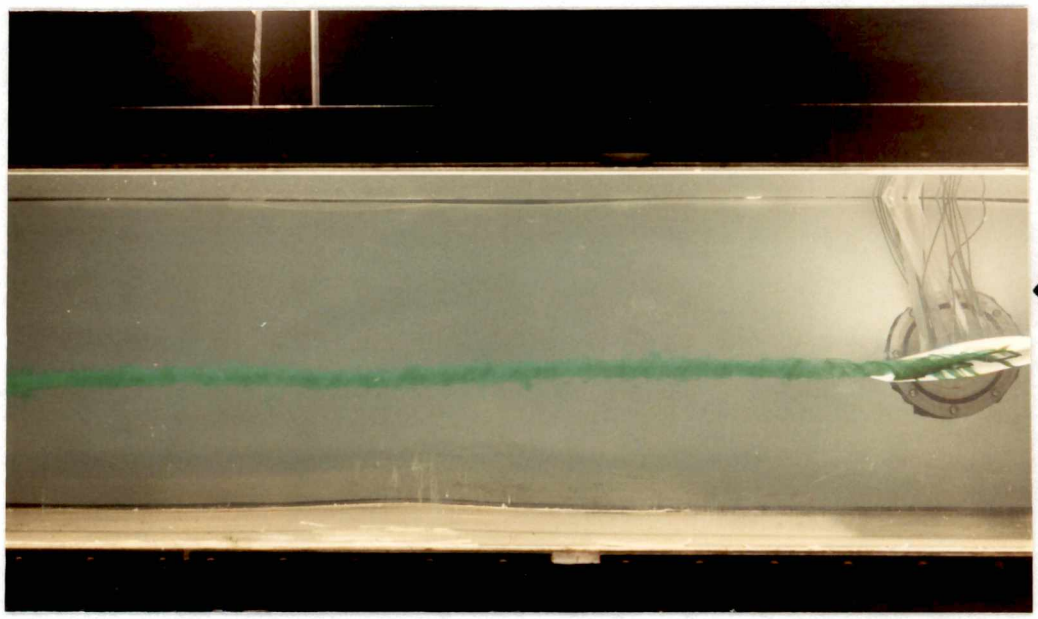
Figure 3.9 Flow pattern for three jets blowing (Tip I, $U_\infty = 8$cm/s, $\alpha = 10^o$, $C_{\mu I} = C_{\mu II} = C_{\mu III} = 0.02$).

B. Effects of Wingtip Blowing on the Tip-Vortex Flow

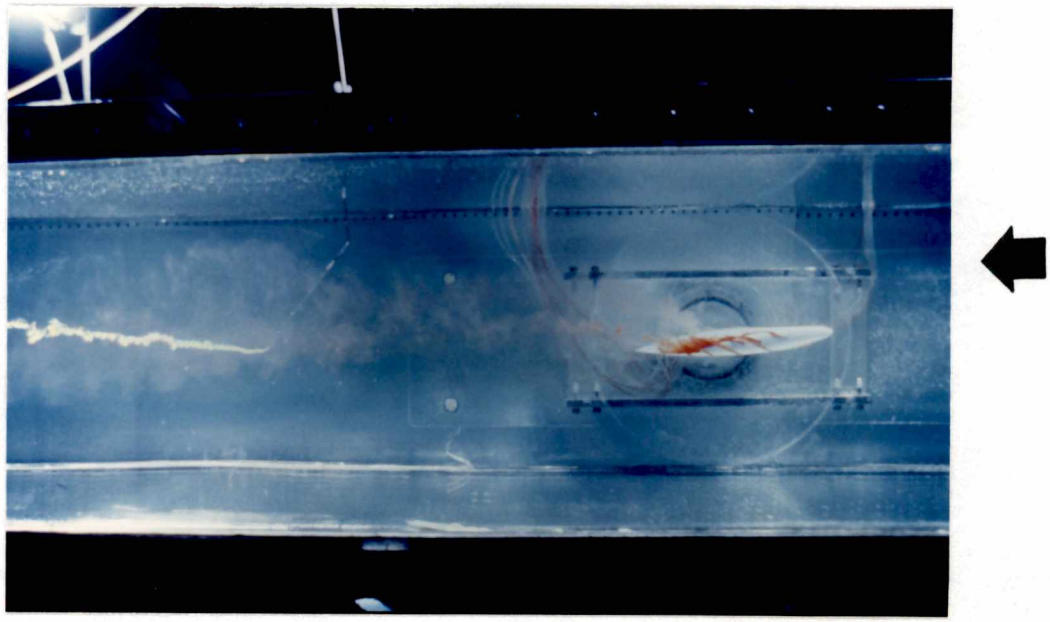
The effects of wingtip jet blowing on the tip vortex flow were investigated. Experimental results show that jet blowing from near the wingtip area can effectively alleviate the tip vortex formation, thus reducing the induced drag. Figure 3.10 (a) exhibits the well known phenomenon that a lifting wingtip vortex core flow can persist far downstream with little dispersion. This tip vortex flow, however, can be dispersed significantly by employing the wingtip jets as shown in Figure 3.10 (b). It has been observed that the wake of the wing with tip-blowing-jets was very unsteady and contained many vortices. This wake flowed downstream with much less global rotation than was in the no-blowing case where the tip vortex core rolled-up tightly. It was also observed that the tip wake flow shifted slightly upward and outward from its original location and its cross-section area enlarged considerably due to the tip-jet blowing as shown in Figure 3.10.

The flow structure of a non-symmetric jet in a crossflow described in the previous sections may explain why the jet blowing had such an effect on the wingtip vortex dispersion. The wingtip-jet creates its own vortex system in the region where the wingtip vortex originally would form. Instead of forming a single, well organized tip vortex in the no-blowing case, the newly formed flowfield is now unsteady, turbulent, and contains many vortices which rotate in various directions, i.e., the new flowfield is very disorganized. Even though the entire wake flow may still have a global rotation due to the lower pressure on the upper wing surface, it does not have a tightly rolled-up vortex core; the formation of the tip-vortex is thus alleviated.

Single jet blowing at various locations were intensively tested. It was found that jet blowing at any location near the tip would, in general, have a positive



(a) without jet blowing



(b) upper circular-jets blowing (all 6 jets, $C_\mu = 0.087$)

Figure 3.10 The effect of wingtip-jet blowing on the tip vortex dispersion ($U_\infty = 9cm/s, \alpha = 8^o$).

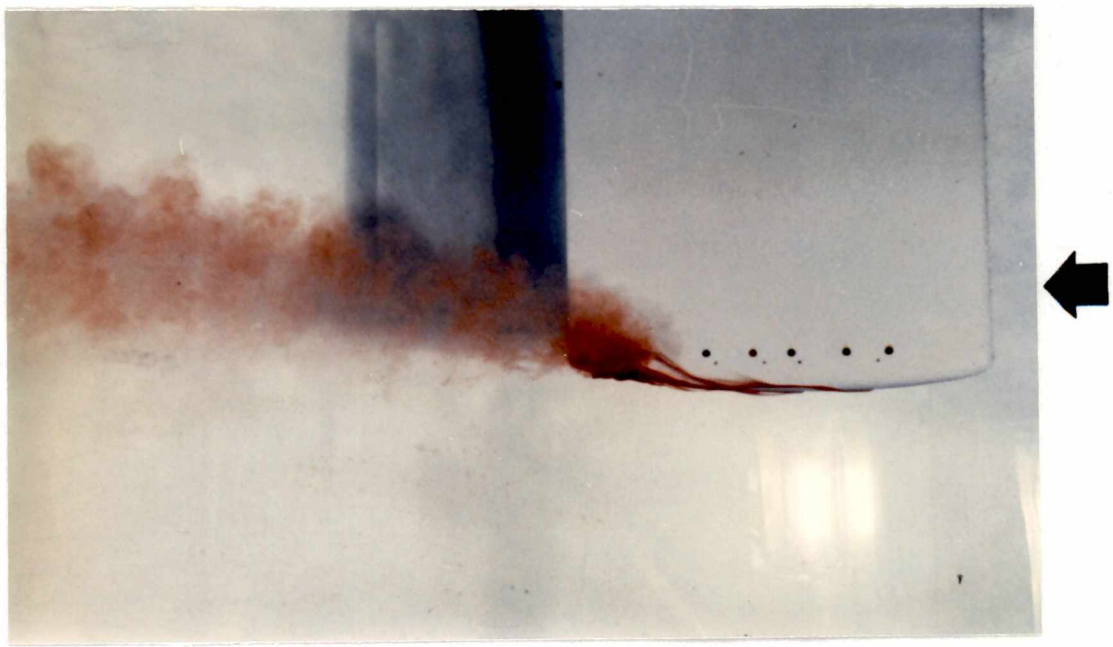
effect on the wingtip vortex dispersion. But, depending on the combinations of location and the amount of jet blowing, various degrees of dispersion resulted. The reason for this is obvious; the jet generated flowfield is rather localized and much smaller compared to the whole wingtip flowfield. The key point for a jet to have a significant impact on the large wingtip flow pattern lies on the fact that the jet should be placed at the onset of the wingtip vortex. Some conclusions drawn from our experiments are listed in the next few paragraphs.

In the spanwise direction, the experiments showed that in order to have an effective dispersion, the jet-ports should be placed very close to the wingtip. If a jet was placed too far from the tip, it would hardly have an effect on the wingtip vortex due to the distance separating the jet flow and the wingtip vortex. The jet No. 2 on Tip 3 was found to be such a case.

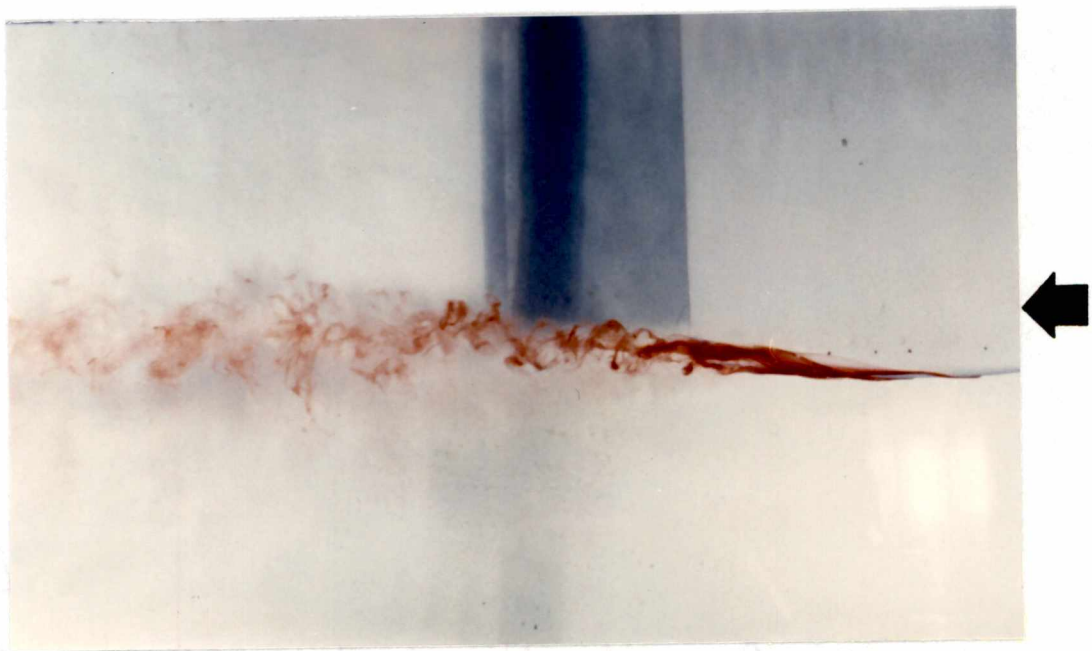
If the jet was placed too close to the leading-edge, the tip-vortex would form some distance downstream of the jet. On the other hand, if the jet was placed too close to the trailing-edge, the tip-vortex would form ahead of the jet. This confirms the notion that the wingtip vortex should be prevented at its onset. Multi-jets blowing cases were also tested and proved to be effective in increasing the dispersion effect. This operation was, however, usually associated with a larger mass flow rate.

Both upper and lower surface jet blowing was tested. It was found that the upper surface jet blowing was much more effective than the lower-surface jet blowing. Figure 3.11 shows the tip-vortex dispersion by the upper and lower surface blowing at the same jet momentum coefficient.

The experimental results also show that the shape of the jet-port did not play a critical role on the tip-vortex dispersion, this was because the basic phenomenon of a jet in a crossflow is not much affected by the shape of the jet orifice.



(a) upper-surface jets blowing (jets #4, 5 & 6, $C_\mu = 0.04$)



(b) lower-surface jets blowing (jets #4, 5 & 6, $C_\mu = 0.04$)

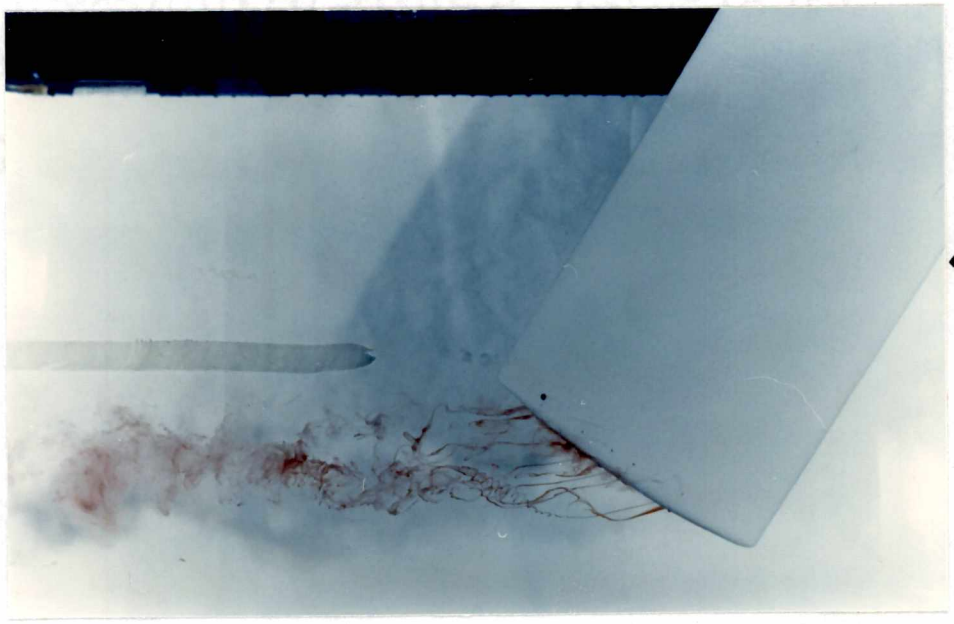
Figure 3.11 Tip-vortex dispersion by upper and lower circular jets blowing ($U_\infty = 9$cm/s, $\alpha = 8^o$, Tip III).

Thus, for each different free-stream velocity and wing angle of attack, there should be a best combination of number of jet ports, their locations, and their blowing rate which may lead to a most favorable effect on the dispersion of the wingtip vortex. In general, more jets blowing with higher C_μ will lead to a better dispersion of the wingtip vortex. It should be point out, however, that this is not so good from a practical point of view as more mass-flow and pump power is now needed.

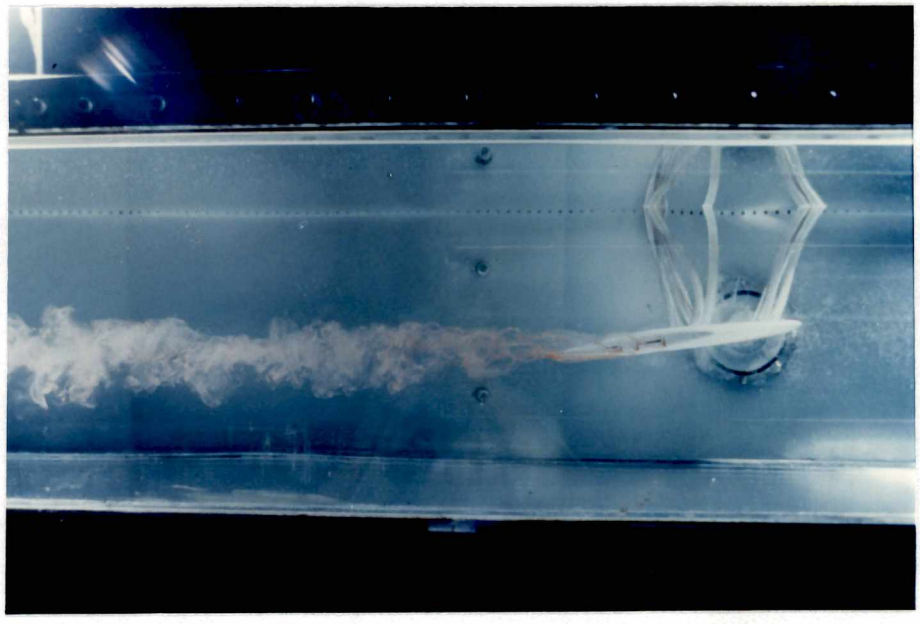
C. Wingtip-Jet Blowing on Swept Wings

Both backward and forward swept wing models were tested in order to observe the effects of the jet blowing in these cases. Figure 3.12 shows the wingtip vortices on the backward sweep model without tip-jet blowing. The vortices were much looser compared to those in the unswept case, this was due to the shape of the model in which the trailing-edge of the wingtip was hidden in the wake of the wingtip leading-edge. The experimental observation showed that the jet blowing was still helpful for the tip-vortex dispersion but had less effects because the tip-vortex was originally weaker. Figure 3.13 contains two photographs which show the effect of blowing on the backward-swept configuration.

Similar experiments were carried out for the forward-swept model. The wingtip flowfields for the forward-swept model in the non-blowing case were similar to those of delta-wing leading-edge vortices as shown in Figure 3.14. The whole tip-vortex system was much looser compared to the unswept wingtip vortex, and the "leading-edge" vortex burst somewhere on the upper surface of the wing depending on the wing angle of attack. The flowfield appeared rather turbulent after the burst, but still had a global rotation shown in Figure 3.14. Similar to the

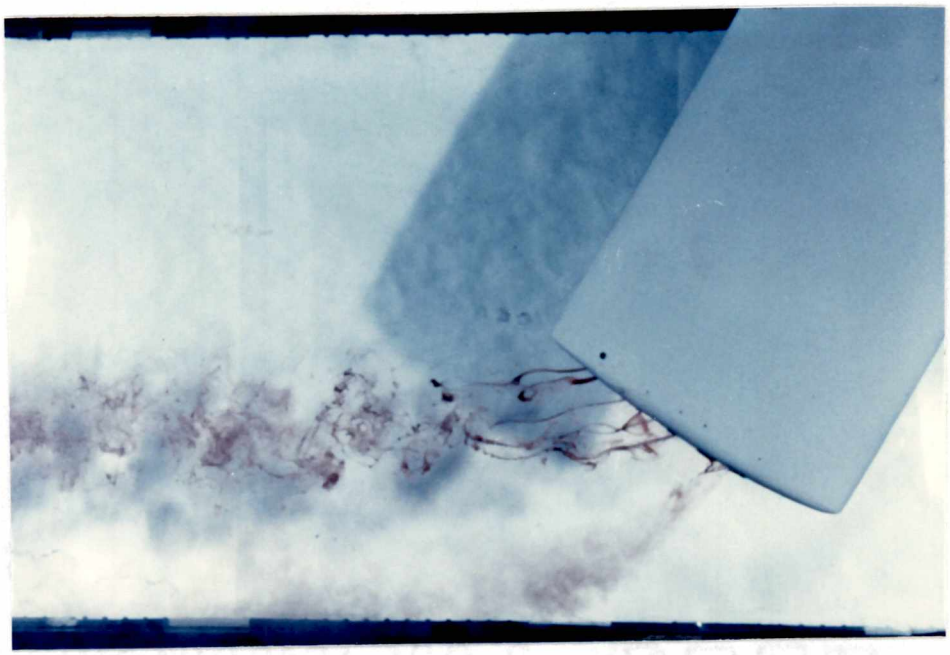


(a) top view

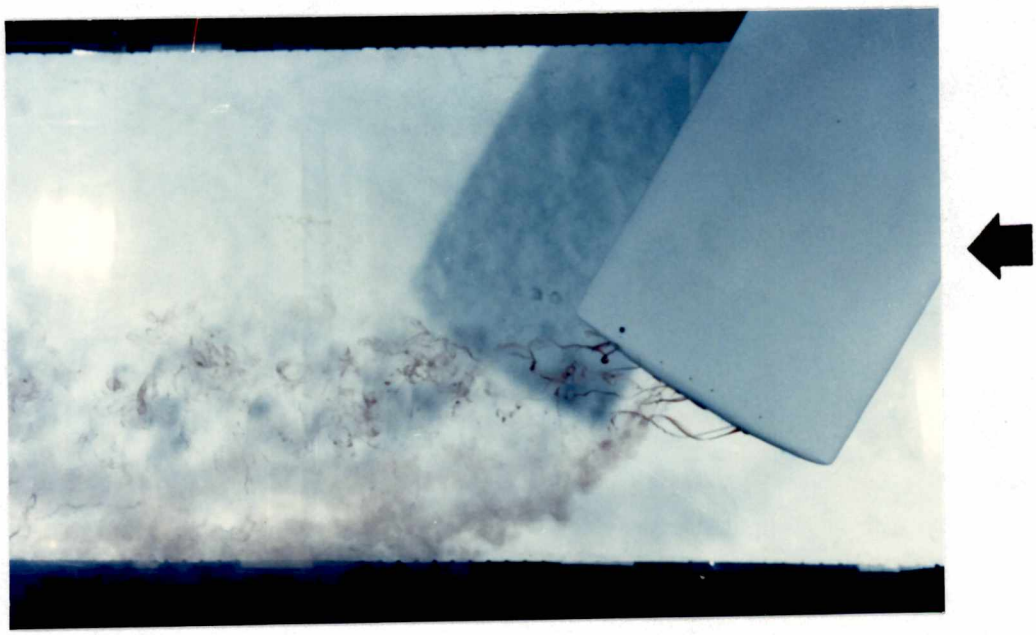


(b) side view

Figure 3.12 Wingtip vortex for backward-swept wing without blowing ($U_\infty = 9$ cm/s, $\alpha = 8^o$).



(a) tip-jet #1 blowing ($C_\mu = 0.016$)

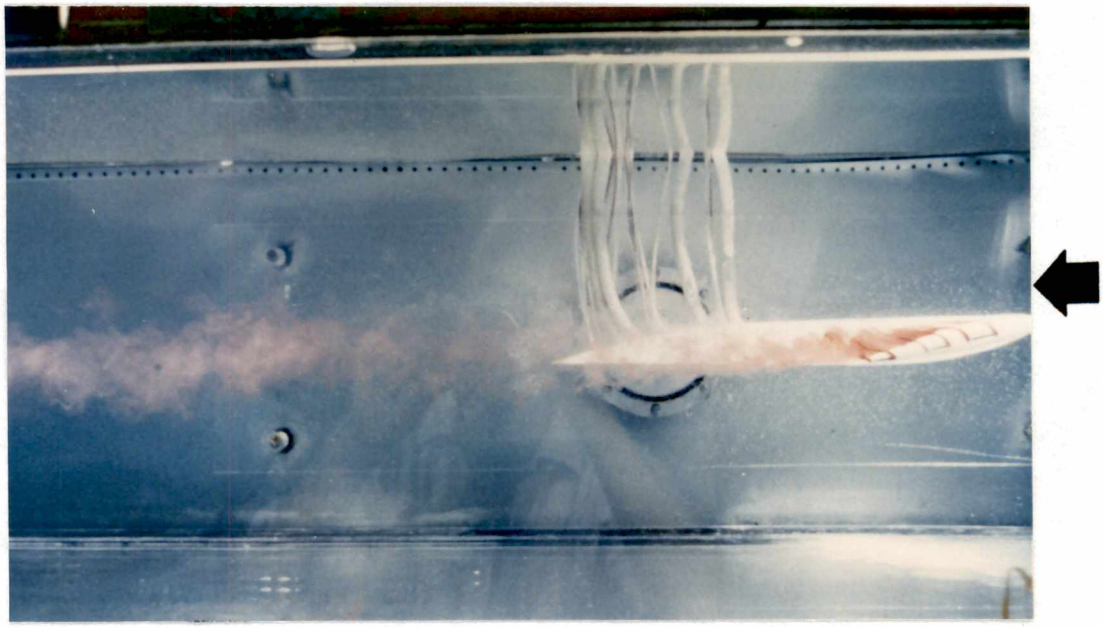


(b) tip-jet #2 blowing ($C_\mu = 0.027$)

Figure 3.13 Flowfield on the tip area of a backward-swept wing with tip-jet blowing ($U_\infty = 9$ cm/s, $\alpha = 8^o$, Tip III).



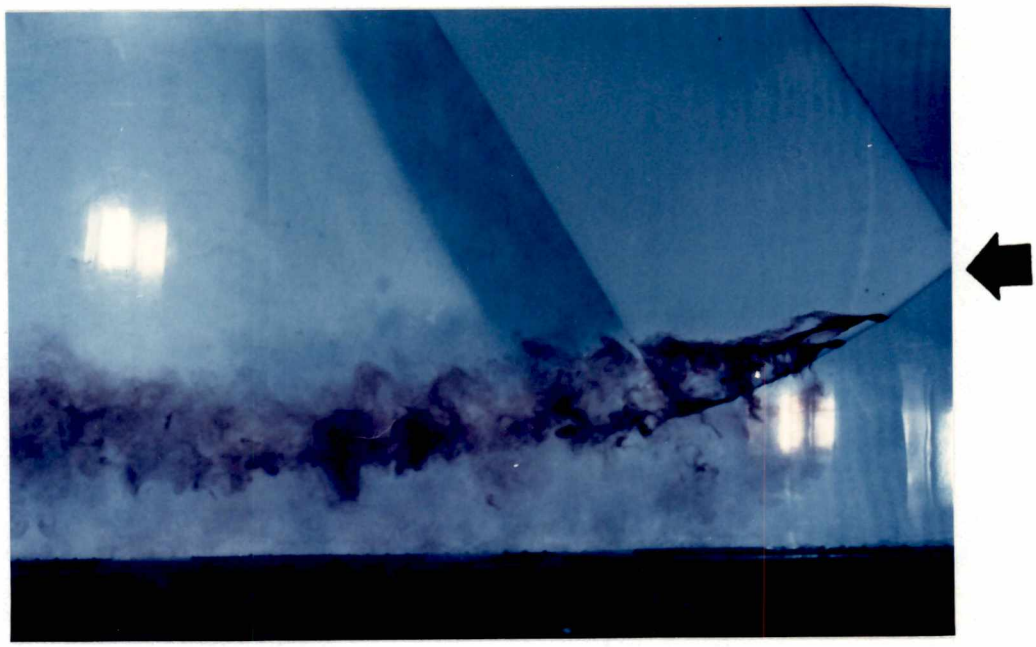
(a) top view



(b) side view

Figure 3.14 Wingtip vortex for forward-swept wing without blowing ($U_\infty = 9$ cm/s, $\alpha = 8^o$).

backward swept case, the tip-jet blowing still helped to make the tip-vortex more disorganized but with less effects than that in the unswept case. Some photographs of the blowing on a forward-swept wing are shown in Figure 3.15.



(a) tip-jet #2 blowing ($C_\mu = 0.027$)



(b) tip-jet #3 and circular-jet #6 blowing ($C_\mu = 0.039$)

Figure 3.15 Flowfield on the tip area of a forward-swept wing with tip-jet blowing ($U_\infty = 9$ cm/s, $\alpha = 8^o$).

CHAPTER IV

WIND TUNNEL EXPERIMENTS AND RESULTS

In order to obtain more knowledge on the wingtip flowfield associated with tip-jets blowing, TiO_2 and kerosene surface streak pattern technique was used on the wing model in the UTSI low-speed wind tunnel. A surface pressure measurement on the wing was also conducted for the purpose of determining the pressure change induced by the wingtip-jet blowing.

§ 4.1 Wind Tunnel, Model, and Experimental Set-up

A. UTSI Low-Speed Wind Tunnel

The University of Tennessee Space Institute (UTSI) low speed wind tunnel is an open circuit continuous wind tunnel with a closed test section. The test section is 35.6 cm in height, 50.8 cm in width and 107 cm in length (H 14 in. × W 20 in. × L 42 in.), and has a Plexiglas side wall for observation and photography. The tunnel is driven by a 1.14 m diameter fan which is powered by a 75 HP motor. The tunnel speed is controlled by a HP Controller such that it can vary continuously from 3 m/sec to 90 m/sec (10 to 300 ft/sec). The tunnel operation and data acquisition are controlled by a IBM personal computer.

B. Model and Experimental Set-up

The model used for these wind tunnel tests was a NACA 0012-64 airfoil with 18.0 cm chord length and 30.48 cm half span. Only the unswept configuration

with wingtip jets (Tip I) were tested in the wind tunnel. The model was made of aluminum in such a way that there was a large access within the airfoil from the root to the wingtip for the purpose of installing the wingtip jets and pressure ports. There were three jet ports on the wing tip and the blowing air was supplied to each tip jet through separate tubes. A sketch of the wing model is given in Figure 4.1. Pressure ports were provided at four span sections with 12 ports for each row on both upper surface and lower surface as shown in Figure 4.1.

The model was supported by a shaft through the tunnel side wall to a mechanical turntable which had the capability to continuously set an angle of attack from 0^o to 360^o. A boundary layer fence was installed between the model and tunnel inner wall to ensure local two dimensional flow. Figure 4.2 shows the wind tunnel experimental set-up.

The blowing air was supplied by a 150 psia low pressure compressor (Pennsylvania). A pressure regulator controlled the air pressure entering to a flowmeter downstream of it. The volume ratio of the blowing air was controlled by a valve which was installed downstream of the flowmeter. The non-dimensional parameter used in the wind tunnel study was also the jet momentum coefficient C_μ, which was defined as

$$C_\mu = \dot{m}V_j/0.5\rho_\infty U_\infty^2 S$$

where V_j is the jet exit velocity, U_∞ is the tunnel velocity and S is the wing area. From the pressure reading at the regulator and the air volume rate at the flowmeter, the C_μ was calculated. Restricted by the jet areas and maximum pressure of the flowmeter, the $C\mu$ values used in this wind tunnel experiment were relatively smaller than those used in the water tunnel study.

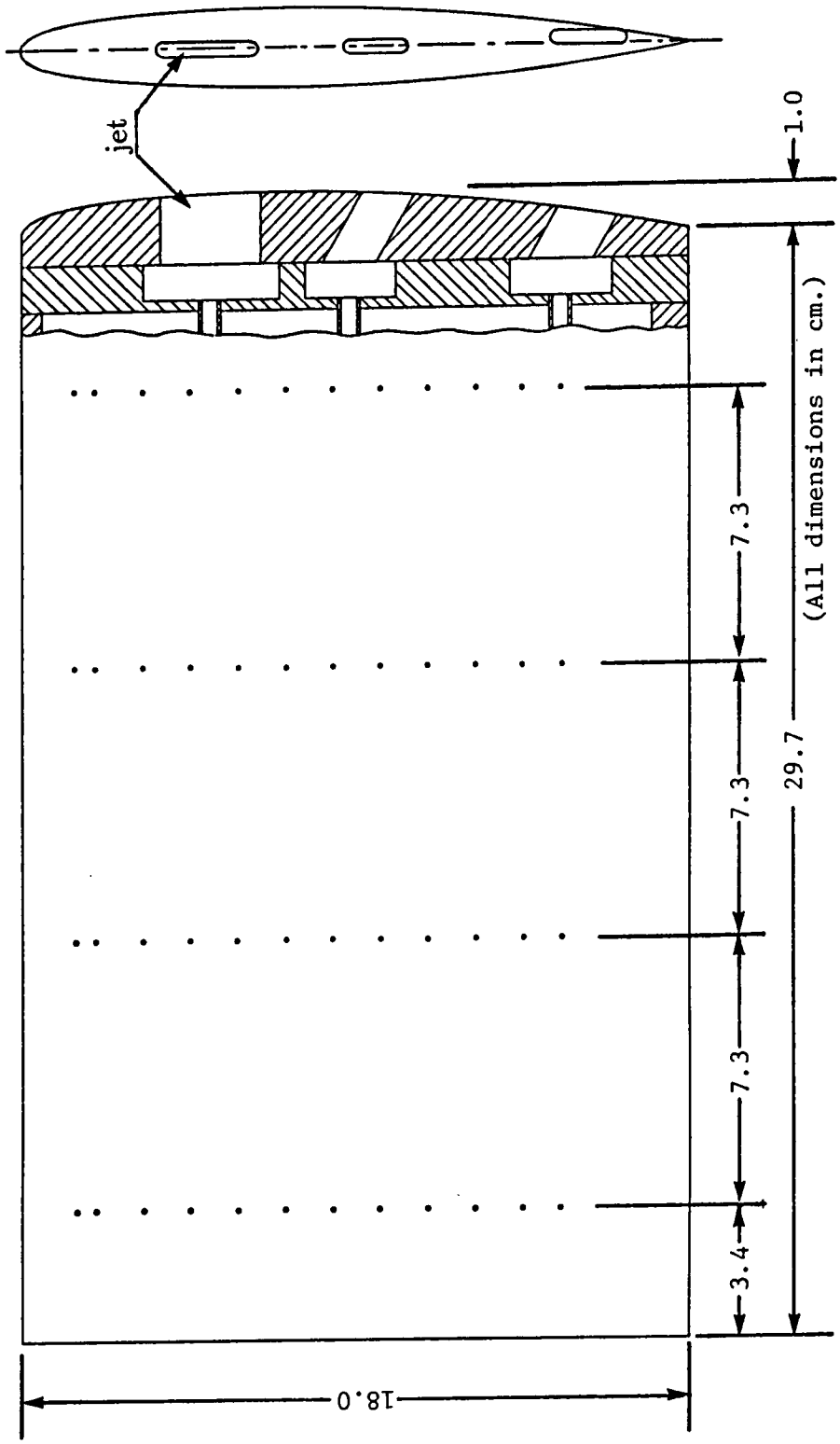
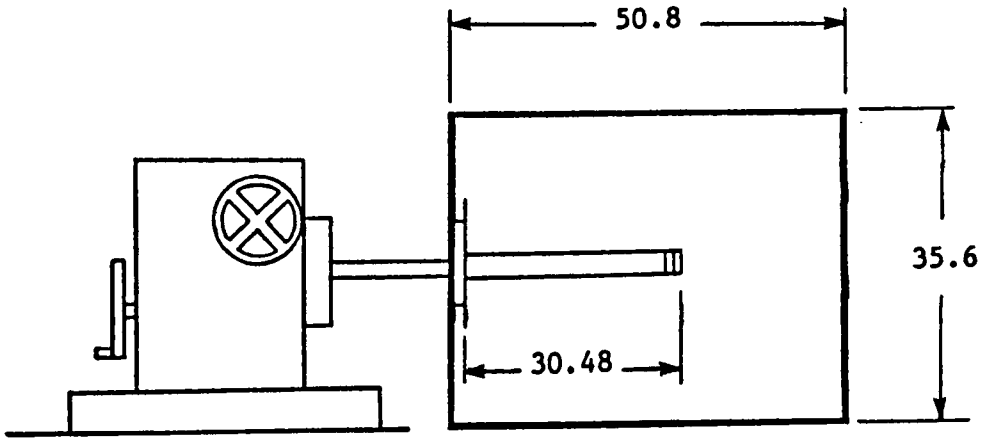
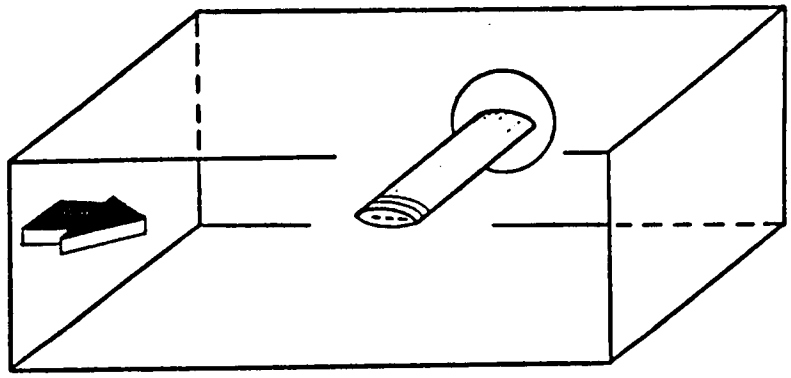


Figure 4.1 Schematic of the wing model for wind tunnel testing.



(all dimensions in cm.)

(a) schematic of sting mounted half-wing model



(b) pictorial view of test section

Figure 4.2 Experimental set-up in the wind tunnel.

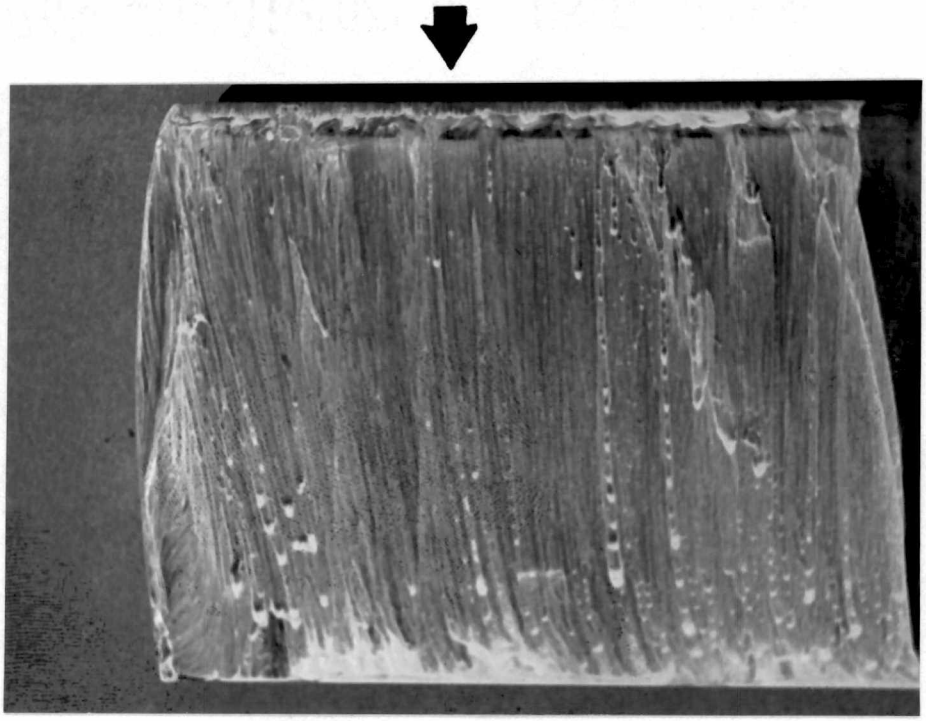
§ 4.2 Surface Streak Patterns

The TiO_2 and kerosene surface streak technique was used to obtain the qualitative surface flow information in order to gain a better physical understanding of the complicated flowfield around the wing with wingtip-jet blowing. Although this method displayed only the footprints of the flowfield on the model surface, together with the water tunnel observation it provided good qualitative information of the flow structure and pattern.

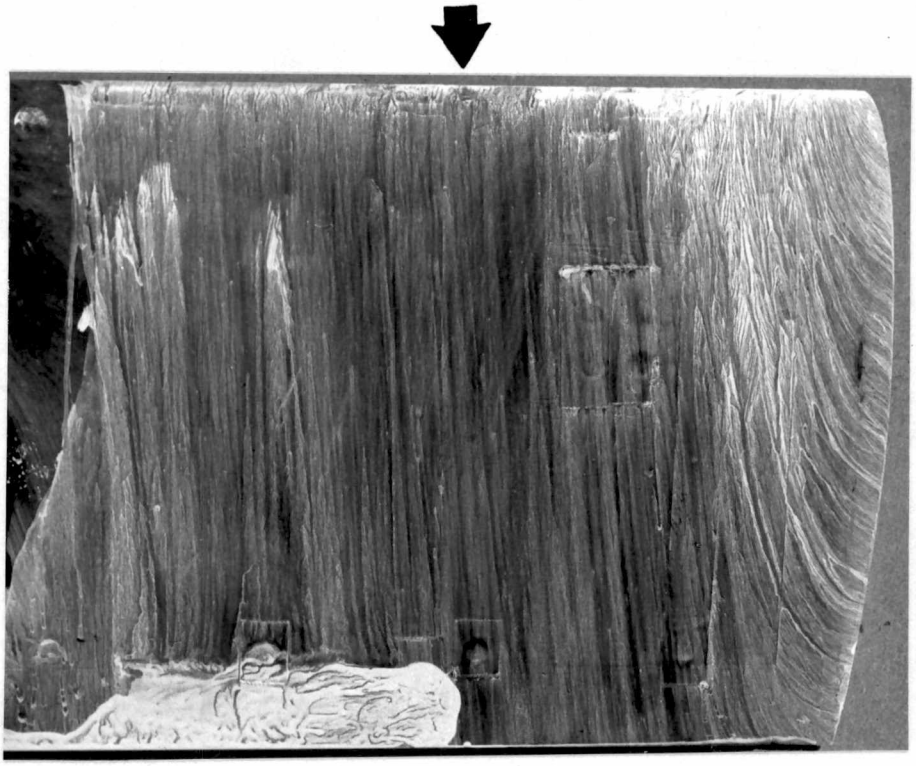
The oil used in this test was a mixture of kerosene and white TiO_2 powder in such a way that it moved with the flow when the tunnel was started and dried on the wing surface after 1 to 2 minutes. Since the tunnel speed reaches its setting value within 20 seconds, the oil trace thus represented the footprints of a steady state flow.

Figure 4.3 is a typical surface streak pattern on the wing model without tip-jet blowing, and some sketches corresponding to these photos is given in Figure 4.4. This is a well known flow pattern and some of its characters are highlighted here. On the upper surface, a narrow separation bubble was observed along the leading-edge. There was also an even narrower separation region along the trailing-edge of the upper surface. Near the root, the flow streak-lines were almost running straight from the leading-edge to the trailing-edge; but close to the wingtip, the fluid from the leading-edge was pushed inboard by the fluid rolled-up from the wingtip so that the surface streak-lines were inclined in a root-wise direction while moving downstream.

On the lower surface near the wingtip, the low pressure on the upper surface caused fluid on the lower side of the wing to move faster and roll-up to form the wingtip vortex, the streak lines on the lower surface near the wingtip region clearly



(a) upper surface



(b) lower surface

Figure 4.3 Surface streak pattern for the wing without tip-jet blowing ($U_\infty = 45$ m/s, $\alpha = 10^o$).



(c) tip

Figure 4.3 (continued).

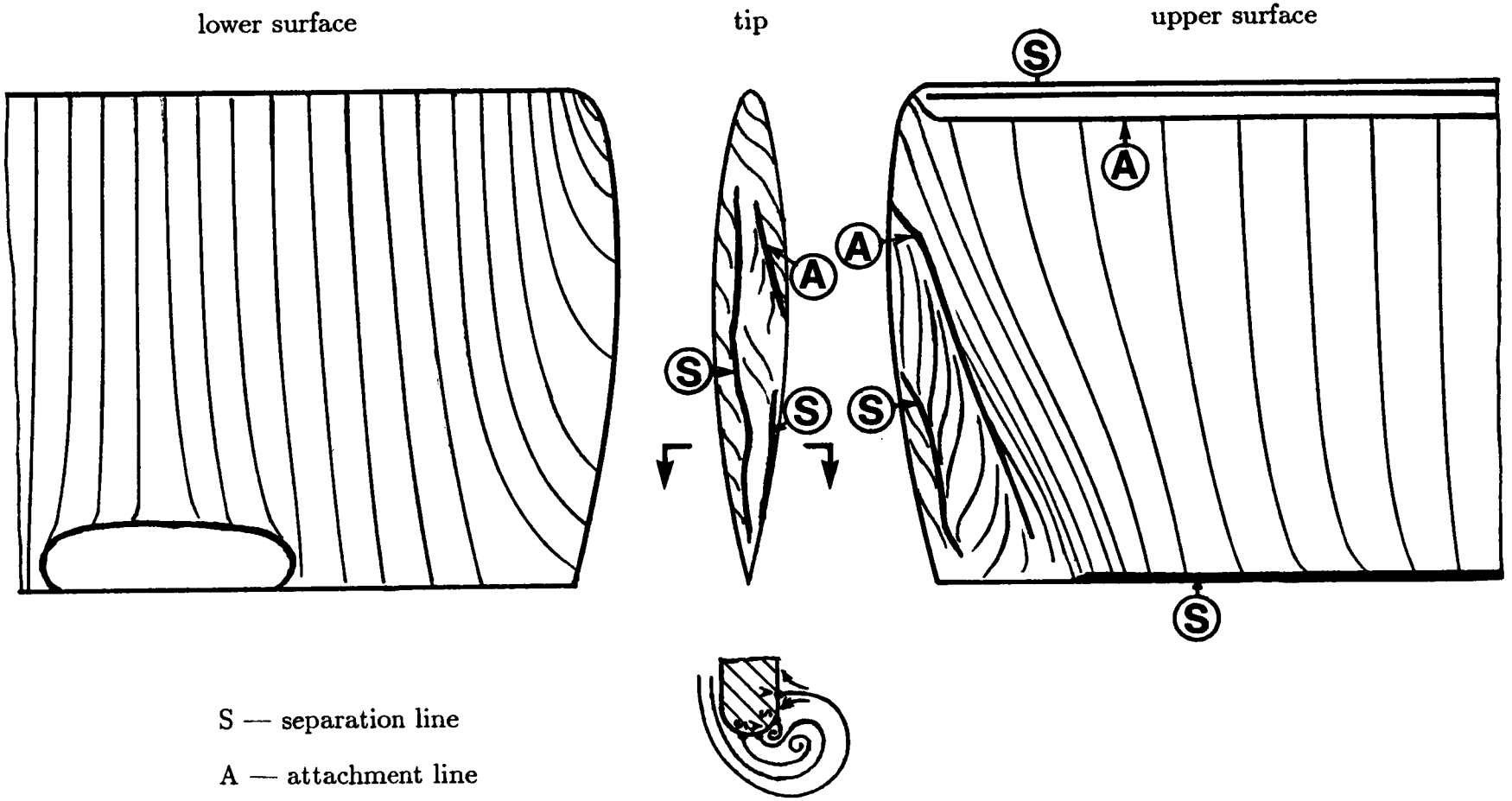


Figure 4.4 Schematic surface streak pattern for the wing without tip-jet blowing.

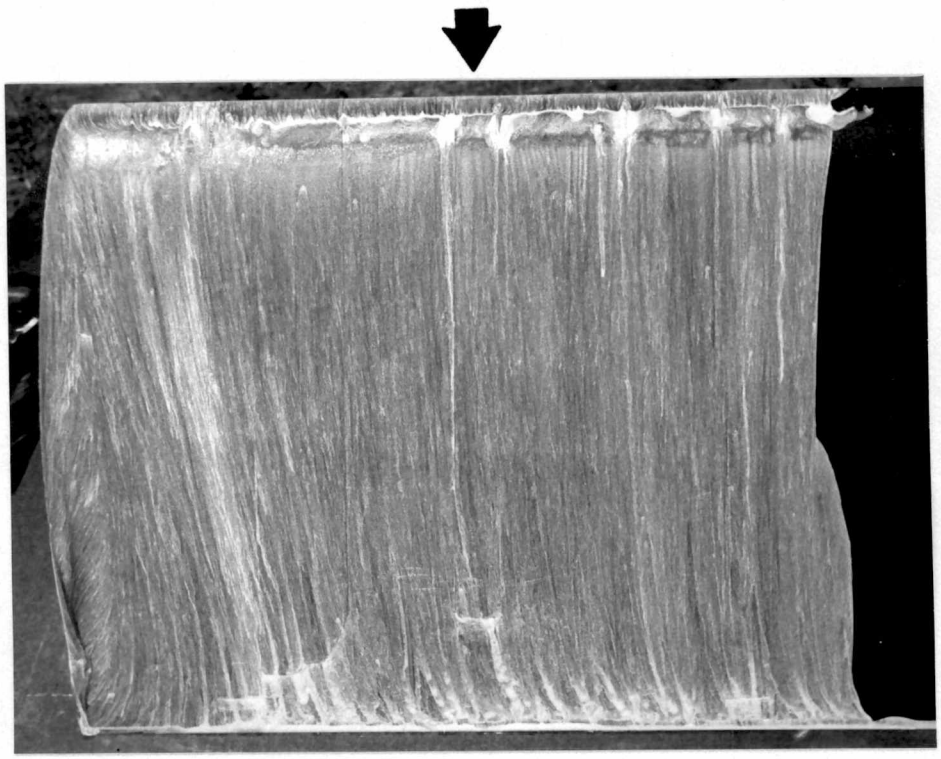
indicated this phenomenon. At the middle portion of the trailing-edge, a region of oil accumulations was observed in this case. It is possible that this was due to a combination of the local surface slope with the wing angle of attack such that it resulted in a local low velocity which could not overcome the oil surface friction; it may even be an indication of a separation bubble. This accumulation did not exist for higher angle of attack cases ($\alpha > 15^o$).

A strong, tight wingtip vortex was formed on the tip. This was evident from the separation and reattaching lines on the tip surface and confirmed by water tunnel observations. In the wingtip region, the surface flow pattern appeared to have a complicated nature. Several separation strips and separation zones were observed. It was believed that when the flow rolled-up from bottom to top, it could not remain attached to the surface all the way up and separated from the surface. In the rectangular wing tip case, the separation area was much larger and almost covered the whole wingtip.

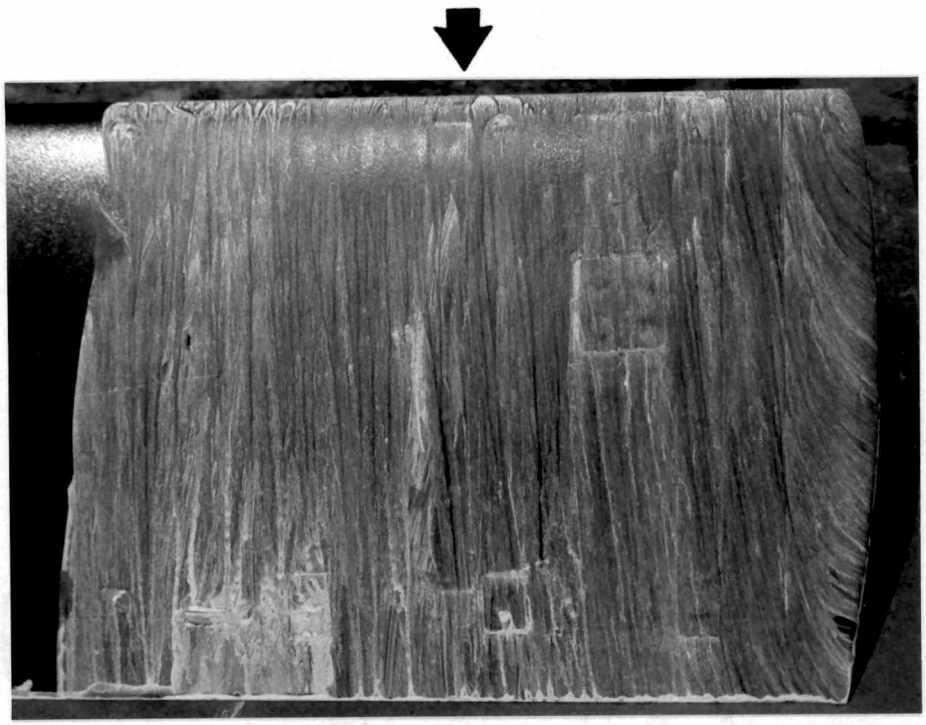
A set of photographs of surface streak patterns for the wing with wingtip jet blowing is shown in Figure 4.5 (the free-stream velocity and angle of attack were kept the same as those used for Figure 3.3) and Figure 4.6 is a sketch of the streak pattern near the jet-orifice. Compared to the surface streak pattern for the no-blowing case, several changes were noticed:

(1). The main changes observed were on the wingtip. The flow pattern near the jet exit was very much like that shown in Figures 3.6 to 3.8 (pp. 81-83), and was consistent with the near surface flow pattern observed in the water tunnel study.

(2). In addition, the reattaching line on the upper wing surface was shifted toward the wingtip. This indicated that the intensity of the wingtip vortex was reduced by the tip-jet blowing.



(a) upper surface



(b) lower surface

Figure 4.5 Surface streak pattern for the wing with tip-jet blowing ($U_\infty = 45$ m/s, $\alpha = 10^o$, tip-jet #2, $C_\mu = 0.002$).



(c) tip

Figure 4.5 (continued).

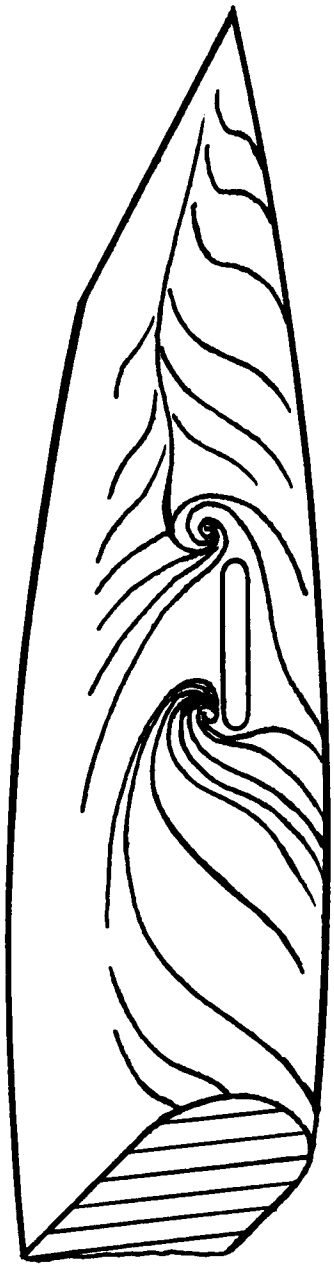


Figure 4.6 A sketch of the surface streak pattern near the jet orifice.

(3). On the tip region of the lower surface, the streak-lines changed their orientation, they became straighter from leading-edge to trailing-edge and less swept toward the wingtip.

(4). The size of the oil accumulation area on the lower surface was reduced by the tip blowing.

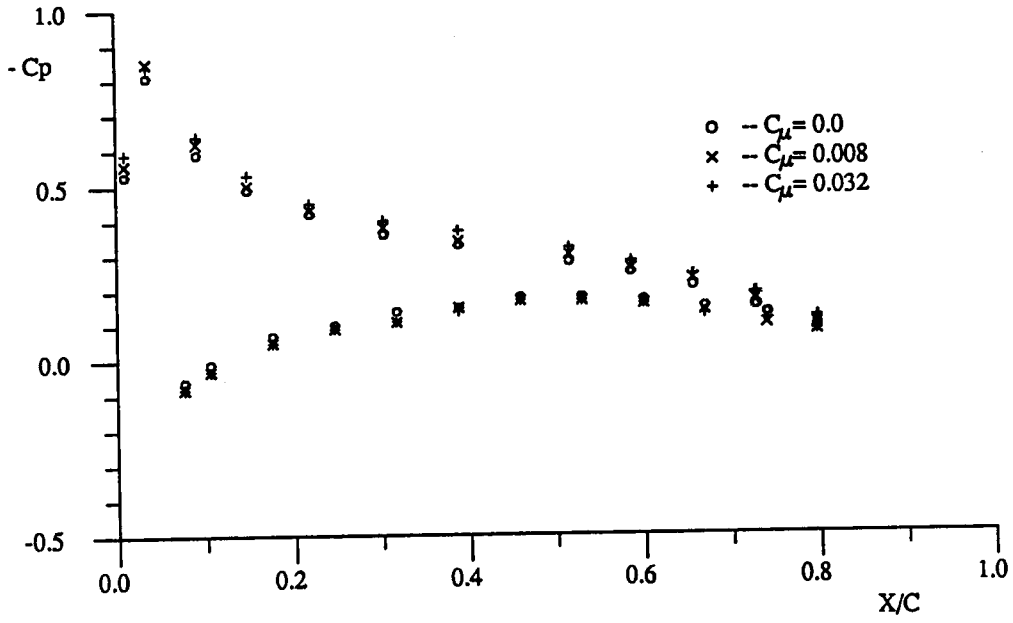
All the changes listed above indicated that the wing-tip vortex intensity was reduced by the tip-jet blowing. The surface flow pattern provided another important information that the tip-jet blowing affected both the flowfield in the wingtip region and that around the whole wing. Hence a global pressure distribution change over the entire wing was caused by the tip-jet blowing as expected.

§ 4.3 Surface Pressure Measurements and Lift Coefficients

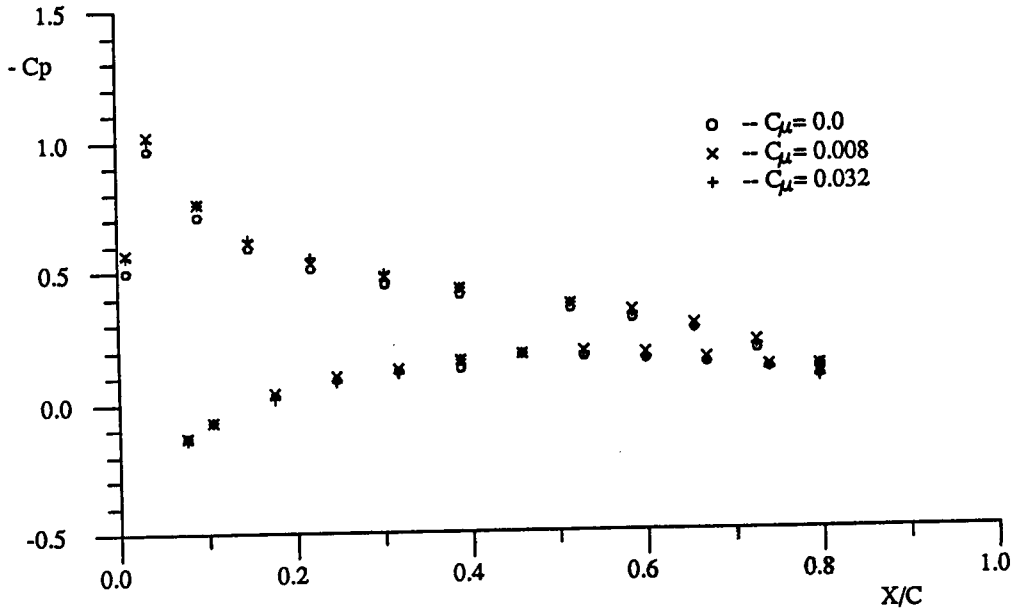
In order to study how the wingtip-jet blowing would affect the pressure distribution on the wing surface, surface pressure measurements were also conducted in the UTSI low speed wind tunnel. The experimental results showed that the wingtip-jet blowing led to a global lift improvement, i.e., the sectional C_l distribution was improved over the entire chord as well as in the spanwise direction.

The surface pressures were measured by four ± 1.3 psid. transducers together with two 24 port wafer switches. The signals were than amplified by a Validyne Amplifier, converted into digital data by a Lab Master A/D converter, and finally collected by an IBM PC/XT personal computer. The data were first checked on the personal computer for quality, then sent to the UTSI VAX 11/785 computer through a communication line for further analysis and plotting.

Some typical comparisons of the pressure distribution on the wing surface with and without jet blowing are shown in Figures 4.7 and 4.8. The results showed

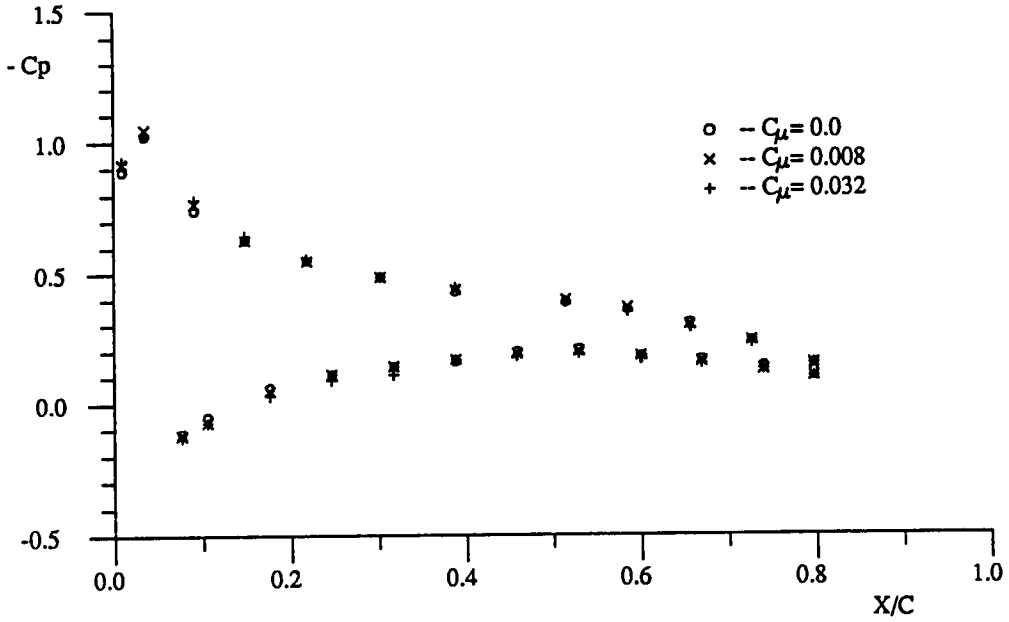


(a) C_p distribution at $2Y/B = 0.826$

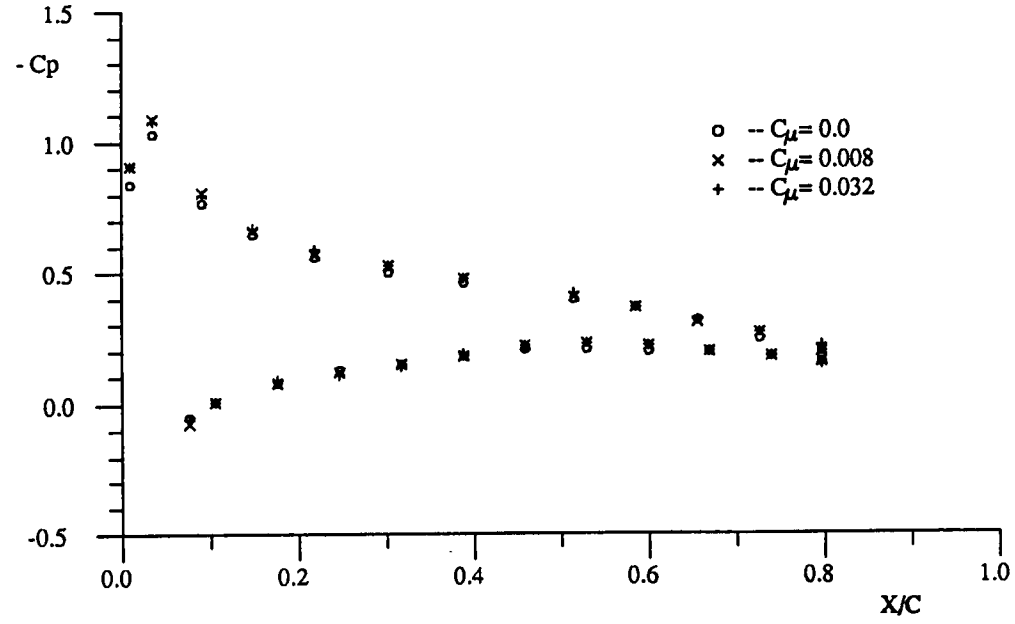


(b) C_p distribution at $2Y/B = 0.588$

Figure 4.7 Chordwise C_p distribution at different sections (jet #1, $U_\infty = 20$ m/s, $\alpha = 5^o$).

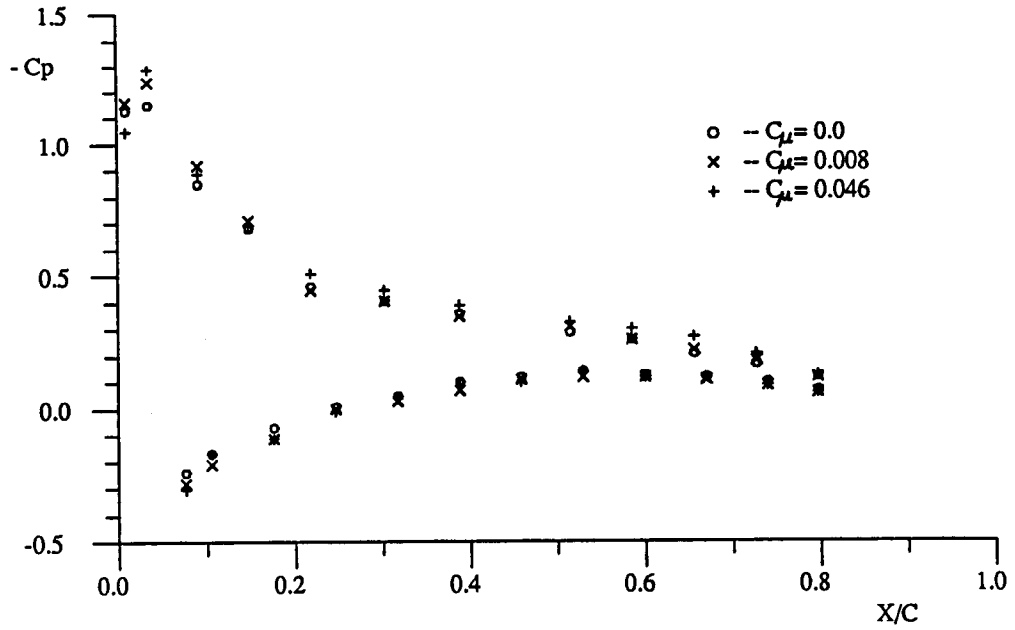


(c) C_p distribution at $2Y/B = 0.35$

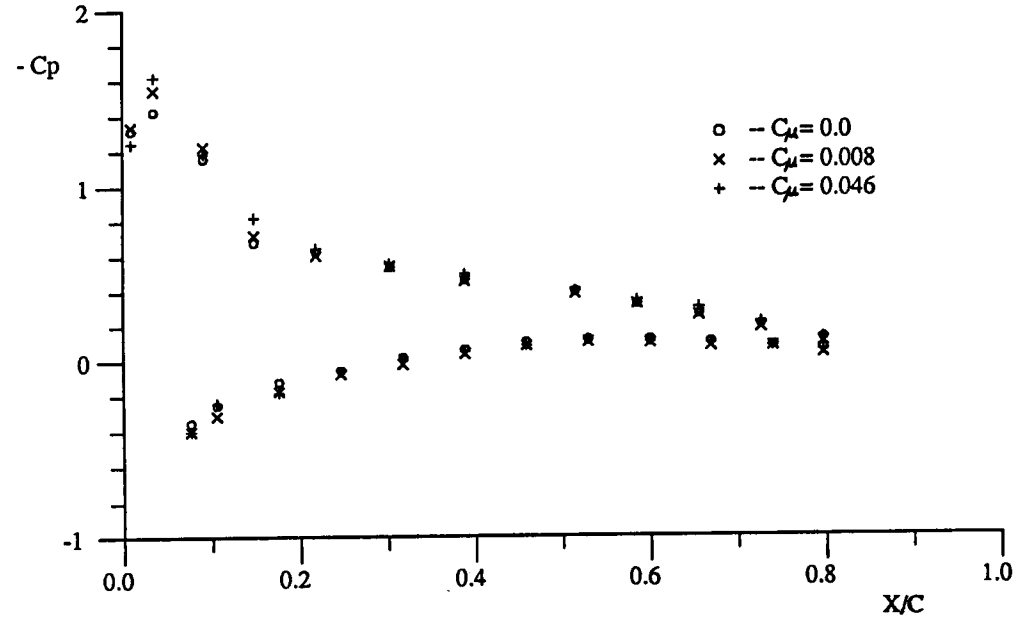


(d) C_p distribution at $2Y/B = 0.1115$

Figure 4.7 (continued)

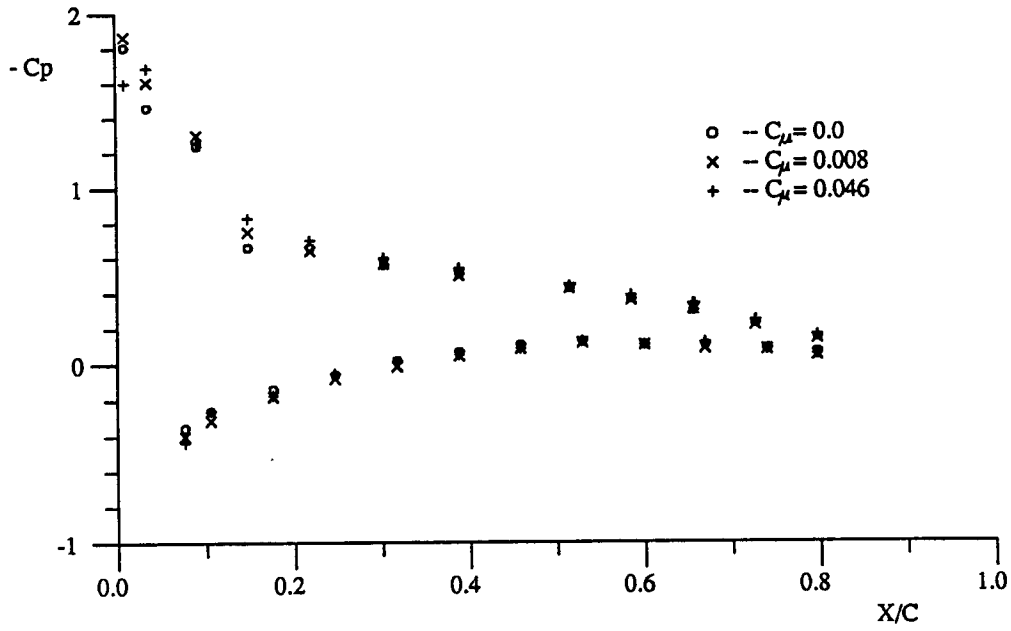


(a) C_p distribution at $2Y/B = 0.826$

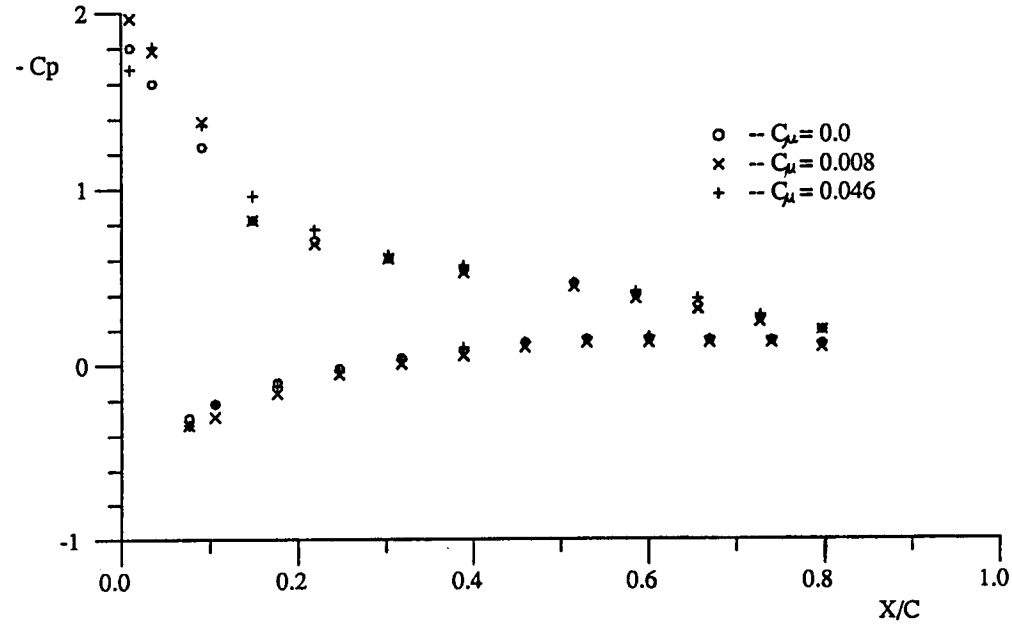


(b) C_p distribution at $2Y/B = 0.588$

Figure 4.8 Chordwise C_p distribution at different sections (jet #2, $U_\infty = 20$ m/s, $\alpha = 8^o$).



(c) C_p distribution at $2Y/B = 0.35$



(d) C_p distribution at $2Y/B = 0.1115$

Figure 4.8 (continued)

that the pressure distribution, C_p, was improved by the wingtip jet blowing. In general, a larger blowing coefficient, C_μ, would result in a better improvement in the pressure distribution. It was noticed that the improvement in the pressure distribution by the jet blowing was different from that created by using a winglet. The winglet utilizes the principle of pressure superposition and its effect is mainly localized. With wingtip jet blowing, the C_p improvement was observed over the entire chord and span, i.e., a more global improvement over the wing was obtained. This implied that the original wing circulation and the vortex system were changed by the jet blowing, which agreed with the qualitatively observed flowfield from the water tunnel experiments and the surface streak pattern.

Spanwise lift distributions were estimated by the chordwise integration of the surface pressure measurements. A line integration was used in the chordwise direction to calculate the sectional C_l values, because there were 12 pressure ports for each row. The curve fitting and numerical integration were used in the spanwise direction because there were only 4 rows of pressure ports along that direction.

Figures 4.9 and 4.10 show two spanwise C_l distributions which correspond to the data in Figures 4.7 and 4.8. The pressure coefficient changed favorably over the whole wing span by the wingtip jet blowing. It was also found that although the pressure distribution improved over the entire wing surface, the increments reduced gradually from the wingtip to the root of the wing (see Figures 4.9 and 4.10).

Typical experimental results of C_l vs. C_μ are given in Figure 4.11. The C_l behaved as a linear function of C_μ for the C_μ range studied. This result was consistent with those observed in Reference [45], which is shown in the same figure. It should be noted, however, that in order to draw a final conclusion that the wingtip-jet blowing can improve the wing performances, more measurements

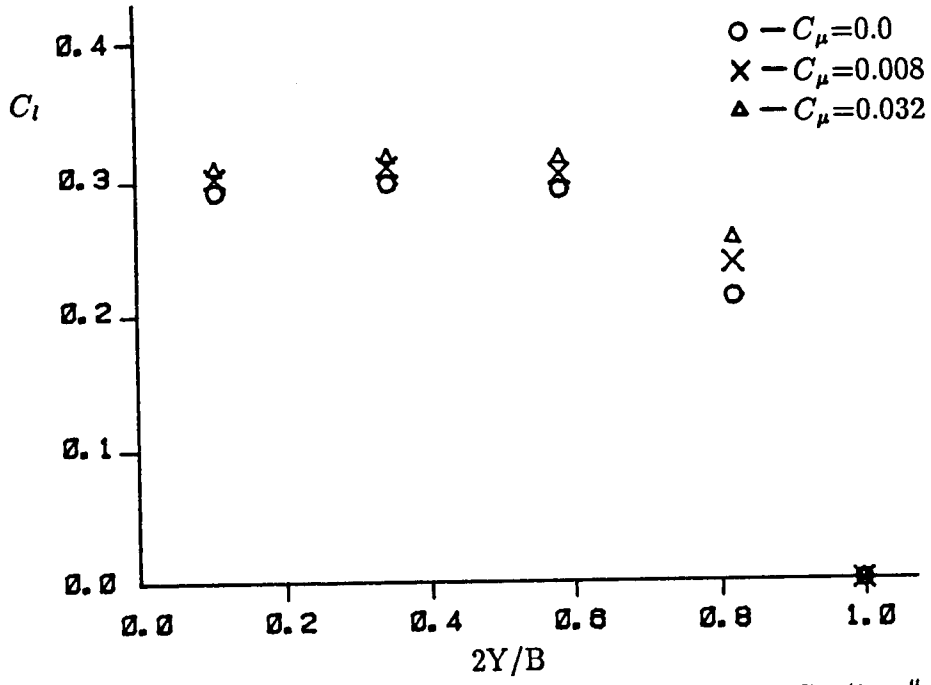


Figure 4.9 Spanwise C_l distribution for different C_μ (jet #1, $U_\infty = 20$ m/s, $\alpha = 5°$).

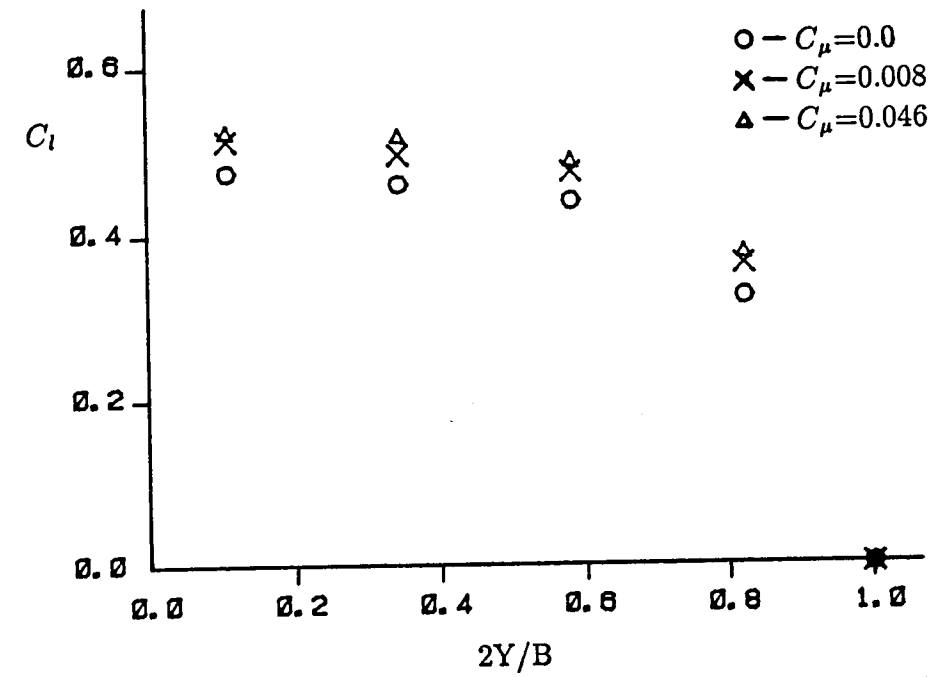
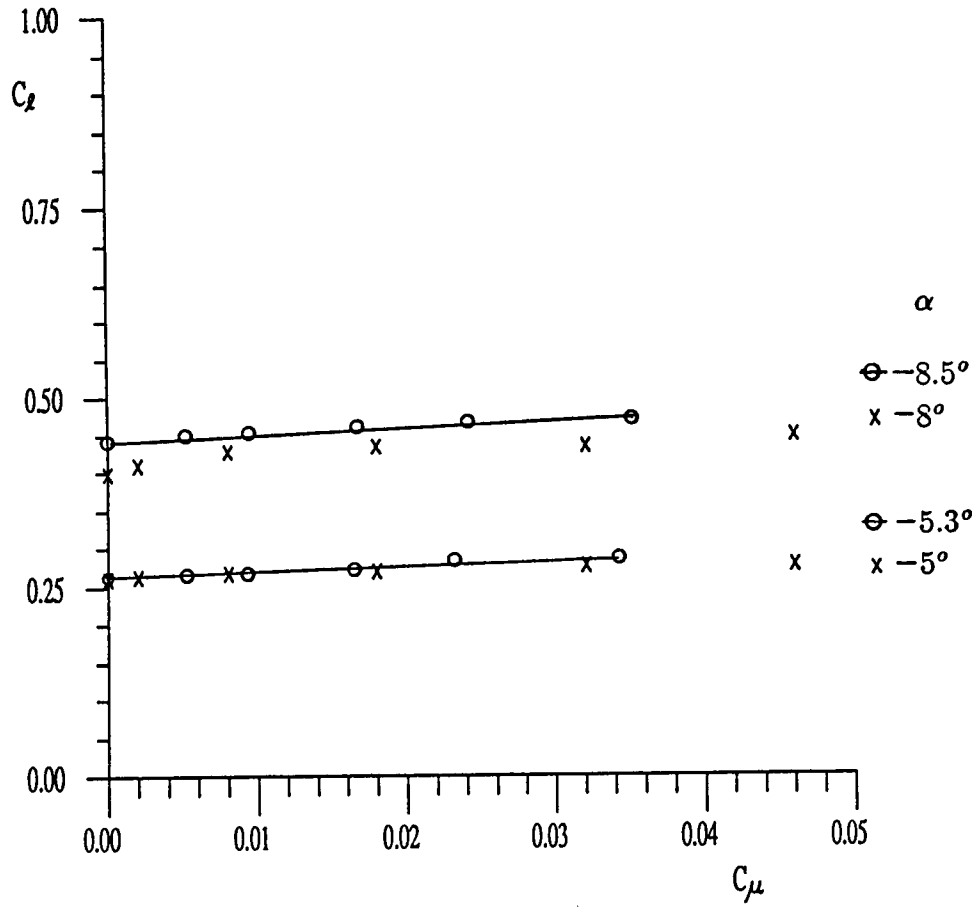


Figure 4.10 Spanwise C_l distribution for different C_μ (jet #2, $U_\infty = 20$ m/s, $\alpha = 8°$).



⊖ – data measured by Mendenhall et al [14]
× – data measured in present study, jet 1

Figure 4.11 Lift coefficients C_l vs. C_μ for different angle of attack.

of C_l at different angles of attack, especially at high angles of attack where the maximum C_l occurs, are needed; drag measurements are also necessary for such a conclusion.

The experimental results showed that blowing from jet-port No. 3 alone was the least effective. This was because the tip-vortex was already partly rolled-up before it reaching the jet-port No. 3 location and thus the effect of the blowing was reduced; this was consistent with the result given in Reference [45].

CHAPTER V

SUMMARY OF THE PRESENT STUDY

This study consists of two parts: a numerical study of jets in crossflow in part I and an experimental study of applications in part II. The findings may be summarized as follows:

Part I

The flowfields of a jet with different shape and orientation in a uniform crossflow were studied numerically. The numerical solutions agreed reasonable well with available experimental results from different sources. The following conclusions were drawn from this part of the study:

- The numerical simulation used in this work predicted the flow features of a jet in crossflow reasonable well. Qualitatively, all the basic flow physics, such as the jet trajectory, the counter-rotating vortex pair, the vertical twin wake vortices, and the horse-shoe vortex, were captured numerically. Reasonable quantitative agreements were also reached for circular jet cases where data are available for comparisons.
- There is a periodic vortex formation at the front bound shear layer of the jet plume which was clearer in the higher jet-to-crossflow velocity ratio cases than that in smaller R cases. The source of these vortices is the front portion of the boundary-layer vorticity generated inside the jet-pipe. The Strouhal number based on the computation is $S_t = 0.25$ for a circular jet with $R = 4$.
- A periodic vortex formation at the rear bound shear layer of the jet plume, which has the same period as the jet's front-bound vortices, was also captured.

The source of these vortices is the rear portion of the boundary-layer vorticity generated inside of the jet-pipe.

- The well known counter-rotating vortex pair is symmetric about the $y = 0$ plane for symmetrically oriented jets and is asymmetric for asymmetric jets. In the asymmetric jet case, the vortex formed on the jet front corner side has higher intensity and larger size than that formed on its rear corner side. The source of these vortices is the boundary-layer vorticity from inside of the jet-pipe. For higher jet-to-crossflow velocity ratio cases, two pairs of counter-rotating vortices were formed and merged together as the jet plume flows downstream.
- The size of the horse-shoe vortex at the front of the jet plume depends on the lateral length of the jet and the jet-to-crossflow velocity ratio. A longer length and a higher velocity ratio resulted a larger horse-shoe vortex. The horse-shoe vortex changed its shape in the same period as that of the jet's front-bound vortices.
- For any shaped jet, a pair of vertical twin tornado-like wake vortices would always form behind the jet plume due to the lower pressure at that region. The source of this vortex pair is the crossflow boundary-layer vorticity and the size of it is depending on the projected length of the jet in the direction normal to the free-stream.
- For an asymmetrically placed jet, the vertical wake vortices are asymmetric in position and different in size; the one corresponding the to jet's front corner is larger and stronger.
- For a long-slot jet with a yaw angle $\beta = 0^o$, a symmetric vortex pair will be formed at its front-corner. When β is increased, the vortex on the wind-side of this corner becomes weaker while that on the lee-side grows stronger. For a

further increased in β, a new vortex is formed on the lee-side of the jet's rear-corner. After β becoming larger than a certain value, the wind-side vortex no longer exists and the vortex at the rear-corner grows stronger. When β reaches 90^o, the vortices on the lee-side of the jet become symmetric.

Part II

An investigation of discrete wingtip jets was also conducted as an application of the asymmetric jet in crossflow. This part of the study consists of many careful flow visualizations in a water tunnel, surface streak patterns and wing surface pressure measurements in a wind tunnel. The following summarizes the results:

- The flow pattern of a wingtip with a tip jet was very similar to the flowfield of an asymmetrically placed rectangular cross-section jet issuing normally from a flat plate to a uniform crossflow. All the vortices observed for the asymmetric jet in uniform crossflow were identified for the wingtip jet flow.
- The roll-up wingtip vortex could be dispersed significantly by the wingtip jets. More jets with higher blowing coefficients resulted in a better dispersion.
- It was found that the pressure distribution on the entire wing can be improved by proper wingtip-jet blowing. The increment was larger near the wingtip and gradually reduced toward the root.
- The individual jet location and blowing momentum are the key control parameters of effectiveness in dispersing the tip vortex.
- The lower surface blowing (at positive angle of attack) was found to be less effective.
- In swept wing configurations, the original tip-vortices were weaker than those in the unswept case, but blowing still had a positive effect.

CHAPTER VI

CONCLUSIONS AND RECOMMENDATIONS

The evidence presented above leads to the conclusion that the flow structure of a jet in crossflow is quite complex; particularly when spanwise symmetry is absent. It is, of course, the latter flow field that is most likely to find application in unfamiliar areas.

One area of application of interest, herein, is to wingtip blowing, where the present study has demonstrated certain benefits of such blowing:

- dispersal of the wingtip vortex,
- beneficial changes in the aerodynamic properties of the wing.

Some recommendations can also be drawn based on the present work. They may be used to improve the numerical simulation for better results in future work:

- It was realized throughout the computation that the lack of a turbulence model limited a better simulation of the problem, especially for the case of higher jet-to-crossflow velocity ratios (i.e., at higher Reynolds number) and at large distances downstream from the jet exit where the turbulent effect becomes more and more significant. Therefore, a turbulence model has to be added into this numerical simulation for any future study.
- Due to the nature of incompressible flow, the convergence was very slow in the present computation. A variable over-relaxation factor should be employed so that the convergence can be improved.
- The computer code used in this work has some difficulty in handling a variable mesh, especially in the y–direction. An improvement is necessary in order to achieve a better resolution and faster convergence.

- It is further recommended that more studies be conducted to determine the optimal tip blowing configuration by careful wind tunnel testing and water tunnel flow observations.
- In order to draw a final conclusion that the tip blowing can improve the wing performance, more lift measurements at different angles of attack, particularly at the high angles of attack where the maximum C_l occurs, is recommended; drag measurements are also necessary for such a conclusion.
- Before any practical application can be considered, it is necessary to study the weight and energy penalty associated with the tip blowing.

BIBLIOGRAPHY

BIBLIOGRAPHY

1. Abramovich, G. N. (1963), The Theory of Turbulent Jets, English Translation published by M.I.T. Press, Massachusetts.

2. Adler, D. and Baron, A. (1978), "Prediction of a Three-Dimensional Circular Turbulent Jet in Crossflow", AIAA Journal, Vol. 17, No. 2, pp. 168-174, February.

3. Andreopoulos, J. (1982), "Measurements in a Jet-Pipe Flow Issuing Perpendicularly Into a Crossflow", Journal of Fluids Engineering, Transactions of the ASME, Vol. 104, pp. 493 - 499 , December.

4. Andreopoulos, J. and Rodi, W. (1984), "Experimental Investigation of Jets in a Crossflow", Journal of Fluid Mechanics, Vol. 138, pp. 93-127.

5. Andreopoulos, J. (1984), "Initial Conditions, Reynolds Number Effects and the Near Field Characteristics of the Round Jets in a Cross Flow", Journal of Flight Sciences and Space Research, Vol. 8, No. 2, pp. 118 - 124.

6. Andreopoulos, J. (1985), "On the Structure of Jets in a Crossflow", Journal of Fluid Mechanics, Vol. 157, pp. 163-197.

7. Anwar, H. O. and Weller, J. A. (1969), "A Thin Rectangular Jet Discharging into a Slow Moving Stream", Water Power, Vol. 21, pp. 214 - 229.

8. Ayers, R. F. and Wilde, M. R. (1956), " An experimental investigation of the aerodynamic characteristics of a low aspect ratio swept wing with blowing in a spanwise direction from the tips," The College of Aeronautics, Cranfield, UK Note 57, September.

9. Briggs, M. M., and Schwind, R. G. (1983), "Augmentation of fighter aircraft lift and STOL capability by blowing outboard from the wing tips," AIAA Paper 83–0078, January.

10. Callaghan, E. E. and Ruggeri, R. S. (1948), "Investigation of the Penetration of an Air Jet Directed Perpendicularly to an Air Stream", N.A.C.A. TN 1615, June.

11. Carafoli, E. and Camarasescu, N. (1971), "New research on small span-chord ratio wings with lateral jets," *Sutdii si Cercetari de Mecanica Aplicata*, Vol 29, No. 4, pp. 947–962, 1970. Available in English as Translation FTD–HC-23–319, Foreign Technology Division, Air Force Station Command, October.

12. Chen, Z. L. and Wu, J. M. (1983), "Jet wing vortex lattice theory with nonlinear wake and tip flow," AIAA Paper 83-0263, January.

13. Chien, J. C. and Schetz J. A. (1975), "Numerical Solution of the Three-Dimensional Navier-Stokes Equations With Applications to Channel Flow and

a Buoyant Jet in a Cross Flow", Journal of Applied Mechanics, Transactions of the ASME, pp. 575 - 579, September.

14. Collins, Frank (1982), "Description of the University of Tennessee Space Institute Water Tunnel", UTSI Report 82-1, University of Tennessee Space Institute, Tullahoma, Tennessee.

15. Crabb, D., Durão, D. F. G. and Whitelaw, J. H. (1981), "A Round Jet Normal to a Crossflow", Journal of Fluid Engineering, Transactions of the ASME, Vol. 103, pp. 142 - 153, March.

16. Demuren, A. O. (1983), "Numerical Calculations of Steady Three-Dimensional Turbulent Jet in Cross Flow", Computer Methods in Applied Mechanics and Engineering, Vol. 37, pp. 309 - 328.

17. Ehrich, F. F. (1953), "Penetration and Deflection of Jets Oblique to a General Stream", Journal of The Aeronautical Science, February, pp. 99-104.

18. Fearn, R. L. and Weston, R. P. (1974), "Vorticity Associated with a Jet in a Cross Flow", AIAA Journal, Vol. 12, No. 12, pp. 1666-1671, December.

19. Fearn, R. L. and Weston, R. P. (1978), "Induced Velocity Field of a Jet in a Crossflow", NASA TP 1087.

20. Fearn, R. L. and Weston, R. P. (1979), "Velocity Field of a Round Jet in a Cross Flow for Various Jet Injection Angles and Velocity Ratios", NASA TP 1506.

21. Fearn, R. L. (1984), "Progress Toward a Model to Describe Jet/Aerodynamic-Surface Interference Effects", AIAA Journal, Vol. 22, No. 6, pp. 752-753, June.

22. Fric, T. F. and Roshko, A. (1989), "Structure in the Near Field of the Transverse Jet", 7^{th} Symposium on Turbulent Shear Flows, August,

23. Foss, J. F. (1980), "Interaction Region Phenomena for the Jet in a Cross-Flow Problem", *Rep.* SFB 80/E/161, February, University of Karlsruhe.

24. Gilliam, F. T. (1983), "An Investigation of the effects of discrete wing tip jets on wake vortex roll up," Ph.D. dissertation, The University of Tennessee Space Institute, August.

25. Gordier, R. L. (1959), "Studies of Fluid Jets Discharging Into Moving Liquid", St. Anthony Falls Hydro Labortory, University of Minnesota, Tech. Paper No. 28, Series B.

26. Hirt, C. W., Nichols, B. D., and Romero, N. C. (1975), "SOLA— A Numerical Solution Algorithms for Transient Fluid Flows" Los Alamos Scientific Labratory Report, LA-5852, AD-A009 953, April.

27. Hirt, C. W. (1979), "Simplified Solution Algorithms for Fluid Problem" Numerical Methods for Partial Differential Equations, Edited by S. V. Parter, Academic Press, Inc., New York.

28. Jordinson, R. (1958), "Flow in a Jet Directed Normal to the Wind" R. & M. No. 3074, A.R.C. Technical Report, October.

29. Karagozian, A. R. (1986), "An Analytical Model for the Vorticity Associated with a Transverse Jet", AIAA Journal, Vol. 24, No. 3, pp. 429-436, March.

30. Keffer, J. F. and Baines, W. D. (1963), "The Round Turbulent Jet in a Cross Wind", Journal of Fluid Mechanics, Vol. 15, Part 4, pp. 481–496.

31. Krausche, Dolores and Fearn, Richard L. (1978), "Round Jet in a Flow: Influence of Injection Angle on Vortex Properties", AIAA Journal, Vol. 16, No. 6, pp. 636-637, June.

32. Krause, E. (1985), "Review of Some Vortex Relations", Computers & Fluids, Vol. 13, No. 4, pp. 513-515.

33. Krothapalli, A. and Lourenco, L. (1989), "On the Separated Flow Upstream of a Jet in a Cross Flow", AIAA Paper 89-0571, January, 1989.

34. Lee, C. S., Tavella, D. A., Wood, N. J., and Roberts, L. (1986), "Flow structure of lateral wing tip blowing," AIAA Paper 86–1810, June.

35. Lee, C. S., Tavella, D. A. and Wood, N. J. (1987), "Flow structure and scaling in lateral wing-tip blowing," Stanford University, August.

36. LeGrivés, E. (1978), "Mixing Process Induced by the Vorticity Associated with the Penetration of a Jet into a Cross Flow", Journal of Engineering for Power, Vol. 100, No. 3, pp. 465-475, July.

37. Lighthill, M. J. (1963), "Introduction to Boundary Layer Theory in Laminar Boundary Layers" (Ed. Rosenhead), Oxford Univ. Press, pp. 46-113.

38. Lloyd, A. (1963), "The effects of spanwise blowing on the aerodynamic characteristics of a low aspect ratio wing," Von Karman Institute Project Report 1963-90. Rhode-st. Geneses, Belgium.

39. Malvern, L. E. (1969), Introduction to the Mechanics of a Continuous Medium, Prentice-Hall, Inc., New Jersey.

40. Margason, R. J. (1968), "The path of a jet directed at large angle to a subsonic free stream," NASA TND-4919.

41. Markstein, G. H. (1964), "Experimental Studies of Flame-Front Instability", Nonsteady Flame Propagation, AGARDograph No. 75, Pergamon Press, Oxford, pp. 75-100.

42. McAllister, J. D. (1968), "A Momentum Theory for the Effects of Cross Flow on Incompressible Turbulent Jets", Ph.D. dissertation, University of Tennessee.

43. McMahon, H. M., Mosher D. K. (1970), "Experimental Investigation Pressure Induced on a Flat Plate by a Jet Issuing into Subsonic Crosswind", NASA SP 218, N70-11830, pp. 49-62.

44. McMahon, H. M., Hester, D. D. and Palfery, J. G. (1971), "Vortex Shedding From a Turbulent Jet in a Cross-Wind", Journal of Fluid Mechanics, Vol. 48, Part 1, pp. 73-80.

45. Mendenhall, M. R., Caruso, S. C., Lesieutre, D. J. and Childs, R. E. (1987), " An investigation of wing lift augmentation with spanwise tip blowing," AFWAL-86-3112, Nielsen Engineering & Research, Inc. April.

46. Patankar, S. V., Basu, D. K. and Alpay S. A. (1981), "Prediction of the Three-Dimensional Velocity Field of a Deflected Turbulent Jet", Journal of Fluid Engineering, Transactions of the ASME, pp. 758–762, December.

47. Pratte, B. D. and Keffer, J. F. (1969), "Swirling Turbulent Jet Flows - Part 1: The Single Swirling Jet", UTME-TP-6910, University of Toronto, Toronto Canada.

48. Rajaratnam, N. (1976), Editor, Turbulent Jet, New York Elsevier Scientific Pub. Co., New York, pp. 184-210.

49. Ramsey, J. W. and Goldstein, R. J. (1972), "Interaction of a Heated Jet with a Deflecting Stream", NASA CR-72613

50. Reilly, R. S. (1968), "Investigation of the Deformation and Penetration of a Turbulent Subsonic Jet Issuing Transversely into a Uniform, Subsonic Main Stream", Ph.D. dissertation, University of Maryland.

51. Roth, K. R. (1987), "Numerical Simulation of a Subsonic Jet in a Crossflow", SAE Paper 872343, 1987.

52. Ruggeri, R. S., Callaghan, E. E. and Bowden D. T. (1950), "Penetration of Air Jets Issuing from Circular, Square, and Elliptical Orifices Directed Perpendicularly to a Air Stream", N.A.C.A. TN 2019, February.

53. Simon, F. F. and Ciancone, J. L. (1986), "Flow Visualization Study of the Effect of Injection Hole Geometry on an Inclined Jet in Cross Flow", Heat Transfer and Fluid Flow in Rotating Machinery, edited by Wen-Jei Yang, Hemisphere Publishing Corporstion, New York, pp. 170-192.

54. Sykes, R. I., Lewellen, W. S. and Parker, S. F. (1986) "On the Vorticity Dynamics of a Turbulent Jet in a Crossflow", Journal of Fluid Mechanics, Vol. 168, pp. 393-413.

55. Tavella, D. A., Wood, N. J., and Harrits, P. (1985), "Influence of the tip blowing on rectangular wings," AIAA Paper 85–5001, October.

56. Tavella, D. A. and Roberts, L. (1985), "The concept of lateral blowing," AIAA Paper 85–5001, October.

57. Tavella, D. A., Lee, C. S., and Wood, N. J. (1986), "Influence of wing tip configuration on lateral blowing efficiency," AIAA Paper 86–0475, January.

58. Thompson, Jr., J. F. (1971), "Two Approaches to the Three-Dimensional Jet-in-Cross-Wind Problem: a Vortex Lattice Model and a Numerical Solution of the Navier-Stokes Equations", Ph.D. dissertation, Georgia Institute of Technology.

59. Thompson, P. A. (1972). Compressible-Fluid Dynamics, McGraw-Hill Book Company, New York.

60. Weston, R. P. and Thames, F. C. (1979), "Properties of Aspect-Ratio-4.0 Rectangular jets in a Subsonic Crossflow", AIAA Journal, Vol. 16, No. 10, pp. 701-707, October.

61. White, H. E. (1963), "Wind tunnel investigation of the use of wing-tip blowing to reduce drag for take-off and landing," The David Taylor Model Basin Aerodynamics Laboratory, AERO Report 1040, January.

62. Wilson, T. L., Nichols, B. D., Hirt, C. W., and Stein, L. R. (1988), "SOLA—DM A Numerical Solution Algorithms for Transient Three-Dimensional Flows" Los Alamos Scientific Labratory Report, LA-11161-MS, February.

63. Wu, J. C. and Mosher, D. K. (1969), "Experimental and Analytical Investigation of Jets Exhausting Into a Deflecting Stream", AIAA Paper No. 69-225, AIAA/AHS VTOL Research, Design and Operation Meeting, Atlanta, Georgia, February 17-19.

64. Wu, J. M., Vakili, A. D. and Chen, Z. L. (1982),"Wing-Tip Jets Aerodynamic Performance", Proceedings of the 13th International Council for Aeronautical Sciences", edited by B. Laschka and R. Staufenbiel, Seattle Washington, August.

65. Wu, J. M., Vakili, A. D., Chen, Z. L. and Gilliam, F. T. (1983), "Investigation on the effects of discrete wingtip jets," AIAA Paper 83–0546, January.

66. Wu, J. M. and Vakili, A. D. (1984), "Aerodynamic Improvements by Discrete Wingtip Jets", Flight Dynamics Laboratory, Air Force Wright Aeronautical Laboratories, WPAFWAL TR 84-3009.

67. Wu, J. M., Vakili, A. D., Gilliam, F. T. (1984), "Aerodynamic interaction of wing tip flow with discrete wing tip jets," AIAA Paper 84–2206, August.

68. Wu, J. M., Vakili, A. D. and Yu, F. M. (1986), "Investigation of the Interacting Flow of Non-Symmetric Jets in Cross Flow", AIAA paper 86-0280, AIAA 24th Aerospace Sciences Meeting, Reno, Nevada, January 6-9.

69. Wu, J. Z., Wu, J. M. and Wu, C. J. (1987), "A General Three-dimensional Viscous Compressible Theory on the Interaction Solid Body and Vorticity-Dilatation Field", UTSI Report 87/03, March.

70. Wu, J. Z., Wu, J. M. and Wu, C. J. (1988), "A Viscous Compressible Flow Theory on the Interaction Between Moving Bodies and Flow Field in the (ω , θ) Framework", Fluid Dynamics Research, Vol. 3, Nos 1-4, pp. 202-208.

71. Yu, F. M. (1987), "An investigation of Non-symmetric Jets in Cross Flow," Ph.D. dissertation, The University of Tennessee Space Institute, June.

72. Yu, F. M., Wu, J. M. and Vakili, A. D. (1988), "Investigation of vortical flow properties of jet in cross flow," AIAA Paper 88-0698, January.

VITA

Zhi Shi was born on December 12, 1948, in Nanjing, China. He attended elementary and high schools in Shanghai. In February of 1979, he entered The Jiao-Tong University, Shanghai and graduated in January of 1983 with a Bachelor of Science degree in Mechanical Engineering.

In 1983, he entered the University of Tennessee Space Institute as a graduate student and has continuously served as a Graduate Research Assistant since. He was granted the Master of Science degree in aerospace engineering in March, 1986. In May 1990, he completed his studies with the degree of Doctor of Philosophy with a major in Aerospace Engineering.

Owing to his academic excellence and fine research performance, he has continuously been awarded the B. H. Goethert Scholarship from 1986 to 1990. He is a member of AIAA and SIAM.

Zhi is happily married to the former Shan-Fang Zhang. They have a daughter, Yun-Ying. His family is living with him now in Tullahoma, Tennessee.